Stimulated Raman Scattering in High-Power Fiber Lasers

DISSERTATION
zur Erlangung des akademischen Grades
doctor rerum naturalium (Dr. rer. nat.)

FRIEDRICH-SCHILLER-
UNIVERSITÄT
JENA

vorgelegt dem Rat der Physikalisch-Astronomischen Fakultät
der Friedrich-Schiller-Universität Jena

von M.Sc. Victor Distler (geb. Bock)

geboren am 15.07.1993 in Amberg

Gutachter:

1. Prof. Dr. Jens Limpert, Friedrich-Schiller-Universität Jena

2. Prof. Dr. Liang Dong, Clemson University

3. Prof. Dr. Markus Schmidt, Friedrich-Schiller-Universität Jena

Tag der Disputation: 25.11.2021

Contents

This thesis is based upon work performed at the Friedrich-Schiller University Jena and at the Fraunhofer Institute for Applied Optics and Precision Engineering - some passages rely on information published previously in the sources listed under *Publications*.

1 Introduction

During the last decades, high-power fiber lasers moved from research laboratories into an unforseen diversity of production processes and paved the way into the so-called "photonic century". Pairing high brightness with excellent beam quality, fiber lasers enable precise, quick and energy-efficient processing. Furthermore, fiber lasers are cheap in construction and maintenance, have a small footprint and are environmentally stable. Consequently, they have been widely adopted in industrial applications, which has led to a global market size of more than 2 billion USD per year (technavio.com, 2020). Besides this sizeable market, many scientific applications, such as laser guide star or remote sensing, also require fiber laser systems. The beam size emitted by a typical high-power, cw fiber laser is in the order of $\mathcal{O}(300\,\mu m^2)$ at the fiber output. This combined with the average output powers of several kW, which these systems can emit with a diffraction limited beam quality (Beier et al., 2017a), results in very high intensities of more than $\mathcal{O}(10\,\frac{GW}{m^2})$. This is a million times brighter than the sun, as seen form earth on a perpendicular surface. However, an even higher output power would be beneficial for many scientific, industrial and security applications (Dong et al., 2017). Unfortunately, a further output power scaling is limited by Stimulated Raman scattering (SRS), an effect that transfers significant signal power to longer wavelengths (Zervas, 2019). This effect is based on Raman scattering, a light-matter interaction that typically annihilates an incident photon to create a photon of longer wavelengths and a phonon (e.g. a molecular vibration). As this reduces the signal strength at the original wavelength and the photon dissipates into heat, SRS is to be avoided in those systems.

To this end, different approaches have been tested. Among them are spectrally selective fibers, that exhibit high propagation losses at the Stokes wavelength (Fini et al., 2006; Kim et al., 2006), but these complex fiber designs require substantial effort in production. Another possibility is to introduce

spectrally selective filters into common fibers (Nodop et al., 2010), which is briefly examined within this thesis. Additionally, before the beginning of this study it was experimentally discovered that the spectral width of the output coupler of a high-power fiber oscillator influences the Raman content by several orders of magnitude (Schreiber et al., 2014). This was followed by intense research, as discussed later. However, the discovery could not be theoretically explained at the time, which is changed by this thesis, that presents a simple analytic model for the observed behavior.

Besides the limits of further output power scaling, another important obstacle of high-power fiber lasers is the limited working wavelength range of these systems. Inherently, fiber lasers can only emit radiation at wavelengths within the relatively small bounds given by the transitions of their active, rare-earth ions, which leaves considerable spectral gaps. Unfortunately, the aforementioned scientific applications oftentimes require high average powers at wavelengths within these gaps. Here, SRS is one possible solution to address these spectral gaps in the form of a Raman fiber amplifier (RFA) (Supradeepa et al., 2017).

Different concepts of RFA have been presented to meet this demand: For example, cladding pumped systems, that show brightness enhancement, but a beam quality of $M^2 > 2.5$ have recently reached output powers of several kW (Glick et al., 2018; Chen et al., 2020a). Cladding pumped systems do not show $M^2 \leq 1.9$ for output powers over 270 W (Chen et al., 2020b). For core pumped systems, which yield better beam quality factors, the output powers of narrow-linewidth systems are in the range of 100 W (Wei et al., 10.07.2018), while spectrally broader Yb-doped (hybrid) RFA show output powers in the kW range (Ma et al., 2020). In recent years it has been discovered that SRS can reduce the beam quality of Yb-doped, high-power fiber lasers (Hejaz et al., 2017; Liu et al., 2018). Very recently it was shown that even RFA are limited by the onset of transverse mode instability (TMI), a nonlinear effect that causes a temporal beam profile fluctuation and results in a beam quality degradation (Zhang et al., 2020). However, the interplay between SRS and TMI required further investigations as it remained unclear whether TMI are also limiting RFA based on passive fiber and what the key influence parameters are. This thesis gives an answer to these questions by an experimental realization and examination of a passive fiber based, narrow-linewidth RFA delivering up to 500 W Stokes

power.

This thesis is structured as follows. The fundamentals necessary to understand the presented investigations are given in chapter 2. This chapter describes the working principle of rare-earth doped fiber amplifiers and high-power fiber lasers. The physics of the main nonlinear effects (including SRS) and their mathematical description is presented. Furthermore, thermal effects (including TMI) occurring in high-power fiber laser systems are explained. A brief discussion of the state of the art of RFAs concludes the chapter.

The following chapter 3 investigates SRS in broad-band cw sources in more detail. Here an analytical model of SRS is developed, that explains the different Raman content observed in high-power fiber oscillators depending on their spectral width. The spectral width of the Stokes signal in a narrow-band cw RFA is investigated in chapter 4. The role of XPM as a limitation of such a system is clarified. Thereafter, chapter 5 is focused on the thermal effects in such an RFA, mainly TMI. Here, the research on the interaction of SRS on TMI in active fibers is reviewed. A new method to detect TMI in a spectrally resolved manner is presented. The narrow-band, high-power RFA from chapter 4 is improved, enhanced and thoroughly investigated. This leads to the first experimental observation of SRS-induced TMI in a passive fiber. This observation is followed by an analysis of the most influential parameters of SRS-induced TMI. Finally, a conclusion is drawn in chapter 6.

2 Fundamentals

This chapter provides the fundamentals necessary for the understanding of this thesis. The working principle of fiber lasers is summarized in section 2.1. Therein, the guiding principle of light in optical fibers is explained and the concept of different transverse modes is introduced. This is followed by a discussion of the special characteristics of high-power fiber lasers. As nonlinear effects play a major role in these systems, the nonlinear propagation of light is detailed in section 2.2. This section also explains SRS in detail, alongside a brief discussion of several other nonlinear optical effects. Besides nonlinear optical effects, thermal effects are also very important in high-power fiber laser systems. These effects, and especially TMI, are explained in section 2.3. Finally, section 2.4 presents the working principle of Raman fiber amplifiers (RFA) and summarizes their properties and applications.

2.1 Rare-earth doped fiber lasers

An optical fiber is a thin glass cylinder that guides light. Section 2.1.1 explains how this can be achieved. The basic idea of a fiber laser is to put the active material, necessary for every laser process, inside an optical fiber. This has several advantages: Optical fibers are usually flexible, which allows for easy handling. On top of that, optical fibers have a high surface to volume ratio, which allows for efficient cooling and an excellent, almost power-independent beam quality. The incorporation of the active material (rare-earth dopants) into the glass forming the fiber is achieved during fiber production, usually by either modified chemical vapor deposition or a powder-sinter-technique (Langner et al., 2011). To increase the solubility of the active ions in the glass matrix, several co-dopants are introduced into the fiber as well (Kuhn et al., 2018). Since there are many degrees of freedom in this process, optimizing the correct fiber ma-

terial system can be challenging (Möller et al., 2020b), but these investigations are beyond the scope of this thesis. Here, it is assumed that by choosing a correct material system, any desired active material concentration can be achieved. For the laser process, the active material alone is not sufficient but population inversion, meaning there are more excited than de-excited active ions, has to be achieved as well. Therefore, not only the signal light, but also a pump signal has to be guided by the fiber. This is achieved by a specific design that is detailed in the following.

2.1.1 Light guidance in optical fibers

General operating principle

Optical fibers considered in this thesis consist of a cylindrical fiber core that is surrounded by a cladding that, in turn, is surrounded by a coating. While the fiber core and cladding are made from (doped) fused silica, the coating is made from a polymer. This polymer coating provides protection against mechanical stress, index-matching oils and or other parasitic environmental influences. Between the fiber core and cladding there is a refractive index step, with the core having a higher refractive index. Signal light travelling along the core undergoes total internal refraction at its outer boundary to cladding, following Snell's law. The separation of the glass cylinder into a core and cladding enables the creation of high-brightness signal light. Thereto, low-brightness pump light is coupled into the fiber cladding. A refractive index step between the cladding and surrounding polymer coating ensures guidance of this pump light along the cladding. This pump light is then absorbed by active ions in the core region of the fiber, resulting in a population inversion. The population inversion is then exploited by light travelling along the fiber core, resulting in an amplification of the latter. Thus, high-brightness signal light is created in the fiber core. Introducing the active material only into the core region of the fiber ensures that there is no signal light created in the cladding, which would degrade the targeted brightness. In such a fiber design, the propagation direction of the pump light and signal light can either be aligned (co-pumping) or opposed (counter-pumping).

A photograph of a fiber taken from the side is shown in Figure 2.1. Commonly, the name of the fiber incorporates the core and cladding diameter: a 20/400 µm fiber has a core diameter of 20 µm and a cladding diameter of

400 µm.

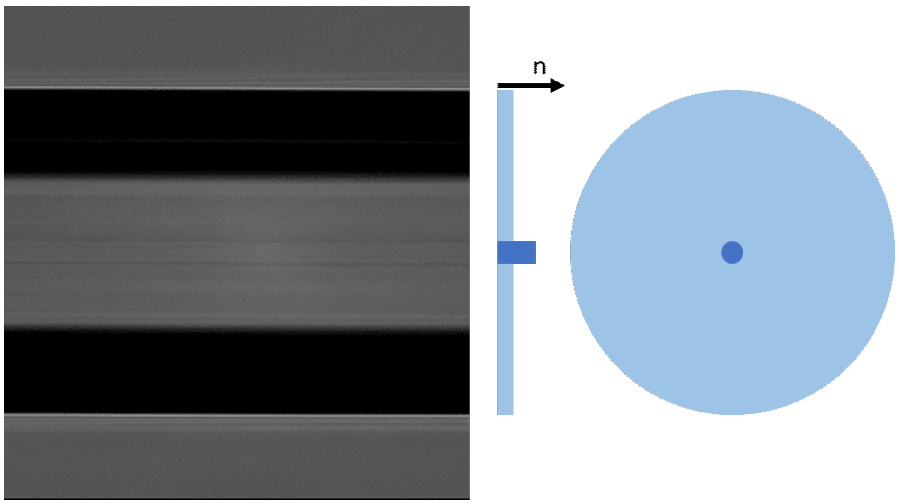

Figure 2.1: A seamless splice between two pieces of fiber as well as a schematic refractive index profile. The fiber depicted is the passive 20/400 µm fiber used throughout large parts of this thesis.

While the above described operating principle of total internal reflection is a good model for a quick understanding of the fiber, it is too simplistic to describe light propagation in detail. In the following, a more realistic model, based on Maxwell's equations is presented.

Core modes

Starting from Maxwell's equations, it is possible to obtain the nonlinear wave equation describing the propagation of the electrical field $\vec{E}$ in a dielectric medium without charges (Mitschke, 2005) or electric currents:

$$\nabla^2 \vec{E} = \frac{1}{c^2} \frac{\partial^2}{\partial t^2} \vec{E} + \mu_0 \frac{\partial^2}{\partial t^2} \vec{P} \tag{2.1}$$

with time t, speed of light c, vacuum permeability μ_0 and electric polarization $\vec{P}$. In the derivation of this, the paraxial approximation was employed. The assumption of a linear electric susceptibility and a weak absorption leads to the linear wave equation

$$\nabla^2 \vec{E} = \frac{n^2}{c^2} \frac{\partial^2}{\partial t^2} \vec{E} \tag{2.2}$$

where n is the refractive index of the medium (i.e. the glass). Due to the cylindrical geometry of the fiber, expressing this equation in cylindrical coordinates (r, ϕ, θ) is desirable. It is possible to use the following ansatz for the electric field:

$$\vec{E} = \vec{E}_0 e^{i\omega t} e^{i\beta z} R(r)\Phi(\phi) \tag{2.3}$$

with R denoting the field component normal to the fiber axis (z) in the radial direction, and Φ being the field component in the azimuthal direction. Additionally, β is the part of the wave vector parallel to the propagation axis (hereafter referred to as propagation constant) and ω is the central angular frequency of the electric field.

At this point, a separation of variables can be applied to the linear wave equation. This results in two equations, one for the azimuthal and one for the radial components:

$$\frac{\partial^2}{\partial \phi^2}\Phi + m\Phi^2 = 0 \tag{2.4}$$

$$r^2 \frac{\partial^2}{\partial r^2}R + r\frac{\partial}{\partial r}R + (\kappa^2 r^2 - m^2)R = 0 \tag{2.5}$$

where m is a constant and κ is the transverse part of the field propagation vector.

For continuous functions, Equation 2.4 has solutions with $m \in \mathbb{Z}$, which limits the number of solutions to the *Bessel equation* (2.5). The solutions to these equation are called *transverse modes*, since they define the shape of the allowed transverse distributions of the electric field in the fiber. The number of solutions to the equations above depends on the V-number of the fiber with core radius a and signal wavelength λ:

$$V = \frac{2\pi}{\lambda} aNA \tag{2.6}$$

The NA of the fiber is given by the difference of the refractive indexes of the core and cladding $NA = \sqrt{n_{core}^2 - n_{cladding}^2}$. For $V < 2.405$ there is only one solution, whereas for larger values more and more transverse modes are allowed. Figure 2.2 shows some modes that appear in a fiber with $V = 4.5$.

These mostly linearly polarized (LP_{mn}) modes are classified by two indexes m and n. The intensity profile of a mode has $2m$ azimuthal roots and $n - 1$ radial roots. The mode(s) in which the light travels along the fiber determines three important properties of the beam.

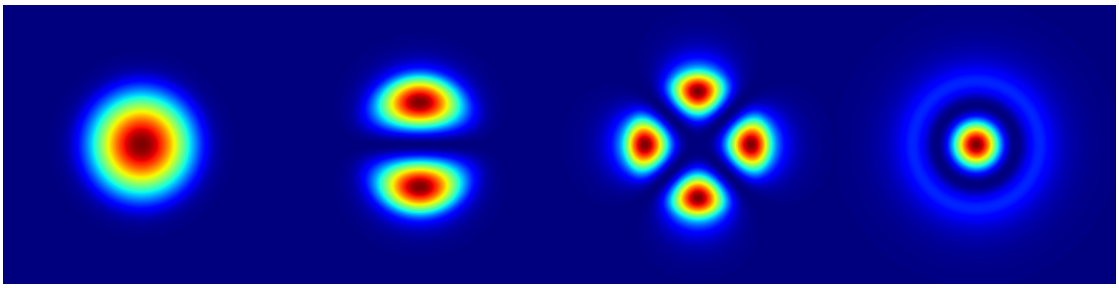

Figure 2.2: Calculated normalized intensity profiles of the transverse modes LP_{01}, LP_{11}, LP_{21}, LP_{02} (from left to right) for a fiber with $V = 4.5$.

The first one is the effective mode-field area A_{eff}, which is different for each mode. The fundamental mode FM LP_{01} has the smallest mode-field area, meaning that the light is confined to the smallest space in the glass. All other modes have a larger mode-field area due to larger transverse wavevectors which in turn results in an enlarged overlap with the cladding region.

The second property is the phase velocity since the different modes have slightly different effective refractive indexes, meaning that they travel through the fiber at different speeds. Thus, if two modes are simultaneously present within the fiber, a beating intensity pattern is created along the fiber, which will be of importance later.

The third property that changes with the mode composition of the beam is the beam quality, which is measured with the *beam propagation factor* M^2 (Siegman, 1998). This factor is proportional to the product of the beam waist size and divergence. Consequently, a beam with higher M^2 value has a considerable lower intensity (and larger cross section) after some free space propagation than a beam with lower M^2 value and the same beam waist size. For V-numbers not close to the mode cut-off, the FM has a $M^2 = 1$, whereas the first higher order mode HOM, the LP_{11}, has a $M^2 = 3$ in one axis and $M^2 = 1$ in the thereto perpendicular axis (Fu et al., 2010). It has to be noted that for a mode mixture of these two modes, the M^2 does not scale linearly with the fraction of the HOM (Fu et al., 2010; Yoda et al., 2009). However, many applications require a beam propagation factor of $M^2 \approx 1$, especially those applications that require a long, free space transmission of the beam. Another example are metal welding applications in which an excellent beam quality enables a reduction of the laser head size, including the scanning mirror size which allows higher scanning speeds. This not only reduces process time but also thinner and deeper welds can be achieved (Beyer et al., 2012). Such a low

beam propagation factor can only be achieved with low HOM content. This thesis is limited to the discussion of lasers with (close to) diffraction-limited beam quality.

Cladding modes

Similar to the fiber core, there are also distinct transverse modes in the cladding. Most of the fibers used in this thesis, are so-called *double-clad* fibers, that exhibit a large refractive index step from the cladding to the fiber coating. This, together with the large diameter of the cladding results in a larger *NA* of the fiber cladding. Consequently, a vast number of distinct transverse modes is guided in the latter. If the cladding has a circular symmetry, most of these modes have a vanishing overlap with the fiber core. The pump light that propagates in these modes is therefore not absorbed and does not contribute to the lasing process of a rare-earth doped fiber laser. Consequently, a circular symmetry is avoided for fibers with active gain medium (Leproux et al., 2001). The active fibers used throughout this thesis mostly have an octagonal or hexagonal cladding shape. This enables a strong pump absorption, which is necessary for high-power lasers that are discussed in the following subsection 2.1.2.

There are situations in which not all cladding light is absorbed, for example due to a short fiber length. Signal light in the cladding region can also be created through spontaneous emission or high propagation losses of core modes whose fields then leak into the cladding. This cladding light can be troubling as it has a higher NA than the core light, resulting in a degradation of the overall beam quality and can lead to unwanted heating of optical elements after the fiber output. This cladding light can be eliminated by deploying a cladding light stripper CLS. These devices rely either on geometrically enlarging the cladding via index matching (glue, silicon) or on scattering (etching, shaping grooves into the cladding). Both methods are used in the experiments presented within this thesis.

2.1.2 High-power fiber lasers

With the above described geometry of active fibers, it is possible to build high-power laser systems. There are several rare-earths that can be used as active dopants that all show different emission bands. Among them are

Ytterbium (Yb) with an emission band at around 1.05 µm, Erbium (Er) at around 1.55 µm and Thulium (Tm) at around 1.8 − 2.2 µm. Throughout this work, Ytterbium (Yb) is mainly considered as an active gain medium, since the highest output powers have been achieved with this material (Zervas et al., 2014). The reason for that and further details on this laser active material will be explained in section 2.3.

There are two different kinds of Yb-doped fiber laser systems: High-power oscillators and master-oscillator power-amplifier (MOPA) systems. Oscillators are typically formed by writing a Fiber Bragg grating (FBG) into the fiber core at each end of an active fiber (or a passive fiber, which is spliced to the active fiber) forming a cavity (Krämer et al., 2019). These systems have shown average output powers up to 5 kW (Möller et al., 2018; Ye et al., 2019). In particular the system presented by (Möller et al., 2018) was limited by SRS, which is explained in more detail in subsection 2.2.2. Unfortunately, these oscillators have a broad spectral linewidth of several nm, which is disadvantageous in many applications.

A narrower linewidth can be achieved by MOPA systems. There, a low-power oscillator provides a seed signal that is amplified in one or more amplification stages to high output powers. This method provides high flexibility as the seed laser can be easily modified. The benefit of such a system is that the coherence properties of the seed laser are transferred to the amplified signal, enabling narrow linewidths. Unfortunately, these systems typically reach lower output powers than the oscillators, due to the onset of transverse mode instability (TMI) (Möller et al., 2018). The effect of TMI is explained in more detail in the following section 2.3. MOPA systems have reached output powers of 4.3 kW (Beier et al., 2017a).

Operating fiber lasers at such high powers leads to several features compared to low-power operation. Naturally, if a large amount of pump energy is converted, and the conversion efficiency is not 100 %, a large amount of heat can be generated. Consequently, thermal effects are present in high-power fiber laser systems, which is why they will be discussed in more detail in section 2.3. Besides that, high powers lead to high intensities, which results in the onset of several *nonlinear effects*. Their origin and consequences are discussed in the following.

2.2 Nonlinear propagation of light and SRS

While the linear description presented in Equation 2.2 explains the different transverse modes observed in optical fibers, it does not describe correctly the propagation of fields with strong intensities. In fact, high-power fiber lasers show strong intensities and are, therefore, prone to induce nonlinear effects. This implies that the electric polarization $\vec{P}$ of the glass does not depend linearly on the electric field $\vec{E}$. $\vec{P}$ incorporates higher orders of the electric susceptibility tensor χ, most importantly the third order:

$$\vec{P} = \epsilon_0 \left(\chi^{(1)} \vec{E} + \chi^{(3)} \vec{E}\vec{E}\vec{E} \right) \tag{2.7}$$

This is because the second order term vanishes as glass is a centro-symmetric material (Boyd, 2008). The small fiber core sizes and/or high powers result in a strong electric field intensity present in the fiber core. This causes strong nonlinear effects, which degrade the optical output and can, even, cause the destruction of the fiber. Nonlinear effects arise from different phenomena. An important one is that the energy potential of the electrons moved by the electric field of the laser beam does not behave as a harmonic oscillator. Additionally, the glass medium forming the fiber does not always act instantaneously but has some memory. This is, for example, caused by molecular vibrations which lead to SRS. The nonlinear Schrödinger equation (NLSE) is used to adequately describe the propagation of a light field in a nonlinear optical fiber.

2.2.1 Nonlinear Schrödinger equation

The nonlinear Schrödinger equation describes how the field amplitude A changes in the fiber as a function of time t and longitudinal fiber position z. The derivation of the NLSE from the nonlinear wave equation Equation 2.1 is textbook knowledge (Agrawal, 2013). Here, only the result of this derivation is presented:

$$\frac{\partial A}{\partial z} = -\frac{\alpha}{2} A - \Big(\sum_{n=1} \frac{i^{n-1} \beta_n}{n!} \frac{\partial^n}{\partial t^n} \Big) A + i\gamma \Big(1 + \frac{i}{\omega_0} \frac{\partial}{\partial t} \Big) \Big(A \int_0^\infty R(t') \big| A(t-t') \big|^2 \mathrm{d}t' \Big) \tag{2.8}$$

For a better understanding of this equation, the individual terms of the right-hand side (RHS) are discussed in the following.

The first term describes loss along the fiber. If the RHS would be composed only of this term, a decaying exponential function would be the solution of the equation. Thus, the pulse amplitude would decrease along the fiber, following the Lambert-Beer's law with absorption constant α.

The second term incorporates chromatic dispersion. The first order means that the pulse amplitude (envelope) travels with a velocity of $v_g = \frac{1}{\beta_1}$. However, the pulse might consist of different frequencies. Thus, depending on the medium, these frequencies can travel at different velocities. This group-velocity dispersion is given by β_2. Often (and in the following chapter), the dispersion parameter $D = -\frac{\omega_0^2}{2\pi c}\beta_2$ is used to express the group velocity dispersion. Within the scope of this thesis, orders higher than $n = 2$ are neglected since the spectral width of the lasers investigated is rather narrow.

In the following chapter, dispersion is of high importance. Therefore, it is key to understand its origin. Light of different frequencies travels with different velocity inside the fiber because the refractive index of glass is frequency-dependent. The refractive index profile can be calculated from the optical absorption spectrum of the medium with the help of the Kramers-Krönig relations (Hutchings et al., 1992). A hypothetical absorption spectrum independent of the optical frequency would lead to a frequency-independent refractive index, which would lead to a dispersion free medium. Silica glass, however, has strong absorption bands both in the ultra-violet wavelength region and in the mid infra-red. This is because in the ultra-violet, the photon energy is high enough for direct electronic excitation and in the mid infra-red the photon energy is resonant with vibrational excitations. As the absorption spectrum is frequency dependent, so is the refractive index, which causes significant dispersion in optical fibers.

The third term on the RHS of Equation 2.8 describes all non-linearities characterized by the nonlinear parameter γ:

$$\gamma = \frac{\omega_0 n_2}{c A_{\text{eff}}} \tag{2.9}$$

with the effective mode area A_{eff}, the central frequency ω_0 and the nonlinear refractive index coefficient n_2. These non-linearities are self-steepening, Raman scattering and self-phase modulation (SPM) . Self-steepening is caused by

the dependency of the group velocity of the electric field on the intensity. It is incorporated into the NLSE Equation 2.8 by the term containing the partial derivative with respect to time, within the nonlinear section proportional to γ and the effect distorts an optical pulse travelling within an optical fiber in that the trailing edge becomes steeper. Raman scattering is of capital importance for this thesis and, therefore, is described in more detail in the following subsection 2.2.2. SPM is explained in subsection 2.2.3.

A further, instructive discussion of the (NLSE) (in a reduced form) is given by (Felice, 2016). The numerical implementation and program used therefore are discussed in more detail in subsection 2.2.4.

2.2.2 Stimulated Raman Scattering

The most important nonlinear effect in the context of this thesis is stimulated Raman scattering (SRS). In the following, a short description of the physical process is given and the mathematical description in the NLSE Equation 2.8 is explained. This description is then simplified to a mathematical model that is commonly used in the calculations of Raman content of high-power fiber lasers.

If an electric field interacts with a molecule, it can excite vibrations of that molecule. As the excitation of the vibration needs some energy, the incident (pump) photon is transferred into a Stokes photon of lower energy. This effect is called *spontaneous Raman scattering* and was originally observed in liquids and crystals. If a molecular vibration is de-excited and a photon of higher energy is created, it is called anti-Stokes photon. The energy of the molecular vibration as well as the efficiency of the Raman scattering depend on the molecular symmetry and orientation, the binding energy, interaction with the surrounding material, etc. The Raman spectrum of fused silica (suprasil) and quartz is shown in Figure 2.3.

The spectral features are much narrower for quartz, as the molecular lattice is strictly regular and the molecules always show the same angles. In the amorphous fused silica, on the other hand, a much broader range of molecular angles exists, which is why the spectral features are much wider. From spectral measurements of fused silica formed by heavy oxygen or silicon isotopes, it is possible to identify the vibrations responsible for the different spectral features (Galeener et al., 1981; Galeener et al., 1983). The lines denoted with R, D_1, D_2

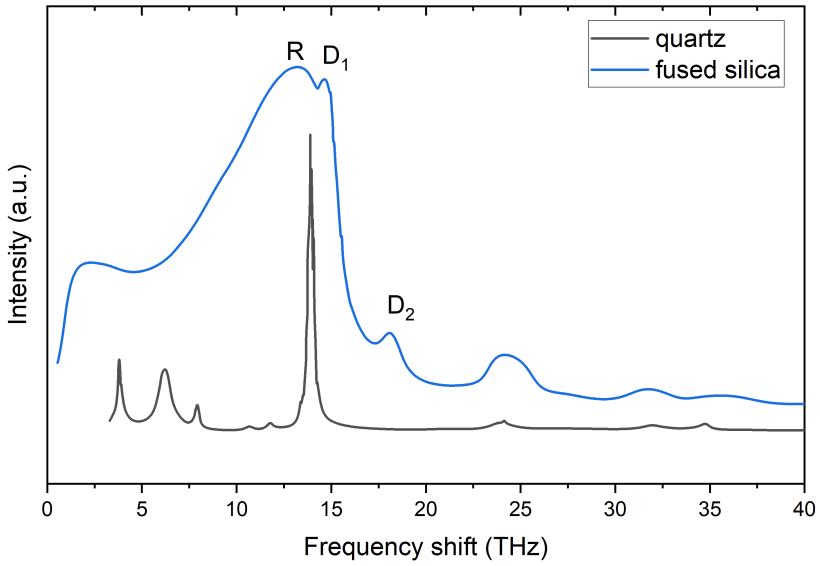

Figure 2.3: Measured Raman spectra of pure melt-quenched silica glass and of a quartz crystal (adapted from (Kalampounias, 2011)). Anti-Stokes photons are not depicted.

all stem mainly from motion of the oxygen, not the silicon. The lines $D_{1/2}$ are caused by breathing motions of 4- or 3-rings (Barrio et al., 1993). The broad R-line is caused by a bending motion of the molecule, with the oxygen moving along the bisector of the bridging angle between the two silicons (Galeener et al., 1981; Mishchik, 2012). Figure 2.4 illustrates these different motions.

If SRS occurs, the pump photons excite these vibrational motions and a Stokes photon is emitted. The vibrational motions can be transmitted to neighboring molecules and spread in the material, before they finally dissipate into heat. Therefore, the speed of this spread and the vibrational lifetime (i.e. the phonon propagation length) determine where this heat is deposited in the material. The phonon propagation length can be vastly different depending on the material structure: In a crystal structure such as quartz or diamond, it will be much higher than in an amorphous structure such as fused silica. (Korepanov, 2020) calculated the Raman spectra of silica for different propagation lengths and could reproduce the main features of the spectra of quartz and fused silica by changing the phonon propagation length. They determined the phonon propagation length of fused silica to be around 1 nm. As this length is

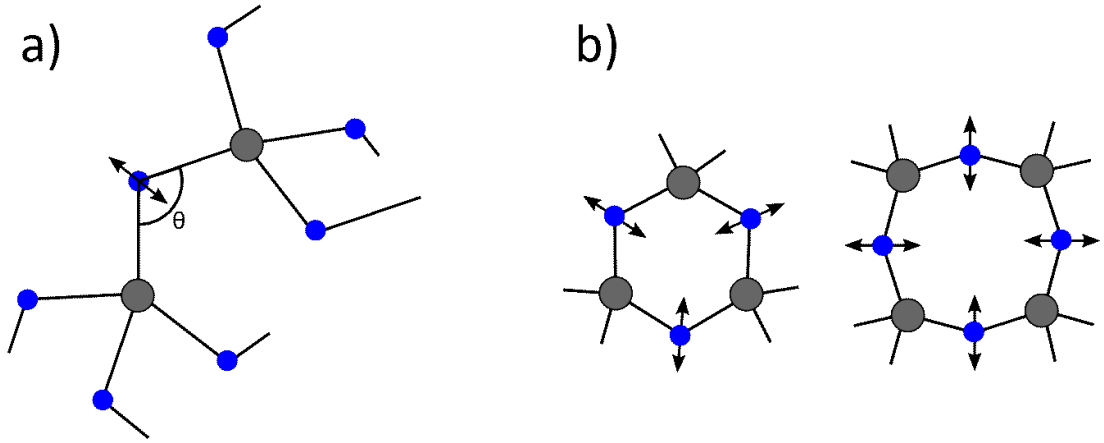

Figure 2.4: Schematic of the molecular vibrations causing Raman scattering in fused silica. The oxygen atoms are depicted in blue, the silicon atoms in grey. (a): Motion responsible for the R-line. (b): Motions responsible for the lines $D_{1/2}$. Please note that in fused silica many angles θ occur and the rings depicted in (b) are not planar.

short compared to the usual fiber geometry, it can be concluded that the heat created by the SRS effect is deposited in the material at the location where the pump photon is absorbed.

Mathematically, Raman scattering can be characterized by the *Raman response function* R as used in the NLSE (Equation 2.8). Even though the Raman gain profile depicted in Figure 2.3 is shown in frequency domain, it can also be expressed in time domain (Stolen et al., 1989). The physical interpretation is that the electrical field propagating in the fiber perturbs the polarizability of the glass. This perturbation is caused by two effects. First, the electronic structure of the molecules is changed due to the electric field. This change happens on short time scales so it can be assumed to be instantaneous. Second, the electric field may cause molecular vibrations, which happen on a much longer time scale. The two effects are included in the nonlinear response function, that takes the form

$$R(\tau) = (1 - f_R)\delta(\tau) + f_R h_R(\tau) \tag{2.10}$$

with time τ and Raman response h_R, that represents the molecular vibrations. The ratio f_R characterizes the relative strength the of instantaneous electronic and vibrational responses. The actual form of the vibrational response depends on the dopants used within the glass which can be modeled (Blow et al., 1989; Hollenbeck et al., 2002; Q. Lin et al., 2006). For this thesis, the simple descrip-

tion, presented by (Blow et al., 1989), was used to reduce the computational cost of the numerical calculations. Thus, h_R took the form:

$$h_R(\tau) = \frac{t_1^2 + t_2^2}{t_1 t_2^2} \exp(\tau/t_2) \sin(\tau/t_1) \tag{2.11}$$

with time constants $t_1 = 12.2\,\text{fs}$ and $t_2 = 32.0\,\text{fs}$. The factor f_R was chosen to be $f_R = 0.18$, as in (Hollenbeck et al., 2002). It has to be noted that, even though the time constants here are in the order of $\mathcal{O}(10\,\text{fs})$, this is not the lifetime of the molecular vibrations. The lifetime of these vibrations is much longer, in the order of $\mathcal{O}(1\,\text{ps})$ (Korepanov, 2020). In frequency domain these long time constants give rise to features that are very narrow compared to the Raman gain presented in Figure 2.3. However, in the glass structure of the optical fiber, the molecular bonding angles cover a broad range. Thus, many such narrow gain features combine to the broad Raman gain observed in Figure 2.3. This broad gain can be approximated by the short time constants $\mathcal{O}(10\,fs)$.

While the vibrational part of the nonlinear response R (proportional to f_R) describes Raman scattering, its electronic part describes the effects of self-steepening, that has been explained above, and SPM, that is explained in more detail in subsection 2.2.3.

At this point, all terms of the NLSE have been described. However, in the case of a pronounced Raman effect along the optical fiber, the created Stokes signal co-propagates with the Raman pump and their mutual interaction is described by a set of coupled amplitude equations. In the cw-case, and neglecting loss, dispersion and further nonlinear effects besides SRS, these equations can be considerably simplified to describe the change in the pump and Stokes intensity $I_{P/S}$ along the fiber (Agrawal, 2013):

$$\frac{\mathrm{d}I_P}{\mathrm{d}z} = -g_R \frac{\omega_P}{\omega_S} I_P I_S \tag{2.12}$$

$$\frac{\mathrm{d}I_S}{\mathrm{d}z} = g_R I_P I_S \tag{2.13}$$

with the Raman gain coefficient g_R. This gain is a measure for how likely it is that SRS occurs, if both pump and Stokes radiation are present. For fused silica $g_R \approx 1 \cdot 10^{-13}\,\text{m/W}$ at a wavelength of $\lambda = 1\,\mu\text{m}$ and scales inversely with the pump wavelength. This can lead, in the case of a high (undepleted) pump intensity, to an exponential increase of the Stokes intensity. For a beam

with effective mode area A_{eff}, instead of using the intensity $I_{p/S}$, this growth can be expressed in terms of power $P_{p/S}$, which leads to a evolution of the Stokes power along the fiber following

$$P_S(z) = P_{S_0} \exp\left\{\frac{g_R P_p z}{A_{\text{eff}}}\right\} \tag{2.14}$$

with P_{s_0} being the initial Stokes seed.

The exponential behavior is especially problematic in high-power fiber lasers as P_p is large and A_{eff} small. In those systems spontaneous Raman scattering creates an initially small Stokes seed that can be strongly amplified. Through this strong gain, large power fractions can be shifted to undesired wavelengths and hence SRS is a limitation for high-power fiber lasers (Zervas, 2019). This is discussed in more detail in chapter 3.

On the other hand, the strong and spectrally broad Raman gain can be used to access wavelengths unreachable by active ion doping, which is explained in more detail in section 2.4.

2.2.3 Additional nonlinear effects in optical fibers

Subsequently, additional important nonlinear effects present in high-power fiber lasers are briefly explained, following the descriptions found in standard textbooks (Boyd, 2008; Agrawal, 2013).

Self-phase modulation

The third order electric susceptibility results in a correction term n_2 to the total refractive index n of the material:

$$n = n_0 + n_2 \cdot I \tag{2.15}$$

where I is the field intensity and n_2 is connected to the third order electric susceptibility by:

$$n_2 = \frac{3\chi^{(3)}}{8n_0} \tag{2.16}$$

This dependency of the refractive index of the material on the intensity is called the *optical Kerr effect*. For fused silica at a wavelength around 1 µm, $n_2 \approx 2 \cdot 10^{20} \frac{\text{m}^2}{\text{W}}$ (Kabaciński et al., 2019). If we assume an area of the beam of

$A = \pi(10\,\mu\text{m})^2 \approx 300 \cdot 10^{-12}\,\text{m}^2$, the optical power necessary for the correction to reach local values of 10^{-5} (non-negligible compared to the refractive index step between fiber core and cladding) are in the order of $\mathcal{O}(150\,\text{kW})$. These high values are far beyond the current capability of high-power cw fiber lasers. However, the interaction length of the electric field with the medium is long in fiber lasers. Thus, small refractive index differences can add up to significant amounts, especially if the instantaneous phase of the electric field changes due to refractive index differences. The nonlinear phase can be estimated by the *B-intergral* for a fiber of length L:

$$B = \frac{2\pi n_2}{\lambda} \int_0^L I(z)\, dz \tag{2.17}$$

This nonlinear phase manifests itself as self-phase modulation SPM. The peak of an intensity modulation travelling through a fiber experiences a different refractive index than its flanks (following Equation 2.15) and, consequently, a different nonlinear phase. As the instantaneous frequency of the light is the time derivative of the phase, new frequencies are created at the front and rear flanks of the pulse. This symmetric spectral broadening can be observed in many narrow-linewidth high-power fiber laser systems (even cw as there are still resiudal power fluctuations on very short time-scales). SPM is the main reason for the broadening of the spectral width with an increase of the output power in a given system. To avoid SPM, the B-integral has to be kept low, which is why short fiber lengths are preferred (this is valid for all optical nonlinear effects). This is also the reason why counter-pumping is preferred over co-pumping, as co-pumping leads to a rise of the intensity earlier along the fiber.

Four-wave mixing

Four-wave mixing (FWM) is a process where two photons of frequency ω_1 and ω_2 are annihilated and two new photons are created with frequencies ω_3 and ω_4 in a way that fulfills energy conservation:

$$\omega_1 + \omega_2 = \omega_3 + \omega_4\,, \tag{2.18}$$

Momentum conservation has to be fulfilled as well, meaning that the wave-vectors (or propagation constants, for the same propagation direction) have to

match:

$$\beta_1 + \beta_2 = \beta_3 + \beta_4 \tag{2.19}$$

This so-called phase matching condition is fulfilled thanks to the dispersion of the given fiber. In fiber lasers *degenerate four-wave mixing* is often observed, where $\omega_1 = \omega_2$ and two new spectral features occur symmetrically in frequency around the central line. Such spectral features are observed in some of the experiments presented in this thesis. However, the efficiency of this process is often moderate, which is why the resulting loss in spectral purity can be tolerated most of the times.

Stimulated Brillouin Scattering

While in the above described effects of SPM and FWM all the energy remains in the form of (guided) photons, there are also inelastic scattering effects like SRS. Here a photon scatters with a phonon and a photon of less energy is emitted. Stimulated Brillouin scattering (SBS) is another inelastic scattering effect. Its origin is *electrostriction*, i.e. the tendency of the glass to become compressed in the presence of an electric field. Brillouin scattering can also happen spontaneously in the form of sponteaneous Brillouin scattering. The latter is the spontaneous scattering of a photon with a thermally excited acoustic wave inside the material. The incident and scattered photons than beat with each other, causing a density variation inside the material through electrostriction. As density variations correspond to refractive index changes, a moving refractive index grating is formed within the fiber, with a periodicity corresponding to the frequency difference between the incident (pump) and the scattered (signal) photons. This grating can reflect photons, which will reinforce the density changes, which scatters more photons, etc. This process results in a large signal pulse travelling within the fiber in the backwards direction. In an active fiber, this pulse can also be amplified to even higher pulse peak powers. Such a pulse can cause the destruction of the glass in the fiber core, which not only destroys the fiber, but can cause severe damage to the whole fiber laser system.

SBS can be detected through an increase of the backwards propagating power and through the presence of short pulses in this backwards propagating signal. These methods are used in many experiments presented within this thesis. Different SBS suppression techniques have been developed (Kobyakov et al., 2010). In general the SBS gain decreases for shorter fibers, larger core

sizes and broader spectral pump linewidths.

2.2.4 Numerical illustration of the nonlinear effects

The numerical solutions of the NLSE presented within this thesis are performed with a commercial software (fiberdesk, 2021) that implements a split-step Fourier method. For a clear understanding of the non-linear effects present in an optical fiber, a simulation is presented in the following. Hereto, the field amplitude of a single Gaussian-shaped pulse with a FWHM of 20 ps, a peak power of $P_p = 5\,\mathrm{kW}$ and a central wavelength of 1060 nm is propagated along 10 m of a passive 20/400 µm fiber.

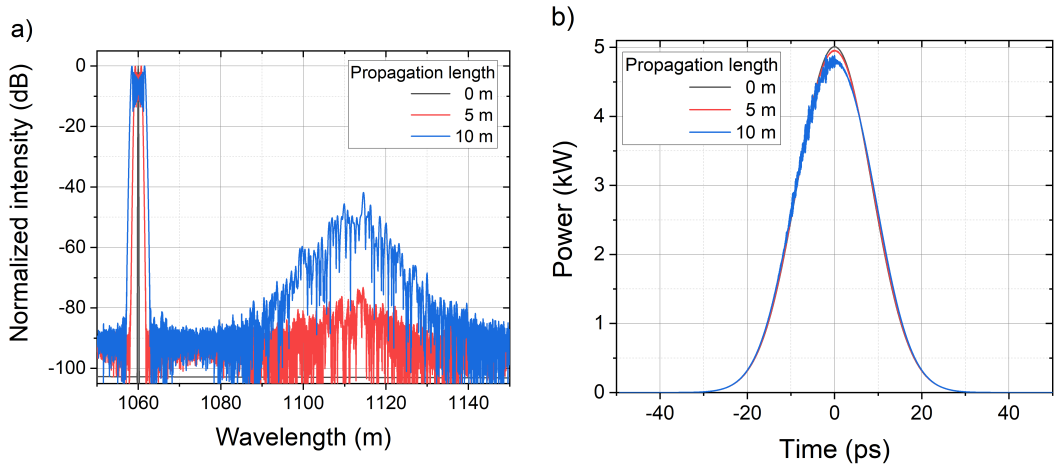

Figure 2.5: Development of the optical spectrum (a) and corresponding pulse (b) as the signal propagates along a fiber.

The initial optical pulse shape and spectrum are compared to the ones after 5 m and 10 m propagation length in Figure 2.5. There are several effects visible: First, the optical spectrum experiences significant broadening around the signal wavelength. This is caused by SPM. In fact, SPM does not only broaden the spectral peak, but also gives it a symmetric fine structure. This is caused by the accumulated nonlinear phase shift reaching values higher than $\Phi = 1.5\,\pi$ (Stolen et al., 1978). Additionally, a Raman peak appears at around 1117 nm. The noisy structure of this peak originates from the initial quantum noise seed, which will be discussed in more detail later. Furthermore, after propagation, the temporal pulse shape shows a structure on the leading pulse edge. This effect and further details of the simulation will be of importance in chapter 3 and will be discussed there.

2.3 Thermal effects and TMI

This section explains the origin of the heat load within the fiber and then proceeds to detail the impact of this heat load on the fiber laser.

Heat sources

There are three main processes that lead to heat deposition in the fiber: background loss, quantum defect and photodarkening.[1]

Background loss, which is explained in great detail in (Kirchhof et al., 2005), can be caused by impurities of the glass (mainly OH-content for Yb- and Tm-doped systems) and all its dopants neccessary, for example, to increase the solubility of the rare-earth ions (such as Al for Yb). Typical background loss values in high-power active fibers are in the order of $\mathcal{O}(10\,\mathrm{dB/km})$ (Kirchhof et al., 2005). It can, therefore, be neglected for fiber lengths below 20 m.

The quantum defect QD is the energy difference between an absorbed pump photon and an emitted Stokes photon and can be calculated by:

$$QD = \frac{hc}{\lambda_{pump}} \cdot \left(1 - \frac{\lambda_{pump}}{\lambda_{signal}}\right) \tag{2.20}$$

This photon energy difference is deposited in the fiber in the form of heat. Thus, the heat deposition is strong in places of the fiber where many pump photons are converted to signal photons. The quantum defect is intrinsic to the laser process and is a major heat source in fiber laser systems. In fact it is one of the main reasons for Yb being able to emit the highest output powers among all rare-earths, since the emission and absorption spectra of the Yb^{3+}-ion responsible for the laser process are very close together. While the emission is strong at a wavelength around 1.05 µm, the absorption is strong around 915 nm and both are highly pronounced around 976 nm. This enables pumping at 976 nm, a wavelength where high-power laser diodes are available, and emitting around 1.06 µm, which leads to a QD of only 8 %.

Photodarkening is an effect which leads to a decreasing output power emitted by the fiber over laser operation time. Thereby, the fiber becomes *darker*, i.e. less transparent for the signal light. This is caused by the formation of color

[1] In Thulium-doped fibers, the quantum efficiency, meaning how many active ions are excited per pump photon absorption, is relevant as well.

centers that absorb the light (Koponen et al., 2006). While this absorption is much stronger in the visible wavelength range, it is still present at a wavelength of 1 µm. Here it is key to realize that the total energy of the absorbed photon eventually dissipates into heat, which results in photodarkening becoming a major contributor to the total heat load within the fiber (Jauregui et al., 2015; Šušnjar et al., 2018). Since the effect is of such high importance, many ways of mitigation have been studied, such as changing the active doping concentration or co-doping with other materials (Jetschke et al., 2012; Zhao et al., 2017), photobleaching (meaning the irradiance with visible light (Cao et al., 2019)) or loading with hydrogen (Engholm et al., 2008) or deuterium (Zhao et al., 2019).

Consequences of the thermal load

The high thermal loads in a fiber created by either absorption, quantum defect or photodarkening have several effects on the laser performance. To reduce the heat load through absorption, a clean environment is necessary during the production of the high-power fiber and laser system. The same holds true for all optical surfaces and coatings that the high-power beam encounters. A temperature increase here leads to a thermal lens, since the refractive index of fused silica is dependent on the temperature T via the *thermo-optic coefficient* $\frac{\mathrm{d}n}{\mathrm{d}T}$. Such a thermal lens results, for example, in a power-dependent change of the beam focusing, which is highly undesirable. However, a thermal lens can also form inside of the fiber via the same thermo-optic coefficient, as the refractive index profile determines the shape and number of the guided core modes, as described in subsection 2.1.1. In that case, the heat deposited in the fiber core increases its temperature, which raises the temperature of the other fiber regions through heat transfer. The temperature distribution is time-dependent, but since the optical fibers are long and thin, a thermal steady state is quickly reached in single-mode operation (Davis et al., 1998). In the case of the heat density Q being deposited only in the fiber core (e.g. neglecting any pump background loss), and neglecting the fiber coating, an analytic formula for the refractive index change of a fiber with core radius a and cladding radius b was derived (Brown et al., 2001) as a function of the radial position r. For the fiber core:

$$\Delta n(r) = Q\frac{\mathrm{d}n}{\mathrm{d}T}\frac{a^2}{4k}\left(1 + \frac{2k}{bh} + 2\ln\left(\frac{b}{a}\right) - \frac{r^2}{a^2}\right) \tag{2.21}$$

where k denotes the thermal conductivity and h is the heat transfer coefficient between the cladding and the outer region. For the fiber cladding on the other hand:

$$\Delta n(r) = Q\frac{\mathrm{d}n}{\mathrm{d}T}\frac{a^2}{2k}\left(\frac{k}{bh} - \ln\left(\frac{r}{b}\right)\right) \tag{2.22}$$

In the derivation of these formulas, stress induced into the glass by a refractive index change has been neglected. The equations show that the refractive index change in the core acquires a parabolic profile with the radius, whereas it decreases in a logarithmic way in the cladding. It also becomes clear that extreme fiber cooling (increasing h) is of limited use, since it only effects the refractive index offset but not its radial profile. This refractive index change causes a shrinking of the modes - a thermal lens within the fiber (Jansen et al., 2012).

For fused silica, the thermo-optic coefficient amounts to $\frac{\mathrm{d}n}{\mathrm{d}T} \approx 10^{-5}\,1/\mathrm{K}$ (Rocha et al., 2016), the heat conductivity is $k = 1.38\,\mathrm{W}/(\mathrm{m}\cdot\mathrm{K})$ and the heat transfer coefficient for forced liquid flow cooling $h = 10000\,\mathrm{W}/(\mathrm{m}^2\cdot\mathrm{K})$ (Dawson et al., 2008). For the 20/400 µm fiber used throughout this thesis, at a heat load of 30 W/m, corresponding to a heat density of $Q \approx 9.6\cdot 10^{10}\,\mathrm{W}/\mathrm{m}^3$, this leads at an exemplary distance of 5 µm from the fiber axis to a refractive index change of approximately:

$$\Delta n(r) = 1.4\cdot 10^{-4} \tag{2.23}$$

This value is not negligible compared to the index step in this fiber, which was measured to be $\Delta n \approx 1\cdot 10^{-3}$. Thus, the heat load can increase the V-number of the fiber and a single-mode fiber can become a fiber that allows for multi-mode guidance, which is neatly explained in (Mafi, 2020) and in (Hansen et al., 2011) [2]. Besides the radially symmetric refractive index increase of the core given by Equation 2.21, a non radially symmetric refractive index change can occur. The change can give rise to an effect which will be examined in main parts of this thesis: Transverse mode instability (TMI). This effect, introduced in more detail in the following section, is usually more critical than thermal lensing (Zervas, 2019), but thermal lensing can delay the onset of TMI (Dong, 2016).

[2] Even in a fiber that allows multi-mode guidance, a clear excitation of a single mode can cause this mode to be dominant. In reality there is usually a non-negligible coupling between different modes through fiber bending or impurities and shape irregularities.

Transverse mode instabilities

The effect of Transverse mode instability (TMI) causes a sudden degradation of the beam quality, once that an average power threshold has been reached. After the onset of TMI, the emitted beam profile fluctuates between different transverse modes on a millisecond time scale, usually in an unpredictable manner. This effect has been known for about a decade (Eidam et al., 2011) and has severely hampered the performance scaling of fiber lasers (Jauregui et al., 2020a). The effect has been mainly studied in Yb-doped systems, but has been theoretically predicted for Tm-doped amplifiers (A. V. Smith et al., 2016) and was recently observed in such a system (Gaida et al., 2021). TMI has been observed for continuous-wave and pulsed operations at high average powers (Beier et al., 2018; Eidam et al., 2011). The most common technique to determine the TMI threshold is to sample the output beam with a photodiode (Otto et al., 2012). If the beam profile is stable, no temporal signal variation is detected. In the case of TMI, strong intensity fluctuations are measured on the photodiode signal. To rule out the possibility that output power fluctuations of the laser system are responsible for the measured intensity variation, a second photodiode that measures the whole beam can be deployed. In the following, the current theoretical understanding of TMI is summarized.

For TMI to appear, there must be at least two modes in the fiber, e.g. the fundamental mode (FM) and a higher order mode (HOM), that are for simplicity hereafter identified with the previously shown LP_{01} and LP_{11}, respectively. An interference of these modes leads to regions with high intensity and regions with low intensity in the transverse cross section of the fiber. Since these modes have a different effective refractive index, they form a beating intensity pattern along the fiber. In regions with high signal intensity, more pump photons are converted. Consequently, those regions experience a higher heat-load via the quantum defect, which leads to an increase of the refractive index in these regions. In that way, the original mode interference pattern (MIP) leads to a refractive index grating (RIG) (Jauregui et al., 2012).

This RIG has the periodicity of the MIP, as it is caused by the latter. Thus it acts as a long-period grating. Such a long-period grating can transfer energy from one mode to the other, but only if a phase-shift exists between it and the mode interference pattern (A. V. Smith et al., 2011). The sign of this phase shift determines the direction of the energy transfer. For a positive phase shift

between the RIG and the MIP (i.e. the MIP is located earlier along the fiber than the RIG), the energy is transferred to the FM, while it is transferred to the HOM for a negative phase shift (Ward et al., 2012; Stihler et al., 2018). The modal coupling efficiency depends on both, the strength of the RIG and the amount of the phase shift. It has to be noted that for a given refractive index perturbation, the coupling efficiency from one mode to another decreases with the signal wavelength (Dong, 2013; Hansen et al., 2013). Furthermore, it is expected that an existing RIG does not only act upon the precise signal wavelength, but that its effect has some spectral width. Unfortunately, to date, no experimental study into the spectral width of the formed RIG has been presented.

In summary, the process of TMI happens as follows: Below the threshold power both MIP and RIG are present, but the RIG is too weak and/or the phase shift is too small to enable energy transfer between the modes. Once the power reaches the TMI threshold and the RIG is strong enough for a given initial phase shift, there is an initial energy transfer from FM to HOM. This changes the MIP present in the fiber, which causes the local heat load to change, which causes the RIG to adapt. The adaptation takes some time in the order of $\mathcal{O}(0.1\,\mathrm{ms})$. This adaptation leads to a weaker phase shift resulting in less energy being transferred from the FM to the HOM. As the MIP adapts, in turn, to the new RIG, even a positive phase shift is possible resulting in an energy transfer from HOM to FM. As a result of this continuous movement of the two gratings, a fluctuating mode composition can be seen at the fiber output. The thermal adaption time determines the fluctuation frequency in the kHz-region.

For this dynamic to happen, there has to be an initial phase shift. The origin of this initial phase shift is still debated (Jauregui et al., 2020a), but the most plausible one is intensity noise in either the signal or the pump. The TMI threshold could be significantly decreased in an experimental system with a modest increase of the pump intensity noise (Stihler et al., 2020). Figure 2.6, adapted from (Stihler, 2020) shows the formation of the RIG along a counter-pumped fiber core. Due to the counter-pumping, the signal intensity increases towards the fiber end and, thus, the MIP (a) is strongest there. This MIP results in a periodic pattern of the active ion inversion profile (b). In regions with strong signal intensity (maximum of MIP) many pump photons are converted to signal photons, leading to a low active ion inversion. Consequently, those re-

gions experience a high heat load resulting in a strong temperature grating (c) along the fiber. In the steady state presented here, the RIG directly mimics the temperature grating. To enhance the visibility of the RIG, the parabolic profile from Equation 2.21 was subtracted.

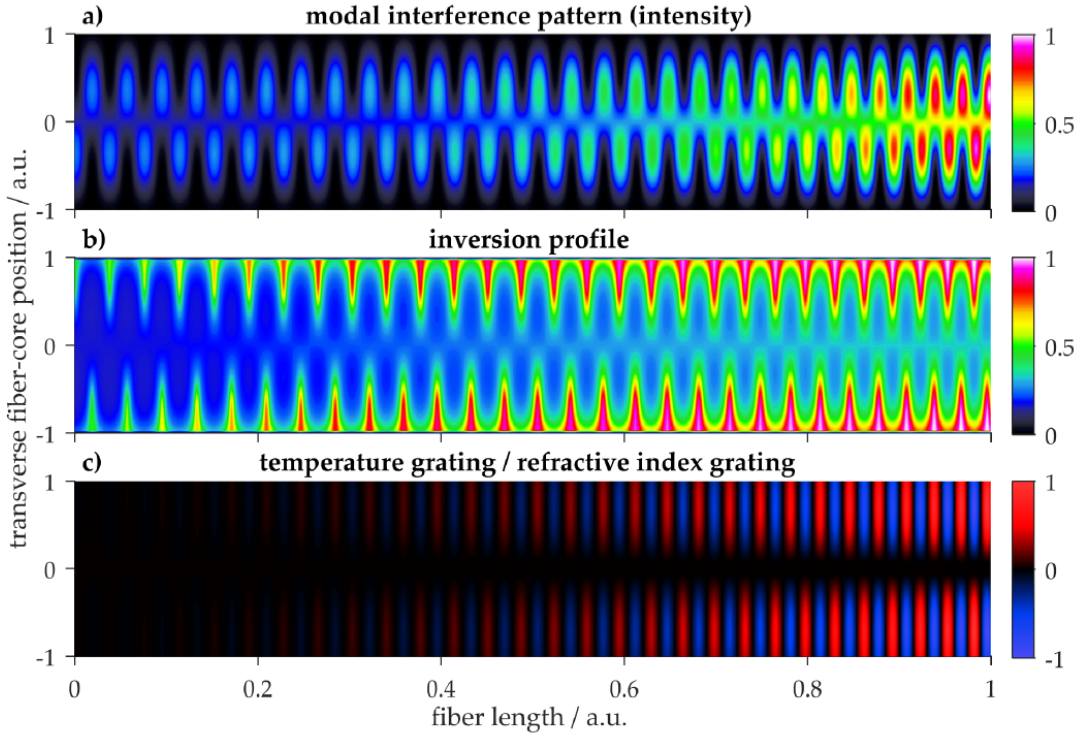

Figure 2.6: Exemplary modal interference pattern (intensity) created by the beating of the LP01 and the LP11 modes (a), corresponding inversion profile (b) and the resulting temperature/ refractive index grating (c) for a counter-pumped fiber. All profiles are normalized. Figure reproduced with kind permission from (Stihler, 2020).

Having understood the physical origin of TMI enables understanding the different experimental mitigation strategies proposed. They either act upon the MIP, the RIG or the phase shift.

A reduction of the phase shift is possible through noise reduction as described above. The phase shift can also be actively controlled for example by driving the laser in burst mode (Jauregui et al., 2020a). During the burst, the temperature of the fiber rises, a positive phase shift is achieved. Between two bursts, the fiber cools down, a negative phase shift occurs, but is not critical as there is no emission between the bursts. The temporal burst length however, is

not freely variable. Further techniques to control the phase shift are currently being developed (Jauregui et al., 2020b).

Another approach to mitigate TMI is to minimize the RIG by reducing the heat load. This can be achieved by reducing the quantum defect through tandem pumping (Zervas, 2019) or by minimizing the photodarkening (Johansen et al., 2013; Jauregui et al., 2015). Additionally, the refractive index also depends on the longitudinal absorption of the pump. Consequently, the ratio of co- and counter-pumping can also become important (T. Li et al., 2018). Decreasing the local heat load is also possible by decreasing the local pump absorption. This can be achieved for example by a lower active dopant concentration or a pump wavelength detuning. The dependency of the TMI threshold on the pump wavelength was shown both experimentally and theoretically (Tao et al., 2015c; Tao et al., 2015b; Jauregui et al., 2016). However, to achieve a similar amplifier efficiency, a lower local pump absorption has to be accompanied by an increased fiber length. In that way, the longer the fiber length, the higher the TMI threshold. The TMI threshold of a fiber could be significantly increased by increasing the fiber length (Beier et al., 2018).

The RIG can also be actively washed out, for example by pump power modulation which significantly increases the beam quality above the usual TMI threshold (Jauregui et al., 2018). However, the phase shift is only positive in one half of the modulation cycle, and FM operation is not continously achieved.

The third possibility is to reduce the MIP. A relatively new possibility to achieve this, is using polarization maintaining fibers, in which linear polarized light is coupled with an angle of 45 to the fiber polarization axes (Lai et al., 2020; Jauregui et al., 05.03.2021). Since the beat length of the FM and HOM is different in the two axes of the fiber, the MIP is periodically washed out. Another way to reduce the MIP is to reduce the HOM content. An increase of the TMI threshold was achieved through HOM content reduction by either directly lowering the V-number of the fiber or by bending of the fiber (Tao et al., 2015a; Beier et al., 2017a; Beier et al., 2018). A reduction of the V-number is possible through a lower NA or a smaller core size as seen in Equation 2.6. Lowering the fiber NA decreases the guiding strength, which increases the fibers susceptibility to bend losses and, therefore, requires larger bending diameters. This can be undesirable as it increases the packaging size of the laser system. A smaller core size, on the other hand, enhances nonlinear effects as discussed in the previous section.

Despite this large set of TMI mitigation strategies, to date, the effect of TMI remains a challenge and further scaling the output power of fiber lasers still requires carefully balancing TMI and nonlinear effects, notably SRS. Indeed, the two effects are not independent of each other and the interplay between TMI and SRS is studied in detail in chapter 5. This interaction is especially important in cases where a strong SRS effect is present. This is the case in Raman fiber amplifiers that are described in the next section.

2.4 Raman fiber amplifiers

As mentioned in section 2.1, the wavelengths accessible by usual fiber lasers are limited to the emission regions of the active dopants used. These are mainly the comparatively small bands around 1.05 µm (Yb), 1.55 µm (Er) and 1.8 − 2.2 µm (Tm). The output power of Yb-doped fibers is much larger than for other rare-earth ions (Zervas et al., 2014). One reason for that is the relatively small quantum defect in Yb, which leads to a high efficiency and low thermal load as explained in section 2.3. However, the wavelength band of Yb-doped lasers has a severe drawback: the damage caused by light to the human retina is much more critical at 1 µm than at wavelengths beyond 1.4 µm. Eye safety is crucial for many applications that require laser transmission through open air such as laser radar, remote sensing and rangefinding (Hecht, 2008). SRS offers a possibility to overcome these obstacles as it enables an energy transfer to longer wavelengths, albeit with some energy loss through the additional quantum defect. This technique is used in a Raman fiber amplifier (RFA). It is worth noting that the Raman shift can also be used multiple times and systems using this are called *cascaded Raman lasers*.

RFA operate in a similar way as rare-earth doped fiber amplifiers: a low-power seed signal (for example generated by an external cavity diode laser) and the signal of a high-power pump are fed into an optical fiber. Here, the seed is amplified following Equation 2.13 to high output powers. The broad R-line of the Raman gain g_R (see Figure 2.3) is benefitial for this, as it enables tuneability of the Stokes wavelength with the same pump wavelength. A standard application is generating a Stokes wavelength of 1176 nm, which can then be frequency-doubled to interact with the sodium-line, which is useful to create a laser guide star for adaptive optics in astronomical observatories (Feng et al., 2009; Enderlein, 2020). Another import application of Raman lasers is

in-band, high-brightness pumping of other fiber lasers, especially Er-doped ones (Nicholson et al., 2010; Zhou et al., 2017). Here the QD in the last amplifier stage can be reduced from 40 % (laser diode pumping) to 4 % (in band pumping). These applications demand high-power Raman lasers, which is why they attracted substantial research interest, which has resulted in several kW-level RFAs with beam quality $M^2 > 2.5$ having been reported recently (Glick et al., 2018; Chen et al., 2020a). A better beam quality of $M^2 \approx 1.5$ was achieved by a hybrid Yb-Raman system with a record output power of 3.9 kW, albeit with a very large 3 dB-linewidth of 7.6 nm due to the long total active fiber length of 50 m. Very recently another hybrid Raman fiber amplifier with smaller linewidth showing kW level output powers was reported, limited by the onset of TMI (Zhang et al., 2020). Chapter 4 includes investigations on a narrow-linewidth RFA with excellent beam quality, before a high-power RFA is implemented and the interplay between SRS and TMI is investigated in chapter 5.

3 Dependence of SRS content on spectral linewidth of broad-band cw light

High-power, few-mode fiber laser systems are inherently prone to nonlinear optical effects due to the high field amplitudes propagating in the fiber and the long interaction length with the fiber as described in section 2.2. Among these nonlinear effects, SRS plays an important role, since it is a performance limitation of fiber lasers with good beam quality ($M^2 < 1.5$) as shown by (Zervas, 2019).

The SRS process is especially relevant for continuous wave multi-longitudinal mode fiber laser sources and in particular for high-power fiber oscillators. These oscillators have shown record output powers of more than 5 kW in the Yb-gain region and are currently limited by SRS (Möller et al., 2018; Liu et al., 2016). Consequently, the main goal in these systems is to reduce the SRS content.

An approach to achieve this goal is to introduce long period gratings into the fiber. These gratings act as a spectral filter for the Stokes signal (Jansen et al., 2009). However, they have some insertion losses at the signal wavelength and may reach critical temperature levels. During the course of this thesis, improved long period gratings were tested in a high-power fiber laser system (Heck et al., 2018). The grating was written into a passive fiber, that was spliced to the output end of the laser system. It was found that the grating experienced a thermal load of about 21 K/kW, and suppressed up to 98 % of the signal at resonance. Unfortunately, the resonance of these gratings is rather narrow and, therefore, the overall reduction of Stokes content was approximately 50 %. A further filtering would require additional gratings, as the filtering effect scales

linearly. The filters work more effectively when placed along the amplification fiber (Jansen et al., 2010), however, up to date, the gratings can only be directly written into the passive fiber if high heat-loads or insertion losses are to be avoided. Consequently, this spectral filtering technique is not likely to be widely adopted as long as writing the filters in the active fiber -preferable through the fiber coating- is deficient.

Another way to reduce the SRS content of high-power fiber oscillators is to change their spectral width. Prior to this thesis, it was experimentally observed that the spectral width of the output grating of such a fiber oscillator influences the Raman content by several orders of magnitude (Schreiber et al., 2014). However, there has not been an explanation for this behavior until now. In this section, such an explanation will be given. Thereto, the influence of the spectral width of cw lasers on the SRS content is reviewed in section 3.1. It will then be explained and quantified with a simple analytical model and an enhanced walk-off model is presented in section 3.2. The application domain and boundary conditions of the model are detailed in subsection 3.2.1. Furthermore, the influence of the temporal field characteristics on the Raman content is investigated in more detail in subsection 3.2.2. Several aspects that have to be followed for the correct simulation of SRS are also discussed.

Finally, a conclusion is drawn in section 3.3 that gives guidelines for future fiber laser systems.

3.1 Recent research on the influence of spectral grating width of cw lasers on the SRS content

It has been experimentally discovered that the Raman content of high-power fiber oscillators depends on the spectral width of their grating (Schreiber et al., 2014). In the experiment, a 20 m long, 20/400 µm Yb-doped fiber with an FBG on each side formed an oscillator. One grating had a reflectivity of 99 % and a spectral width of 3.5 nm. The second grating had a reflectivity of 10 % and a spectral width of 1.5 nm, 0.5 nm or 0.04 nm. Additionally, the oscillator was tested without an output grating, with the broad-band Fresnel reflection serving as the oscillator feedback. The observed SRS content at an output power of 760 W ranged approximately from 3 % (narrowest grating) to 2×10^{-5} % (Fresnel relfection).

The observation of the bandwidth-dependence of the Raman content was experimentally confirmed by (Liu et al., 2016). The observation was extended to different spectral shapes (Brochu et al., 2017; Wang et al., 2017; Xu et al., 2017) and chirp-moiré fiber Bragg gratings (W. Lin et al., 2018). In master oscillator power amplifier systems, the influence of different seed sources was also studied (Liu et al., 2017). In the above-cited works, the temporal characteristics of the Raman pump field have attracted more and more attention and promising attempts to directly control the temporal characteristics to suppress SRS have been made (T. Li et al., 2019). There, different seed oscillators were amplified to output powers in the kW-level. It was specifically noted that the length of the temporal features of the field amplitude is important. A field with fewer, longer features will result in a higher SRS content than a field with more frequent but shorter features. This thesis shows that walk-off between the Raman pump and the Stokes signal can explain the observed behavior.

3.2 Derivation of an analytical cw SRS model incorporating walk-off

A closer look at the simulation shown in Figure 2.5 suggests that walk-off plays an important role in the Raman process. This is because the depicted pulse develops a structure on its leading edge as it propagates through the fiber. Crucially, if the Raman effect is switched off in the numerical calculation, this structure does not appear. Therefore, it stems from a superposition of the Raman pump and the Stokes signal. Qualitatively this behavior can be described in the following way: As the Stokes signal travels faster along the fiber, it overlaps with the leading edge of the pump pulse. There, the Raman pump intensity is significantly lower, which results in a lower Raman gain of the Stokes signal.

Describing this effect quantitatively is more difficult since the NLSE (Equation 2.8) incorporating the effect of Raman scattering and walk-off does not have an analytical solution for arbitrary input fields. Therefore, describing the influence of walk-off in a fiber on SRS usually requires numerically solving Equation 2.8, which is very time consuming. For example, the numerical illustration presented earlier in Figure 2.5 took several hours to complete. However, (Christodoulides et al., 1989) derived an analytical formula in the case of a sin-

gle pulse propagating along a fiber, causing SRS and undergoing walk-off, in a loss-less case without pump depletion. Equation (38) in (Christodoulides et al., 1989) describes the intensity profile of a resulting Stokes pulse. Integrating over this pulse would give the total Stokes power, but this is not possible in an analytically simple form. However, in equation (40), (Christodoulides et al., 1989) the peak intensity $I_{S,max}$ of the Stokes pulse is given, which is linked to the Raman pump pulse duration τ and given by equation:

$$I_{S,max}(z) = s_0 \cdot \exp\left(a \cdot \tau \cdot \tanh\frac{b(z)}{\tau}\right) \tag{3.1}$$

where

$$a = \frac{2\, g_R\, P_P}{A_{\text{eff}}\, D\, \Delta\lambda_{PS}} \tag{3.2}$$

and

$$b(z) = \frac{D\, \Delta\lambda_{PS}\, z}{2} \tag{3.3}$$

with Raman gain coefficient g_R, effective mode area A_{eff}, fiber dispersion D, Raman pump peak power P_P, wavelength difference between Raman pump and Stokes $\Delta\lambda_{PS}$, fiber position z and initial Stokes intensity s_0. The Stokes peak power follows from this equation through an integration over the mode area, replacing the initial Stokes intensity with the initial Stokes power. The total Stokes power P_s can then be approximated by introducing a parameter k that takes into account that the Stokes pulse has an average intensity below $I_{s,max}$:

$$P_s = P_0 \cdot k \cdot \exp\left(a \cdot \tau \cdot \tanh\frac{b}{\tau}\right) \tag{3.4}$$

Here, P_0 is the initial total Stokes power. In the limit case of no walk-off, meaning $D \cdot \Delta\lambda_{PS} \to 0$, the hyperbolic tangent can be approximated by a linear function, leading to the common formula for the Stokes power, Equation 2.14. Equation 3.4 was used to calculate the Stokes power for single pulses of different duration τ propagating through 10 m of fiber. The fiber parameters can be found in Table 3.1. The central wavelength was 1060 nm and the pulse peak power was $P_P = 5\,\text{kW}$.

This problem was also calculated numerically by solving the NLSE with the help of a commercial software (fiberdesk, 2021), that implements a split-step Fourier method. In the numerical model the power in the spectral region of the first Stokes between 1099 nm and 1124 nm was integrated after propagation

Table 3.1: Parameters used for the analytical model

Parameter	Value
Fiber length	4 m, 6 m, 8 m, 10 m
Fiber dispersion	$D = -27.5$ ps/nm/km @ 1060 nm
A_{eff}	227 μm^2
$\Delta\lambda_{PS}$	51.5 nm
g_R	$0.8 \cdot 10^{-13}$ m/W

to obtain the Stokes power P_S. This spectral region corresponds to a Stokes shift between 10 THz and 16 THz, so it covers the first peak of the Raman gain curve, shown previously in Figure 2.3. These boundaries are somewhat arbitrary, and others could be chosen, as long as they are broad enough to include most of the Raman scattered signal. Additionally, it is necessary to consider that a broader spectral range is more robust against noise. The noise (also visible in the spectrum shown in Figure 2.5) stems from two effects: there is the numerical noise (which is negligible) and there is the initial quantum noise, which has to be especially considered.

In the simulation tool quantum noise is modeled by adding one photon of random phase to each numerical bin. This method is widely used since the early days of optical fiber technology (R. G. Smith, 1972). It takes into account, that stimulated Raman scattering is not the only Raman process happening along the fiber, but that there is also spontaneous Raman scattering. However, the net result of the amplification of all this spontaneous Raman scattering along the fiber is equivalent to the injection of a single (fictional) photon at the fiber input (R. G. Smith, 1972). It has to be mentioned that, in the derivation of this result, the approximation of a long enough fiber (compared to the Raman pump absorption) is used. Hereby it can be demonstrated that this quantum noise model is not valid and over-estimates the Stokes content in the first part of the fiber. However, for the cases studied within this thesis, this approximation is fulfilled.

The initial noise disturbs the calculation of the Stokes content: While the spectral integration takes every Stokes photon into account, only those that have a temporal overlap with the initial Raman pump pulse act as seed for the SRS process. If T is the total time window length, only a fraction of τ/T

Stokes photons act as the Stokes seed. Therefore, the Stokes power calculation Equation 3.4 becomes:

$$P_S = P_0 \frac{\tau}{T} \cdot k \cdot \exp\left(a \cdot \tau \cdot \tanh \frac{b}{\tau}\right) + P_0 \cdot (1 - \frac{\tau}{T}) \tag{3.5}$$

The added term proportional to P_0 takes into account that in the numerical model, all noise Stokes photons will be accounted for in the spectral integration, for example even in the case without any fiber propagation in which no SRS occurred.

To compare the numerical simulations and the analytical formula, the Stokes power was calculated with both methods for different fiber lengths at a Raman pump peak power of $P_P = 5\,\mathrm{kW}$. The fixed peak power (incorporated in parameter a of Equation 3.5) leads to different average powers, if the pulse duration is varied. Therefore, the resulting Stokes power increases linearly with pulse duration in the cw limit case of very long pulses where walk-off does not play a role. Which pulse durations belong to this limit case is discussed in more detail in subsection 3.2.1. The pump power and fiber lengths were chosen in such a way, that no pump depletion was observed in the numerical simulation, i.e. the Stokes power stayed below 1 % of the pump power.

The resulting Stokes Power as a function of the pulse duration is shown in Figure 3.1 alongside the results of Equation 3.5.

The numerical simulations are in agreement with the analytical formula. The fitting parameter was found to be $k = 0.016$ for 10 m propagation length. The agreement indicates that the walk-off between the Raman pump and the Stokes signal plays an important role in determining the SRS content at the fiber output. This is because the Stokes light travels faster along the fiber than the pump light, which means that for short pump pulse durations, it will quickly walk-off the pump pulse. Therefore, the pump pulse does not serve as seed for further SRS. This result is analogous to using gratings that filter out the Stokes signal along the amplification fiber, since a lower Stokes seed signal leads to a nonlinear decrease of the Stokes output signal. Thus, the SRS content is strongly dependent on the pump pulse duration and can vary by several orders of magnitude. While this holds true for single pulse propagation, it is also applicable to the cw case, as demonstrated in the following.

The propagation of a cw-field through a passive fiber was simulated with

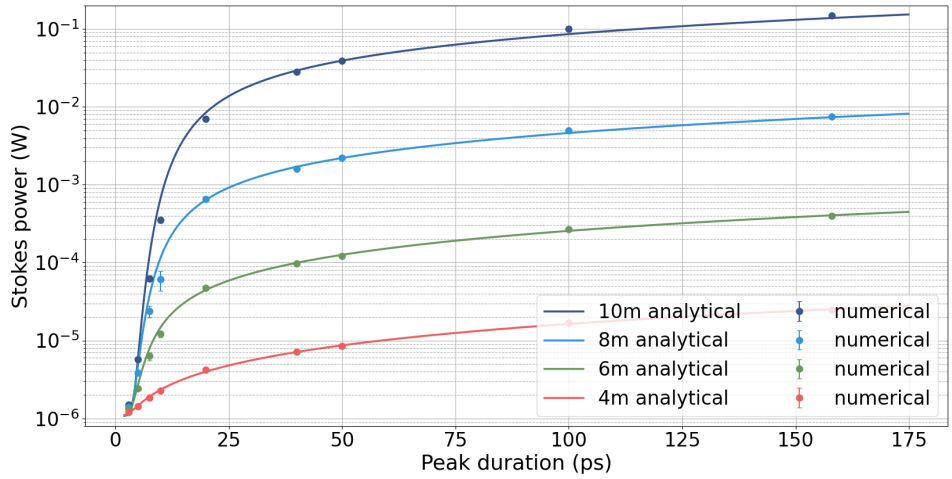

Figure 3.1: The Stokes power P_S is shown over the pulse duration (FWHM) of transform limited Raman pump pulses with a center wavelength of 1060 nm and a peak power of 5 kW, after propagation through a fiber with parameters as listed in Table 3.1.

the parameters of Table Table 3.2.

The pump field consisted of an average power of $P_{avg} = 2.0\,\text{kW}$ with a gaussian spectrum centered at 1060 nm. Its phase was defined using a phase diffusion model following (Frosz, 2010). The phase Φ at each time t is given by:

$$\Phi(t) = \int_{\infty}^{t} \nu_R(x)\,dx \tag{3.6}$$

where ν_R is Gaussian white noise. The variance of this white noise is related to the spectral linewidth of the field. This phase diffusion model (which is a random-walk model) results in fields with distinct temporal features, which is a good approximation to multi-longitudinal mode sources. The influence of different models will be discussed later in subsection 3.2.2. Figure 3.2 (a,b) shows exemplary excerpts of those temporal fields for two different bandwidths of the pump field. While they have the same average power, the spectrally narrower one has clearly longer temporal features.

Such fields are then propagated along a passive fiber with the parameters given in Table 3.2. The corresponding spectra after propagation are shown in Figure 3.2 (c,d). These spectra contain two main differences. First, the one corresponding to the short temporal features exhibits significantly more spectral broadening due to self-phase modulation, as expected (Turitsyn et al.,

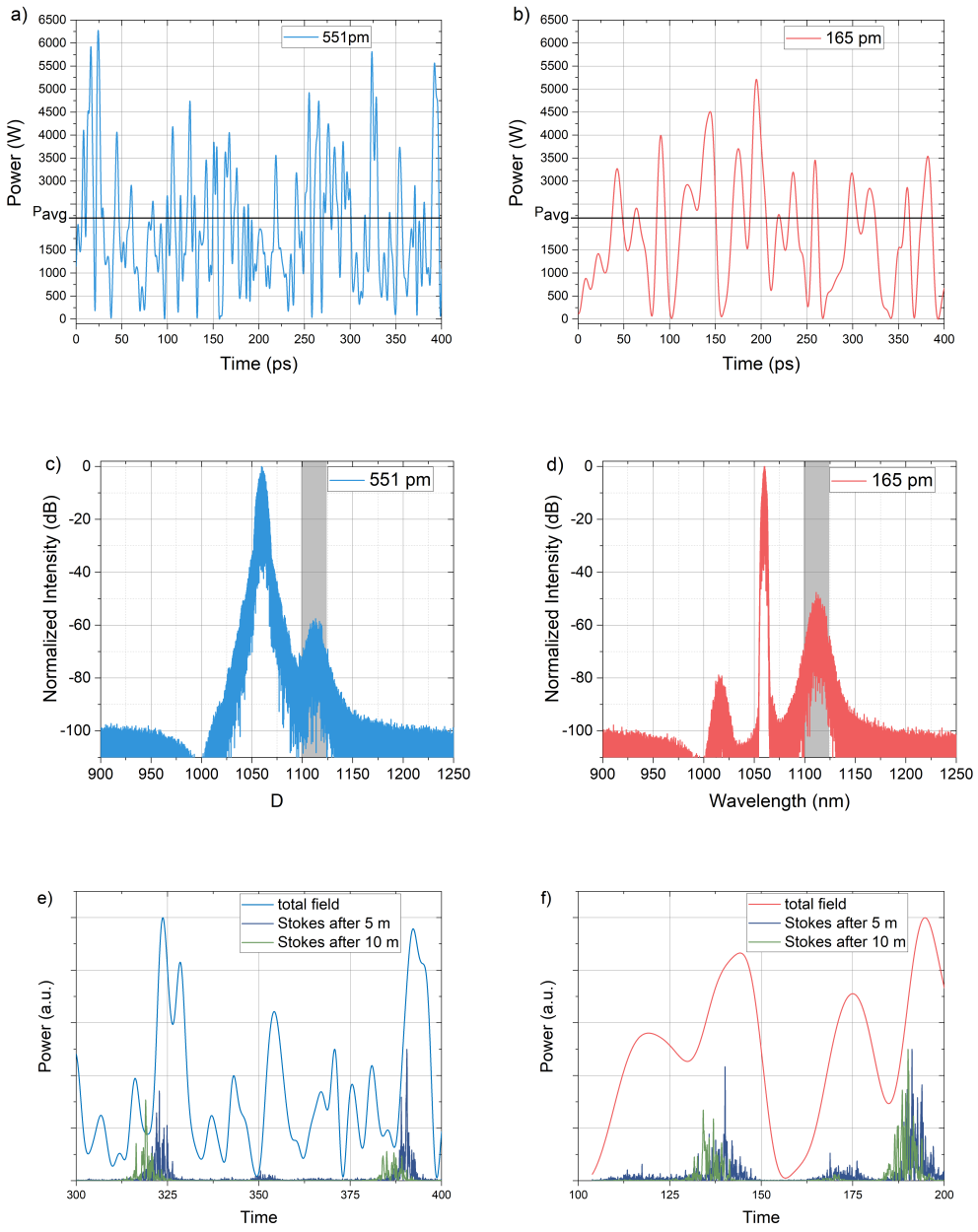

Figure 3.2: Two exemplary sections of temporal Raman pump field distributions before propagation with spectral width of a) 551 pm and b) 165 pm and the corresponding spectra after propagation (c,d). The field with shorter peaks (i.e. the one with the broader bandwith) leads to significantly more self-phase modulation and lower SRS, which also results in a lower four-wave mixing (anti-Stokes) spectral feature. The gray area marks the region from which the SRS content is calculated. Excerpts of the fields (a,b) are shown in (e,f) together with the temporal Stokes signal fields after 5 m and 10 m of propagation. It has to be noted, that the Stokes signal fields are not plotted to the scale of the pump fields, as the Stokes content is much lower (no pump depletion). Walk-off causes the Stokes to leave the Raman pump peak, which occurs earlier for the spectrally broader case.

Table 3.2: Parameters used for the numerical model

Parameter	Value
Center wavelength	1060.0 nm
$\lambda_{min}, \lambda_{max}$	897.5 nm, 1294.3 nm
Time window length	1280 ps (2^{17} points)
g_R^{max}	simple Lorentz model (Blow et al., 1989) $\tau_1 = 12.2$ fs , $\tau_2 = 32.0$ fs corresponding to $0.8 \cdot 10^{-13}$ m/W
f_R	0.18
Quantum noise	1 photon with random phase per bin
Fiber parameters	equal to the analytical model, see Table 3.1

2011). Second, it contains a significantly lower SRS content. This is due to walk-off, which becomes clear from Figure 3.2 (e,f) that shows details of the temporal fields at the fiber input (a,b) together with the Stokes signal after 5 m and 10 m of propagation. It can be seen that the Stokes signal is on the leading (left) edge of the pump peaks and leaves the Raman pump peaks with further propagation. In the spectrally narrow case, this is less pronounced, since the temporal peaks are longer. Here, after 10 m propagation, the Stokes signal is on the leading edge of the Raman pump. In the spectrally broad case on the other hand, it has completely walked-off the Raman pump pulse after 10 m of propagation. It has to be noted that the peak position in the total temporal field does not change with propagation as the time frame is moving with the group velocity of the central wavelength.

To quantify the effect of walk-off, the Stokes power P_S is calculated numerically as the fraction of power in the spectral region of the first Stokes as explained above. The results are shown as dots in Figure 3.3.

In order to apply the analytical equation of the single pulse propagation to the cw case, the rigorous way would be to calculate the Stokes power for every pulse i in the cw-field with equation (3.5) and then perform the sum:

$$P_{S,tot} = \sum_i P_{S,i} \tag{3.7}$$

However, this would require to identify and separate all different pulses in

the cw-field, which would be impractical. Instead, a characteristic peak power and duration is chosen for each field. The statistics of the temporal field is left unchanged for now, but it will be manipulated in subsection 3.2.2. Here, the characteristic peak duration τ_{char} is connected to the spectral width $\Delta\lambda$, that describes the different temporal fields. This is done with a parameter k', according to:

$$\Delta\lambda = k' / \tau_{char} \, . \tag{3.8}$$

This parameter follows from the phase diffusion model Equation 3.6 and, in this case, $k' = 1655\ \text{ps} \cdot \text{pm}$. The characteristic power P_{char} is the average power of a pulse in the cw-field P_{avg}, to be consistent with the the conventional model Equation 2.14, in the limit case without walk-off (e.g. for short fiber lengths). To describe the cw case, Equation 3.4 then becomes:

$$P_S = f_p \cdot \exp\left(\frac{2\, g_R\, P_{char}\, k' \cdot \left(\tanh \frac{D\, \Delta\lambda_{PS}\, z}{2\, k'} \cdot \Delta\lambda \right)}{A_{\text{eff}}\, D\, \Delta\lambda_{PS} \cdot \Delta\lambda} \right) \tag{3.9}$$

with a free parameter f_p that can be fitted by a first experiment or simulation of the laser setup of interest at any given spectral width. Here, 15 numerical points have been used to fit the parameter f_p of the analytical model, independently for each fiber lengths.

With this, one can calculate the Stokes power as a function of the spectral width, which is shown in Figure 3.3 in comparison to the numerical values for different fiber lengths. While the analytical formula and the numerical values describe the same general behavior, there are some discrepancies, especially for broad spectra and long fiber lengths, which will be discussed in subsection 3.2.1. For shorter fiber lengths, less power is transferred from the Raman pump to Stokes. Furthermore, the effect of walk-off is smaller for shorter fiber lengths, as expected. After 10 m fiber length, both approaches describe a reduction of the Stokes power by several orders of magnitude for broader spectral widths.

It becomes clear that walk-off between the Raman pump and the Stokes signal is of crucial importance for the amount of Stokes signal created in a high-power continuous wave Yb-doped fiber laser.

This model was compared with the data presented in the previously mentioned experiment by (Schreiber et al., 2014). The experimental parameters and

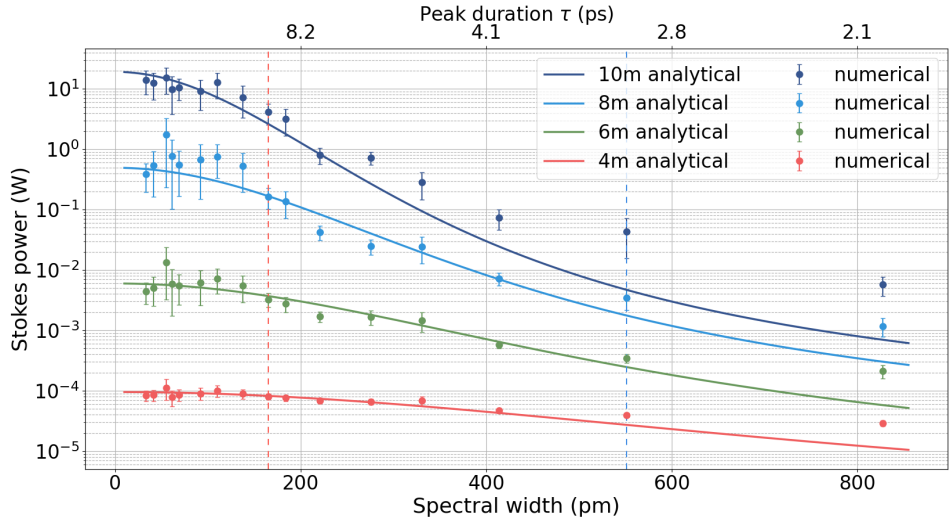

Figure 3.3: The mean Stokes power after propagation over the spectral width (FWHM) in the cw case for both the analytical and numerical models. For the propagation, the parameters of Table 3.1 (analytical) and Table 3.2 (numerical) have been used. For each numerical point, at least 20 field initializations have been performed, which mean value is plotted. The error bars are the standard deviation of the mean values.

analytical parameters can be found in Table 3.3.

It has to be noted, that the experiment compares different high-power fiber oscillators, which does not precisely match the theoretical model, as the average power is not uniform but increasing along the fiber. The parameters of Table 3.3 are used to calculate the Stokes content with the enhanced walk-off model following Equation 3.9. Since the enhanced walk-off model has one free parameter f_p, this parameter was fitted to $\approx 5 \cdot 10^{-7} \cdot P_{avg}$ to best match the experimental data.

The resulting Stokes content in comparison to the experimental data is depicted in Figure 3.4. There, the conventional model following Equation 2.14 is also drawn with a Stokes content matching to the enhanced walk-off model for narrow spectral width.

The conventional model does not incorporate a dependency of the Stokes content on the spectral width and therefore fails to describe the experimental situation. The enhanced walk-off model fits significantly better. There is still some discrepancy between this model and the experimental data, possibly due to the longitudinal power increase in the experiment. Furthermore, the analytical model neglects experimental details like slightly different output powers

Table 3.3: Parameters of the experimental source (Schreiber et al., 2014) and the analytical model.

Parameter	Value
Fiber length	20 m
Fiber dispersion	$D = -27.5$ ps/nm/km
Mode area A_{eff}	227 µm^2
$\Delta\lambda_{PS}$	51.5 nm
g_R	$0.8 \cdot 10^{-13}$ m/W
Average power P_{avg}	760 W
k'	1655 ps · pm

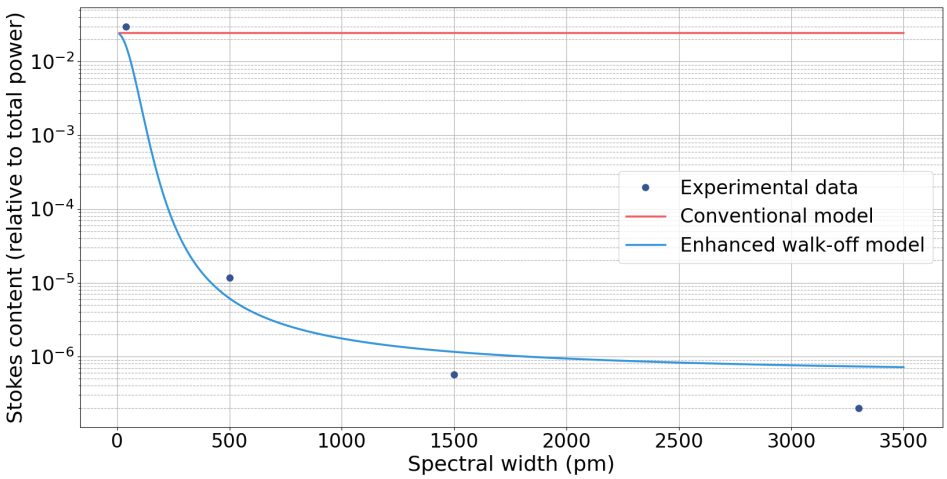

Figure 3.4: The Stokes content over the spectral width (FWHM) for the experimental data of (Schreiber et al., 2014) in comparison to the calculated Stokes content form the conventional model and the enhanced model developed in this thesis.

(and effective lengths) of oscillators with different spectral grating width and differences in reflectivity. However, it becomes clear that accounting for walk-off with the analytical model developed here is a substantial improvement and largely explains the experimental observation. This underlines the importance of walk-off between the Raman pump and the Stokes signal in high-power continuous wave Yb-doped fiber lasers.

3.2.1 Application domain of the analytical model

As the derivation of Equation 3.1 presented in (Christodoulides et al., 1989) requires a case without pump depletion this model is restricted to low Stokes contents. As Stokes contents of 1 % of the total output power are already troublesome for many applications, this assumption is often fulfilled. Therefore, the above described model is applicable in the case where a low SRS content is intended and SRS is the main factor limiting a further power scaling of the Raman pump signal. Crucially, this includes high-power fiber oscillators, as mentioned above. MOPA systems comprising a fiber oscillator as seed source followed by several meters of active fiber are also prone to the walk-off effect. In both cases, the typical active fiber length is in the order of $\mathcal{O}(10\,\mathrm{m})$ and the transport fiber length in the order of a few meters (oscillators: (Möller et al., 2019; Yang et al., 2018a; Yang et al., 2018b), MOPA setups: (Hejaz et al., 2017; Fang et al., 2017; T. Li et al., 2018)). As mentioned above, in these systems the walk-off effect is relevant and the above described analytical model is applicable. However, this is not the case for very long fibers. In order to understand this, it is worth examining the two limit cases of a very short and very long fiber. In a very short fiber no walk-off takes place. In a very long fiber on the other hand, the walk-off is so large that it will cover several temporal features. A suited parameter to describe the application regime of the model is the walk-off time t_w. It is calculated by the fiber length L, the dispersion D and the wavelength separation of Raman pump and Stokes $\Delta\lambda_{PS}$:

$$t_w = L \cdot D \cdot \Delta\lambda_{PS} \tag{3.10}$$

This time should be smaller than the average separation time between two Raman pump peaks t_{sep} to prevent that the Stokes signal generated by a first Raman pump peak seeds a subsequent Raman pump peak. This time separation is inversely proportional to the spectral width: $t_{sep} \propto \frac{1}{\Delta\lambda}$. The temporal

fields of Figure 3.2 illustrate that as well.

For fused silica, the dispersion at a wavelength of approximately 1 µm is about $D = -27.5 \frac{\text{ps}}{\text{nm}\cdot\text{km}}$. For a propagation of 5 m, this leads to $t_w \approx 7.6\,\text{ps}$. The temporal fields depicted in Figure 3.2 (e,f) show the Raman pump peak separations and the walked-off Stokes signal. After 5 m of propagation, the Stokes peak has not yet reached a second Raman pump peak. The relation between walk-off time and pulse separation time explains why the analytical model is less accurate for long fiber lengths and broad spectra: These conditions enable reaching a second pump peak.

If, on the other hand, t_w is much shorter than the characteristic peak duration τ_{avg}, walk-off will only have a minor effect. This is the case for a very short fiber. This can be seen in the saturation of the Raman content in Figure 3.1 for long peak durations. There, the Stokes content approaches the single-longitudinal mode cw limit of Equation 2.14.

Another limit of the model is that it does not easily allow comparing laser sources with different temporal field characteristics, which will be discussed in the following.

3.2.2 Temporal field characteristics of cw lasers

In the derivation of Equation 3.9 the description of the temporal field statistics was reduced to a single parameter, the average pulse duration τ_{avg}. In reality, the probability distribution of pulse durations and peak powers can be quite complex. The simplification is only justified if the field statistics is left unchanged. While this is true for the oscillator model where the phase varies following a random walk (as described in (Frosz, 2010) as phase diffusion model), Equation 3.9 does not correctly describe, for instance, a field with a uniformly distributed random phase with unchanged fitting parameters.

This becomes clear when comparing two temporal field statistics: one with the phase diffusion and one with the uniformly distributed random phase. Temporal fields were created for both models with the same characteristic peak duration. The fields were searched for peaks, and a pulse duration and pulse energy was attributed to each peak. This peak-finding is a non-trivial task and there are several ways to accomplish this goal. Here, a simple method was used that defined a pulse as the region in a temporal field between two neighboring minimums of its amplitude. The second moment (the variance)

of this pulse was calculated and the pulse length was chosen to be twice that variance (which is, depending on the pulse form, not necessarily the same as the full width at half maximum). The pulse energy was then defined as the sum of the energy within this pulse length around the pulse center.

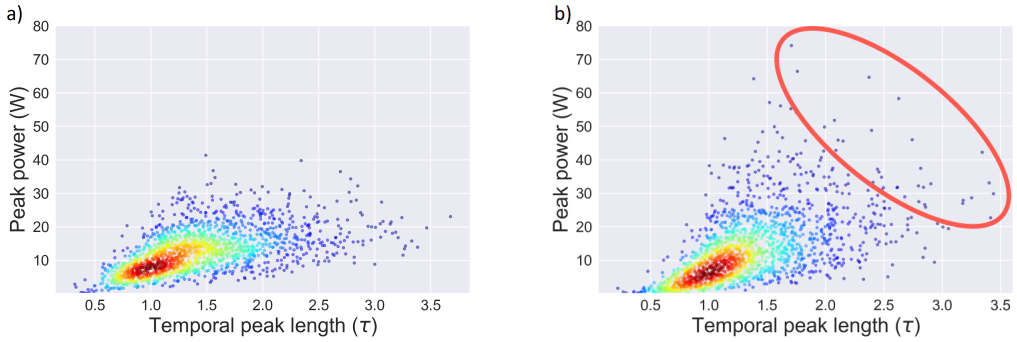

Figure 3.5: Pulse parameter distribution in the temporal field created with a phase diffusion model (a) and a random phase (b), showing significantly more peaks with high peak power and long peak duration in the random phase model (highlighted by the red ellipse).

Figure 3.5 shows the result of this pulse decomposition analysis for the phase diffusion model and for the random phase model. The random phase variation allows for a significantly higher fraction of peaks with long duration and high energy. Since walk-off has a lower effect for those peaks, the SRS content will be significantly higher for this model and Equation 3.9 needs to be adapted accordingly by its fitting parameters. Thus, the temporal field statistics is of high importance for the Stokes power due to the effect of walk-off. Different temporal field characteristics explain not only the variation of the Stokes power with the oscillator spectral width, but also other SRS suppression techniques, such as the introduction of transmission fibers to the seed lasers, as shown in (T. Li et al., 2019). There, the characteristic peak durations are $t_{avg} = 100\ ps > t_w$ and thus walk-off does not play a dominant role, as it has been pointed out. Instead, the second characteristic property of the peaks becomes important: the peak power. (T. Li et al., 2019) showed a simulation in which a reduction of the peak power was reached by dispersion caused within an additional 500 m of transmission fiber introduced into the seed laser. As $t_{avg} > t_w$, the corresponding increase of pulse duration does not lead to a stronger Raman scattering. However, this technique of SRS reduction only works for systems where a broad signal linewidth can be tolerated. For narrow-linewidth

signals $t_{avg} < t_w$, the walk-off effect becomes dominant again.

3.3 Conclusion

In this chapter it was shown that walk-off between the Raman pump and the Stokes signal is of crucial importance for the amount of Stokes signal present at the fiber output. An existing walk-off model describing the pulsed case could be expanded to describe the cw case and explain the influence of the spectral width of a fiber laser on the Raman content.

These investigations directly lead to guidelines for the construction of high-power fiber laser systems with low Raman scattering.

For high-power fiber laser systems where a low Raman content is desirable, the spectral width should be carefully considered. This is especially helpful since other parameters that reduce nonlinearities, such as fiber length and core size, are often set. A short calculation of the walk-off time with Equation 3.10 enables the identification of whether walk-off is important in the system of interest or not. In the case where walk-off is important, this thesis provides, with Equation 3.9, a simple, analytical formula that allows calculating the Raman content for different spectral widths, with only one free parameter (that can be estimated by an initial experiment or simulation). This formula shows that the Stokes power strongly decreases over several orders of magnitude with an increasing spectral width. For even broader spectral widths, this dependency is much weaker. These results are especially interesting for high-power fiber oscillators that are currently limited by SRS, especially, since the spectral width of the emission of these systems can be controlled with the output coupler. With the easing of SRS as limitation, the output power of these oscillators can be expected to rise in the near future, up until TMI become the limiting factor. The onset of this limit is currently unclear as TMI in high-power fiber oscillators has been covered by just a few publications (Möller et al., 2018; Scarnera et al., 2019). Very recently an output power of 6 kW was demonstrated (Ye et al., 2021) without any sign of TMI in a fiber with a larger core size, compared to the 20/400 µm fiber used by (Möller et al., 2018) to extract an output power of 5 kW. Consequently a stable operation at an output power of 6 kW with a 20/400 µm fiber seems within reach.

4 Nonlinear limitation of narrow-band cw Raman amplification

As explained in section 2.4, Raman fiber amplifiers are used to access wavelengths otherwise unreachable by rare-earth doped fiber laser systems. However, it has to be taken into account, that for many applications, the linewidth of the laser is of importance, for example to reach high output powers in the visible spectrum range via second harmonic generation of RFA (Runcorn et al., 2015). Here, the efficiency of the second harmonic generation decreases with broader linewidths of the pump RFA (Surin et al., 2016). Consequently, a narrow linewidth of the Stokes signal is desirable.

To investigate these RFA, an experimental setup of a narrow-band Raman fiber amplifier was built. This setup is described in the following section 4.1. An important aspect of this setup is the preservation of a narrow spectral width. The spectral properties of the Stokes signal are investigated in section 4.2. Finally, a conclusion is drawn in section 4.3. The knowledge gained here also serves as a basis for a high-power RFA and the examination of the interplay between thermal effects and Raman amplification presented in chapter 5.

4.1 Experimental setup

The setup comprised three main structural elements: a Raman pump seed laser, a Stokes seed laser and a high-power amplification system which amplifies the Raman pump to kW-level output powers. Please note that throughout this thesis, *Raman pump* refers to the signal acting as pump in the Raman process, usually at a wavelength near 1060 nm. Light at a wavelength of approximately 976 nm, used for energizing the amplification process inside the YDF,

is specifically denoted by its wavelength to avoid confusion. The schematic of the system is shown in Figure 4.1. Each of the structural elements itself consisted of several components which are detailed hereafter. Subsequently their combined performance is described.

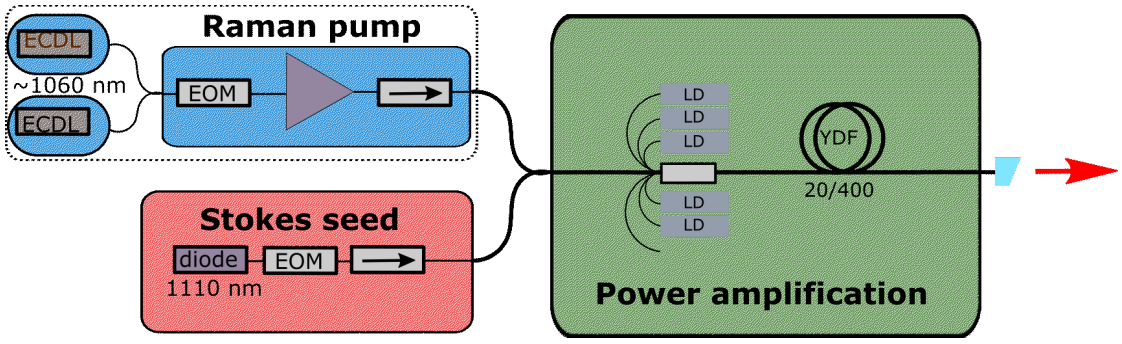

Figure 4.1: The simplified experimental laser setup, see text for detailed discription.

Raman pump laser

The Raman pump system consisted of two different external cavity diode lasers ECDL delivering approximately 10 mW of linear polarized light each. The wavelength of these two lasers was located around 1060 nm, but they had a slight, controllable separation. This arrangement is used to achieve significant spectral broadening during propagation via SPM (Plötner et al., 2017). This spectral broadening is necessary to avoid SBS along the fiber. A subsequent electro-optic phase modulator had the same purpose of mitigating SBS (Harish et al., 2018). This modulator was driven by a signal that was a combination of white noise and a sinusodial wave. This phase modulation technique enabled output powers of an YDF of up to 4.3 kW without limiting SBS (Beier et al., 2017a).

The signal was then amplified to an output power of about 3 W in a 10/125 µm Yb-doped fiber, that was cladding-pumped by a single 976 nm laser diode coupled via a pump combiner. The length of the active fiber was 2.8 m, which corresponds to a total cladding absorption of approximately 14 dB at a wavelength of 976 nm. The signal emitted from this first amplification stage then went through a set of fiber-coupled optical isolators to avoid any back-reflection from the high-power amplification element that might disturb the Raman pump seed laser. A fiber-coupled spectral filter, which removes

amplified spontaneous emission signals, was included as well. Hereafter, a 99/1 fiber tap coupler allowed monitoring both the seed laser stability and the backwards travelling light. The latter was characterized with a power meter and a photodiode. Stimulated Brillouin scattering would lead to a strong increase in the backward propagating power as well as to short pulses in the photodiode signal as explained in subsection 2.2.3. Furthermore, TMI also manifests itself on this backward photodiode as a power fluctuation (Möller et al., 2021). This investigation also showed that the power fluctuation in the backward direction is temporally correlated to the power fluctuations measured at the fiber output in the forward direction, most likely caused by back-reflections within the fiber near the fiber output. For all measurements presented within this chapter, no such fluctuations have been detected.

Stokes seed laser

The Stokes seed laser consisted of an external cavity laser diode, delivering about 10 mW of linearly polarized light at a wavelength of 1110 nm. While the simulation shown in Figure 2.5 suggests a peak of the optical Raman gain near 1117 nm, a laser providing this wavelength was unfortunately not available. However, the Raman gain is spectrally broad enough to allow for significant amplification at 1110 nm as well, which also becomes clear in Figure 2.5. As done for the Raman pump seed laser, the signal phase was modulated by an electro-optical phase modulator. A 99/1 fiber tap coupler was used to monitor the power level and stability of the Stokes seed laser. The Stokes seed laser was then combined with the Raman pump seed laser with a wavelength division multiplexer.

Thus, the Raman pump and Stokes signal propagated in the same direction (co-pumping), which enhances nonlinear effects, as explained in subsection 2.2.3. Furthermore, this co-propagation is important for the subsequent high-power amplification as the seed lasers of the Raman pump and the Stokes signal do not have to be protected against kW-level signal powers of the other wavelength, which increases the stability of the system.

High-power amplification element

The combined signals of Raman pump and Stokes seed were then fed into a mode-field adapter that connected the 10/125 µm fiber used so far to the

20/400 µm fibers used from now on. A fused coupler combined the 20/400 µm fiber together with six 200/220 µm multi-mode fibers to a single 20/400 µm fiber. This device was used to couple 976 nm light to excite the Yb-ions in the following active fiber. There were five laser diodes used, each emitting up to 500 W. The active fiber was a double-cladding Yb-doped 20/400 µm fiber. This fiber, with core NA = 0.065, had a peak cladding absorption of approximately $\alpha = 1.9\,\mathrm{dB/m}$ at a wavelength of 976 nm. The active fiber had a length of 10 m and was coiled on a metal, water-cooled spool of 12 cm diameter. This spool was additionally put inside a swirling water basin for further cooling. A 1 m long Germanium-doped 20/400 µm fiber with a water-cooled, angled end cap with anti-reflective coating was spliced to the active fiber at the output end. This fiber piece was loosely coiled.

The beam emitted from the fiber end cap was characterized with an optical spectrum analyzer, photodiodes, a beam quality measurement instrument and power meters. To this end, the spectral regions of Raman pump and Stokes setup were separated from each other by specifically designed dichroic mirrors.

Amplifier performance

The experimental setup, in which the 976 nm-signal co-propagated with the Raman pump and Stokes, allowed for an amplification of the Raman pump seed to the kW-level. The beam quality of the pump was measured to be $M^2 = 1.2$ at the highest output power and no temporal instabilities of the mode profile were observed. The total output power was stable with a standard deviation of $< 1\,\%$. Due to the relatively short fiber length and low Raman pump intensities over a long section of the active fiber, the Stokes seed was not amplified beyond a power of 10 W. This also manifests itself in the power slope of the amplifier, depicted in Figure 4.2 a). Even at high output powers, the Raman conversion remains low and the power slope remains linear.

While the Stokes amplification is not strong enough to reach high output powers and significantly deplete the Raman pump, it is still strong enough for the Stokes signal to be seen as a distinct Stokes peak in the optical spectrum. Exemplary spectra are depicted in Figure 4.2 b), corresponding to an output power of 137 W (red) and 1074 W (blue). Significant spectral broadening of both the Raman pump and Stokes signal is visible. There are two additional spectral features appearing in a symmetrical fashion around the Raman pump

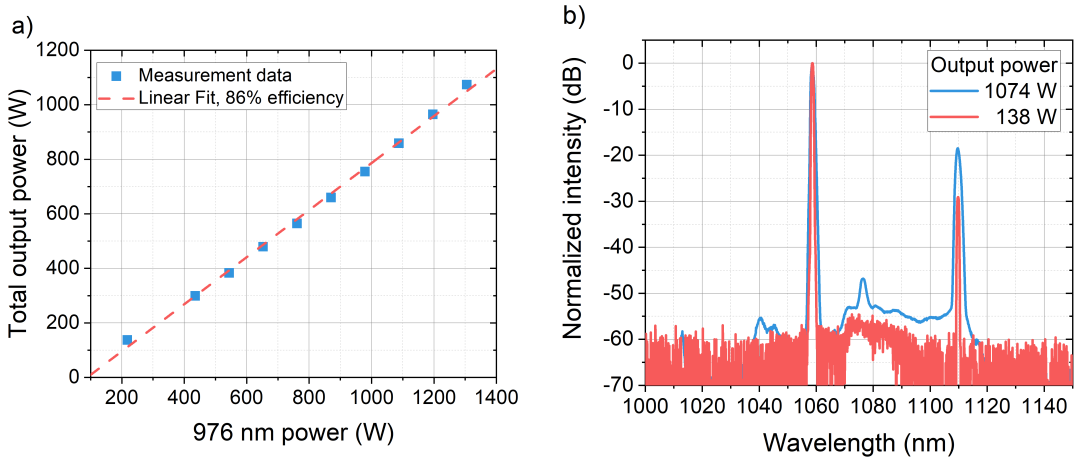

Figure 4.2: Total output power of the experimental setup (a) and optical spectrum at the fiber output at powers of 137 W and 1074 W (b).

signal at a distance of approximately 18 nm. These two signals stem from FWM and are not of special interest at this point, but are discussed further in subsection 5.3.1. Additionally, some light originating from amplified spontaneous emission is visible around 1080 nm. There is no amplified spontaneous emission visible at lower wavelengths due to the spectral filter used in the seed laser, the co-pumping with 976 nm light of the active fiber and the long active fiber length, which favors re-absorption of low wavelength signals.

Spectral measurements of the Raman pump and Stokes signal with high resolution enabled to precisely determine the spectral width of these signals. These spectral investigations are presented in the following.

4.2 Raman pump temporal structure as cause of nonlinear spectral broadening

For many applications it is desirable to have a Stokes signal with a narrow linewidth, as explained above. In contrast to that, a significant broadening of the Stokes signal linewidth was observed in the experiment presented here, which depended on the linewidth of the Raman pump. At approximately 1 kW of output power, the 10 dB linewidth of the Raman pump could be tuned between 500 pm and 3000 pm, by changing the wavelength separation of the two ECDLs. The Stokes signal seed linewidth, determined by a single ECDL, was not changed. Nevertheless, the linewidth of the Stokes signal at the output

was influenced by the Raman pump linewidth, despite the Raman gain being much broader than the width of the Raman pump signal. Figure 4.3 shows the measured linewidth of both signals as a function of the output power. It becomes clear that the broader the Raman pump linewidth, the broader the Stokes signal linewidth.

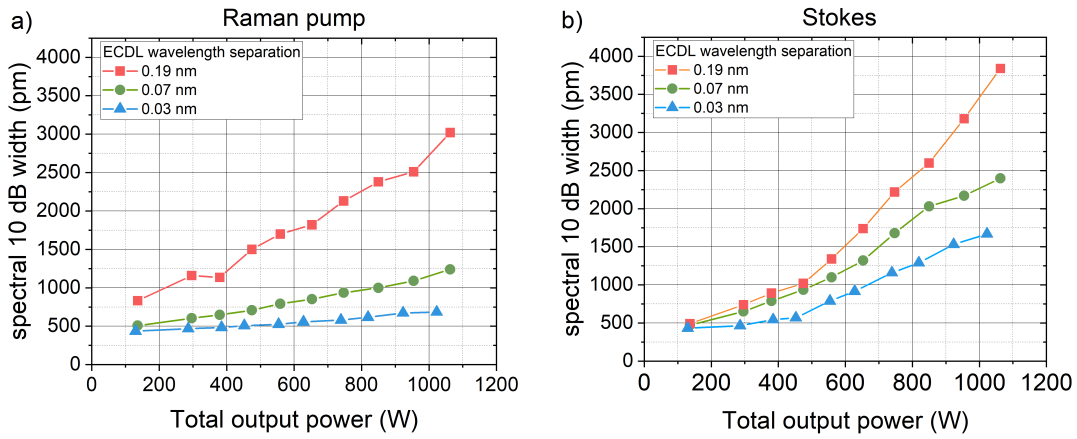

Figure 4.3: The measured 10 dB-linewidth of the Raman pump (a) and the Stokes signal (b) at the output of the system over the output power. Two single-longitudinal mode laser sources were used as the Raman pump seed source, which was then amplified in the YDF.

This behavior can be explained by the effect of Cross-phase modulation (XPM). In the derivation of the NLSE (Equation 2.8) a main field propagates along the fiber. However, there might be two fields instead, for example when two different polarization states propagate in the fiber. While the two fields would not directly interfere, the refractive index changes in the fiber caused by one field would still affect the other. The same is true for two fields at different wavelengths as it is the case with the Raman pump and Stokes signal in this experiment. Therefore, instead of using a single NLSE, a set of two coupled equations is more suitable. Assuming the signals are co-polarized and neglecting SRS and self-steepening, the equations become:

$$\frac{\partial A_P}{\partial z} = -\frac{\alpha_P}{2}A_P - \left(\sum_{n=1}\frac{i^{n-1}\beta_{P,n}}{n!}\frac{\partial^n}{\partial t^n}\right)A_P + i\gamma_P A_P\left(\left|A_P\right|^2 + 2\left|A_S\right|^2\right) \quad (4.1)$$

$$\frac{\partial A_S}{\partial z} = -\frac{\alpha_S}{2}A_S - \Big(\sum_{n=1}\frac{i^{n-1}\beta_{S,n}}{n!}\frac{\partial^n}{\partial t^n}\Big)A_S + i\gamma_S A_S\Big(\big|A_S\big|^2 + 2\big|A_P\big|^2\Big) \quad (4.2)$$

for the Raman pump and Stokes field amplitudes (A_P and A_S, respectively), with $\gamma_{S/P}$ being given by Equation 2.9 (Agrawal, 2013). The nonlinear term proportional to γ now contains an SPM related term as before, but also contains the field amplitude of the co-propagating field at the different wavelength. This is the XPM related term.

In the experiment presented here the Raman pump seed consisted of two single-longitudinal mode lasers, whose wavelengths differed slightly. These two lasers interfered with each other resulting in a beating. Consequently, A_P took a sinusoidal form in time (as well as along the fiber at any specific point in time). A spectral separation in the order of $\mathcal{O}(0.1\,\mathrm{nm})$ corresponds to a beat frequency of $\mathcal{O}(8\,\mathrm{GHz})$. Consequently, there were temporal peaks with pulse durations of $\mathcal{O}(100\,\mathrm{ps})$. Through the SPM related term in Equation 4.1, these temporal peaks undergo SPM as the field propagated along the fiber. Accordingly, the spectrum got broader. This SPM-induced broadening prevents SBS as shown in (Beier et al., 2017a). Moreover, (Plötner et al., 2017) presents some additional numerical simulations about this.

As A_P takes a sinusoidal shape in the time domain, this leads to spectral broadening of the Stokes signal through two processes: First, the temporal shape of A_P leads to a time-dependent variation of the efficiency of the Raman process as it depends on both the Raman pump and Stokes intensity as described by Equation 2.13. This nonlinear gain causes a pulsed shape of A_S, which leads to SPM of the Stokes signal. However, as the Stokes power is low ($< 10\,\mathrm{W}$), the SPM-induced spectral broadening of the Stokes signal should be considerably less than the SPM-induced broadening of the pump that has a kW-level output power. A numerical simulation of a cw Stokes signal with an average power of 10 W and an initial spectral 10-dB linewidth of 345 pm travelling through a 20/400 µm fiber was performed. After a propagation length of 10 m, the increase of the 10-dB linewidth was below 2 %. This means, that SPM-induced spectral broadening of the Stokes signal does not play an important role in the above presented experiment. The second effect responsible for Stokes broadening is the nonlinear term related to XPM in

Equation 4.2. Through this XPM-term, the refractive index modulation caused by the temporally sinusoidal Raman pump leads to a spectral broadening of the Stokes signal. This explains why, in the above presented experiment, the Stokes linewidth increased with the Raman pump linewidth, despite the fact that only one narrow-band Stokes seed was used.

As the wavelength separation of the two Raman pump seed lasers was increased, the beating of A_P got faster and the SPM-induced broadening of the Raman pump got stronger and so did the XPM-induced broadening of the Stokes signal. This is clearly visible in Figure 4.3. The strength of XPM-induced broadening and SPM-induced broadening depends on the Stokes and Raman pump intensities. For a higher Raman pump intensity than Stokes intensity (as it is the case here), the XPM-induced broadening of the Stokes in Equation 4.2 is more important than the SPM-induced broadening of the Raman pump. The measured linewidths depicted in Figure 4.3 are in accordance with that, as they show a significantly broader Stokes than Raman pump linewidth. It has to be noted, that for higher Stokes powers, the Raman pump will not only experience SPM-induced broadening but also XPM-induced broadening and the linewidth difference will not be as pronounced.

To test this behavior, the power ratio of the two Raman pump seed lasers was varied, while the wavelength separation was kept constant. This does not change the frequency of their beating but its modulation amplitude. According to the reasoning above, lower modulation amplitudes correspond to lower spectral broadening. Table 4.1 exhibits the measured Stokes 10 dB-linewidth at an output power of approximately 600 W, that shows the predicted behavior.

Table 4.1: The measured 10 dB-linewidth of the Stokes signal at an output power of approximately 600 W for different Raman pump wavelength separations.

Raman pump seed power ratio	1 : 1	1 : 2	1 : 3
Stokes 10 dB-linewidth (pm)	1740	1380	1270

To prevent the XPM-induced spectral broadening of the Stokes signal, the sinusoidal shape of A_P must be avoided. This can be achieved in several ways: First it would be possible to choose an orthogonal polarization between the two Raman pump lasers, which would prevent their beating. However, this would forbid the use of any polarizing elements, including polarizing optical

isolators. As these isolators are crucial to ensure the stability of the seed laser, this solution is impractical. Another possibility is to abandon the use of two different single-longitudinal mode seed lasers for the Raman pump. In fact, a multi-longitudinal mode seed laser can be used instead, if it is spectrally broad enough to prevent SBS in the Raman pump.

This approach was tested by deploying a laser diode, wavelength-stabilized with a Fiber Bragg grating (FBG), emitting polarized light at a center wavelength of 1060 nm. This Raman pump seed laser was phase modulated by an electro-optical modulator. The strength of this modulation allowed varying the spectral width of the Raman pump seed. Three different initial Raman pump linewidths were tested (10 dB-linewidth of 468 pm, 372 pm and 296 pm). The Stokes seed linewidth was kept constant. The resulting linewidths of the Raman pump and Stokes signal after high-power amplification are depicted in Figure 4.4.

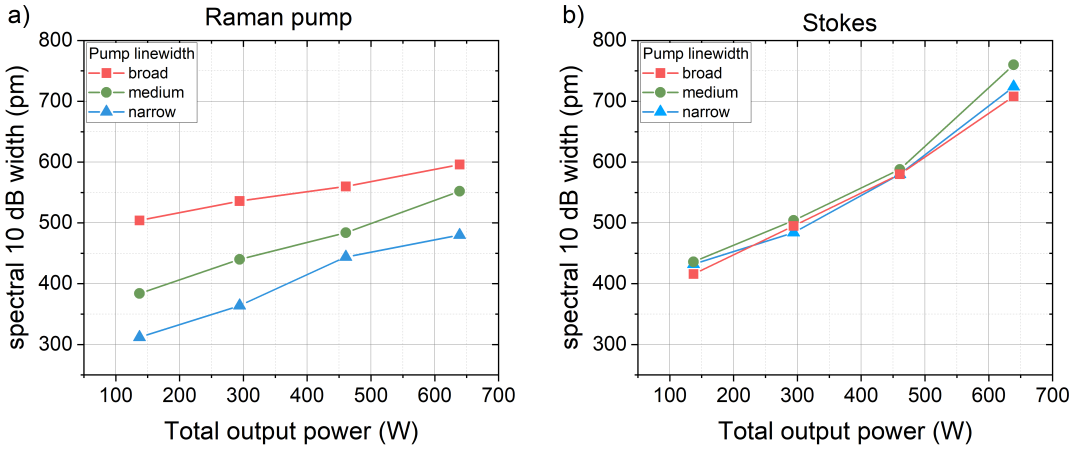

Figure 4.4: The measured 10 dB-linewidth of the Raman pump (a) and Stokes signal (b) at the output of the system over the output power. A multi-longitudinal source was used as the Raman pump seed source, which was then amplified in the YDF.

While the linewidth of the Raman pump was significantly different, the Stokes linewidth remained unchanged. There was no XPM-induced spectral broadening of the Stokes signal observed. Thus, the multi-longitudinal mode Raman pump seed source enables narrow-band Raman amplification. For high-power RFA, co-pumped by high-power fiber lasers, it is therefore necessary to adapt the Raman pump seed source. Instead of the commonly used combination of two single-longitudinal mode laser diodes, a multi-longitudinal mode source should be used to avoid XPM-induced spectral broadening of the

Stokes signal. These insights are used for all experimental setups in chapter 5, where the output power of an RFA is further increased.

4.3 Conclusion

In this chapter, optical effects influencing SRS in high-power fiber laser systems have been investigated. The spectral broadening of the Stokes signal in a Raman fiber amplifier could be explained by XPM. These investigations directly lead to guidelines for the construction of high-power RFAs.

In such systems it is necessary to avoid cross-phase modulation between the Raman pump and Stokes signal. Since a co-propagation of Raman pump and Stokes signal is beneficial for the system stability, XPM cannot be avoided completely. Furthermore, the nonlinear parameter γ will -in most fibers- be very similar for the Raman pump and the Stokes signal (and it has to be large for a high Raman conversion efficiency). Instead, using a spectrally broad Raman pump source ensures low nonlinear effects of the Raman pump source and, consequently, low XPM. This was experimentally verified in this chapter. However, high-power RFAs, are furthermore limited by Raman-induced TMI, which will be discussed in the next chapter.

5 Observation and characterization of TMI in RFA

High-power, few-mode laser systems are inherently prone to thermal effects due to the large amount of converted energy, as described in section 2.3. Since SRS causes a heat load in the fiber core, it impacts these thermal effects.

The heat load caused by SRS creates a thermal lens in the fiber, analog to the thermal lens caused by rare-earth amplification explained in section 2.3. Since this thermal lens is dependent on the converted power, the mode-field diameter changes with the output power of the laser system which is undesirable. However, in fiber lasers with good beam quality ($M^2 < 1.5$) thermal lensing is usually not as critical as the effect of TMI, which is currently limiting their performance (Zervas, 2019).

From section 2.3, it is known that a heat load in a fiber core, which is radially non-symmetric can result in TMI. This radially non-symmetric heat load can originate from a beam that incorporates some HOM content. In the fiber, the Raman pump as well as the Stokes beam can -in principle- have such a HOM content and, thus, an impact of SRS on TMI is reasonable. Indeed, SRS influences TMI and vice versa. It is important to note that small amounts of Stokes light can be tolerated in many systems, but an unstable output beam can not. Consequently, TMI has to be avoided and the impact of SRS on TMI is crucial, while the impact of TMI on SRS is of minor importance.

This chapter investigates the impact of Raman amplification on TMI. First, section 5.1 describes the state of the art prior to this work about the influence of SRS on the beam quality of active fibers. Thereafter, the experimental setup and methods used to investigate TMI are discussed in section 5.2. Section 5.3 then presents new experimental evidence of SRS-induced TMI in passive fibers. The influence of several key laser parameters (especially Stokes seed power

and fiber length) are investigated there as well. The insights and experimental results of SRS-induced TMI in active and passive fibers are then discussed in section 5.4. There, the influence of other laser parameters will be considered and mitigation strategies of SRS-induced TMI will be discussed. Finally a conclusion is drawn in section 5.5.

5.1 Recent research on SRS-induced TMI in active fibers

As described in section 2.3, the effect of transverse mode instability is caused by the interaction of three components: a mode beating pattern, a refractive index grating and a phase shift between the two. In active fiber lasers, SRS acts on all three elements, as explained in the following.

Through the additional quantum defect of the Raman process, additional heat is introduced into the fiber. Via the thermo-optic coefficient ($\frac{\mathrm{d}n}{\mathrm{d}T}$), this leads to a refractive index increase at the location where the scattered Raman phonon dissipates into heat. As described in subsection 2.2.2, this region is approximately identical to the region where the Raman pump photon is absorbed. For core- and cladding-pumped RFA, this is the region within the fiber core where the mode pattern has an intensity maximum. Therefore, the SRS process heats the same fiber regions as the rare-earth amplification process and, thus, increases the strength of the thermally-induced refractive index grating.

As this temperature change diffuses within the fiber, the overall refractive index profile also changes, which leads to an even stronger increase of the refractive index of the fiber core as opposed to the fiber cladding. This, in turn, favors the HOM guidance, as it increases the core NA, which leads to a higher V-number through Equation 2.6. An increased HOM guidance, in turn, can lead to a higher HOM content along the fiber. If, for example, the mode excitation at the beginning of the fiber creates some HOM content (e.g. through an imperfect fiber splice), light in this HOM usually experiences some bend loss as it propagates along the fiber. However, an increased HOM guidance can compensate this bend loss and, thus, increase the HOM content in the rear parts of the fiber.

The higher HOM content results in a more pronounced mode beating pat-

tern.

Finally, the Raman process can be seen as a perturbation to the system with a temporally unstable Stokes signal acting similar to an intensity noise. This could cause a phase shift between the mode pattern and the refractive index grating.

Since SRS acts upon all three components responsible for TMI, it is unsurprising, that it also influences the TMI threshold of rare-earth doped fiber lasers. Recently, it was experimentally shown that SRS can induce TMI in an Yb-doped fiber amplifier (Hejaz et al., 2017). There, a fiber laser operating at 1080 nm showed a decrease of modal purity at approximately 1.3 kW output power, simultaneously with the an appearance of Stokes light at the output and in the backward direction, together with a strong increase of backward propagating power. A reduction of the active and passive fiber length led to a stable operation at 1.6 kW output power. An increase of the seed laser power of the Raman pump from 100 W to 500 W allowed for even higher output powers and a threshold was observed at approximately 1.8 kW output power. At this threshold the same behavior of reduced modal purity and appearance of Stokes light both in the forward and the backward directions was observed. Unfortunately, this work did not show any data acquired with high temporal resolution to resolve the modal instability. However, since the overall backwards power below the threshold was relatively small (less than 1 W), and the forward Stokes content was small as well, the additional heat load through the Raman process was negligible. Therefore, the TMI are here probably caused by the action of SRS on TMI via a perturbation of the phase shift between the RIG and MIP in the fiber.

A similar behavior was observed by (Z. Li et al., 2018), who claimed a TMI threshold at an output power of 1.9 kW with a Raman content of 6.0 %. Unfortunately, the contribution does not present time-resolved measurements indicating TMI, but rather uses “beam profiler measurement results” that are not presented, to calculate a threshold. Additionally, the Stokes content is calculated from a measured spectrum. This is not accurate in the case of TMI due to a fluctuating beam profile, which results in a fluctuating coupling into the spectrum analyzer. However, the theoretical work presented in this contribution predicts a dependence of the TMI threshold on the fiber length, in that a longer fiber length leads to a higher SRS content which decreases the total output power at the TMI threshold.

The concept of SRS-induced mode distortions was studied further theoretically (Liu et al., 2018). The work examines a co-pumped Yb-doped fiber laser operating at 1070 nm that is amplified to about 1.7 kW output power in 20 m active fiber length. As a result, it was shown, that the SRS content increases first and the HOM content increases shortly thereafter. It was concluded that SRS enables a coupling of FM to HOM, which might be responsible for TMI.

The above cited works showed that in active Yb-doped fiber lasers even small SRS contents might disturb the laser process in the active fiber, resulting in TMI. High-power Raman fiber amplifiers do not rely on active fibers so a disturbance of the active fiber laser process is not straightforward, but this thesis shows that there can still be TMI in passive fiber Raman amplifiers. The evidence for this was acquired by a spectrally selective TMI detection method. This method and its experimental realization are explained in the following section.

5.2 Spectrally selective TMI detection

To investigate SRS-induced TMI in passive fibers, a high-power RFA was constructed, based on the work presented in chapter 4. The components and operating principle of this setup are explained in the following subsection 5.2.1. The beam stability of this RFA was then analyzed independently for the Raman pump and the Stokes signal. The methods for this beam characterization and further setup characterization methods are detailed in subsection 5.2.2.

5.2.1 Experimental setup

The experimental setup consisted of four main structural elements: a Raman pump and a Stokes seed laser, a high-power amplification element (which amplified the Raman pump to kW-level output powers) and a Raman enhancement element to achieve a pronounced Raman effect. Please note that throughout this thesis *Raman pump* refers to the signal acting as pump in the Raman process, usually at a wavelength near 1060 nm. Light at a wavelength of approximately 976 nm, used for amplification inside the YDF is specifically denoted by its wavelength. The schematic of the system is shown in Figure 5.1. This setup differs in several key aspects from the one presented in chapter 4, as the insights gained there led to certain modifications. Consequently, each

of the four structural elements is detailed hereafter, followed by a description of their combined performance. Subsequently, the observation of TMI at the fiber output is detailed and evidence for it being caused by Raman scattering is given.

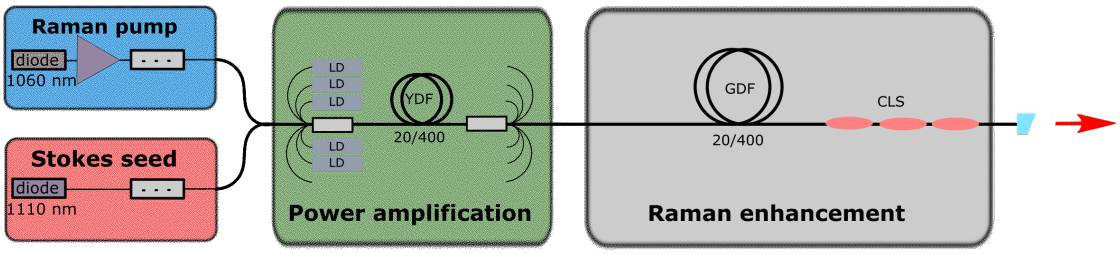

Figure 5.1: The simplified experimental laser setup, consisting of four main structural elements, that are described in detail in the text.

Raman pump laser

The seed laser of the Raman pump consisted of a laser diode stabilized with a fiber Bragg grating, delivering about 50 mW of linearly polarized light at a wavelength of 1060 nm. This laser diode was spliced to an electro-optic phase modulator to suppress any stimulated Brillouin scattering as described in (Zeringue et al., 2012; Harish et al., 2018). A combination of white noise and a sinusoidal was chosen as modulation signal, resulting in a 10 dB-linewidth of 428 pm. This seed laser was chosen because it was shown to induce little spectral broadening of the Stokes signal in chapter 4. The optical signal was then amplified to an output power of about 3 W in a 10/125 µm Yb-doped fiber, that received its energy from a single 976 nm laser diode coupled via a pump combiner. The length of the active fiber was 2.5 m, which corresponds to a total cladding absorption of approximately 13 dB at a wavelength of 976 nm. The signal emitted by this first amplification stage passed through an optical isolator, a spectral filter to reject amplified spontaneous emission and another optical isolator. The optical isolators had a combined isolation of more than 55 dB, which exceeded the gain in the following stage by more than 20 dB. This prevented any back-reflection from the high-power amplification element from disturbing the Raman pump seed laser. After the last optical isolator, a 99/1 fiber tap coupler allowed monitoring both the stability of the seed laser and the backwards travelling light. The latter was characterized with a power meter and a photodiode. This allowed monitoring the onset of stimulated Bril-

louin scattering as explained in chapter 4. Additionally, the effect of TMI in the high-power amplification element would also manifest itself in the backwards photodiode signal, as shown in (Möller et al., 2021). After the tap coupler, a wavelength division multiplexer was used to combine the Raman pump signal with the Stokes seed laser signal.

Stokes seed laser

For the first experiments presented in the following, the Stokes seed laser consisted of an external cavity laser diode delivering about 10 mW of linearly polarized light at a wavelength of 1110 nm[1]. The seed signals passed through a fiber coupled variable optical attenuator. This attenuator allowed changing the Stokes seed power without changing the driving current of the laser diode, which would require long warm-up times after each manipulation. A 99/1 fiber tap coupler was spliced to the output of the attenuator to monitor the power level and stability of the Stokes seed laser. The output power stability was ensured during all subsequently presented experiments, with a typical standard deviation of the power $< 2\,\%$ acquired over the course of an hour long measurement. As in the case of the Raman pump seed laser, the Stokes signal phase was modulated by an electro-optical phase modulator. After the modulator followed a set of optical isolators. The Stokes seed laser signal was then combined with the Raman pump seed laser signal by means of a wavelength division multiplexer.

High-power amplification element

The combined signals of Raman pump and Stokes seed were then fed into another wavelength division multiplexer that allowed coupling a signal at a wavelength of 1300 nm. This enabled the precise measurement of the fiber length of the high-power amplification element and the Raman enhancement element with an optical frequency domain reflectometer (OFDR), as demonstrated in (Soller et al., 2005; Beier et al., 2017a).

This device relies on a frequency-tuneable narrow-linewidth laser source that is split into two signals. One of them is coupled into the fiber under test, causing Rayleigh scattering. The backwards propagating parts of this Rayleigh

[1] In subsection 5.3.2 the Stokes seed laser is changed, and will remain that way thereafter, for more details see subsection 5.3.2.

scattering light are interfered with the second part of the signal. A Fourier-transform of the frequency-dependent interference signal allows to calculate a time-dependent intensity signal, which can be identified as a length-dependent signal since the speed of light in the fiber is known. As the reflective properties of the fiber change with the refractive index, longitudinal changes of the latter can be detected. This allows to access the precise localization of fiber splices, for example, as they are typically accompanied by small refractive index steps. Additionally, the longitudinal temperature change within the fiber core can be measured with this OFDR since this temperature change corresponds to a elongation of the fiber in space. This elongation in space results in a shift of the detected frequency of the intensity signal. To measure the temperature change, a reference measurement of the back-scattered signal in the cold state has to be acquired. The frequency-dependent signal of the cold state is then cross-correlated to the frequency-dependent signal of the warm state. The resulting frequency shift corresponds to a temperature change that is initially calibrated for example by a controlled temperature change of the environment. However, if the correlation is too weak, no temperature change can be calculated. This is the case, for example, for very long fibers, i.e. fibers with too much propagation loss, as the back-scatted signals are too weak. This correlation is also impossible if there are significant Stokes signals (approximately $> 10\,\mathrm{W}$ in our case) present in the fiber. The reason for this behavior is not entirely clear, but it is presumably backwards propagating higher order Stokes signals preventing the correlation.

The second wavelength division multiplexer was followed by a mode-field adapter that connected the polarization maintaining $10/125\,\mu\mathrm{m}$ fibers used so far to the $20/400\,\mu\mathrm{m}$ fibers used from now on. It has to be noted that these large mode area fibers were not polarization maintaining. This is because high-power PM fibers were not available during the time of this work, which is likely to change in the near future. Therefore, the polarization state at the input of the large fiber is not clear, because the non-PM fiber has a rotation symmetry which precludes a precise orientation during fiber splicing.

A fused coupler combined the $20/400\,\mu\mathrm{m}$ fiber together with six $200/220\,\mu\mathrm{m}$ multi-mode fibers into a single $20/400\,\mu\mathrm{m}$ fiber. This $1:6+1$ combiner was used to couple $976\,\mathrm{nm}$ light to excite the Yb-ions in the following active fiber. There were five laser diodes used, emitting up to $500\,\mathrm{W}$ each. The active fiber was a double-cladding Yb-doped $20/400\,\mu\mathrm{m}$

fiber. This fiber, with core NA $= 0.065$, had a peak cladding absorption of approximately $\alpha = 1.9\,\mathrm{dB/m}$ at a wavelength of 976 nm. The active fiber had a length of 12 m[2]. The fiber was coiled on a metal, water-cooled spool of 12 cm diameter. This diameter was chosen based on fiber bend loss measurements performed with the method described in the appendix of (Möller et al., 2020b). These measurements revealed that the fiber is single-mode for 12 cm coiling diameter for both the Raman pump and the Stokes wavelength, which is desirable to suppress TMI and to reduce the heat at the $1 : 6 + 1$ combiner. The fiber was additionally put inside a swirling water basin for further cooling.

The active fiber was followed by another $1 : 6 + 1$ combiner. The light of one of the coupler arms was directed onto a dichroic mirror, enabling the measurement of the power (averaged over several seconds) of 976 nm and Raman pump light in that arm. Additionally, the Raman pump light emitted from the coupler arm was measured using a photodiode, which allowed for a temporal resolution in the kHz-region which is characteristic for TMI. These measurement parameters are used to verify that TMI did not occur in the high-power amplification element. This enables to locate the place of origin of TMI occurring in this setup to places before or after the $1 : 6 + 1$ combiner. The high-power amplification element ends with the second $1 : 6 + 1$ combiner, marking the beginning of the Raman enhancement element.

Without this Raman enhancement element and without Stokes seed, the output power stability of the standard deviation of the Raman pump power was $< 0.8\,\%$ acquired over the course of a 50 min long measurement at an output power of 1 kW.

Raman enhancement element

The Raman enhancement element consists of a passive, Germanium-doped 20/400 µm fiber, which structure was shown previously in Figure 2.1. The length of this passive fiber could be varied through several cut-backs. For the following subsection 5.3.1 it was chosen to be 16 m[3]. The passive fiber was coiled with a bending diameter of 20 cm to keep the bend losses of the Stokes modes low, which was verified by numerical simulations. The fiber was

[2] In subsection 5.3.3 and subsection 5.3.4, the length was 11.2 m.

[3] In subsection 5.3.4 the passive fiber length is changed, which is discussed in detail in that section.

put into the same water basin as the active fiber. There was still a significant amount of cladding light at the fiber output, which led to the application of three different cladding light strippers (CLS) towards the fiber end: First a CLS, etched with hydrofluoric acid (Ulfalux SG 500, 20 min etching time). This was followed by a straight CLS based on index matched silicone (NuSil LS-3354). Finally a bent CLS based on the same silicone was used. Each of the CLS removes cladding light of different numerical aperture and their order ensures a minimal temperature on the last CLS, that unfortunately remained a thermal limitation of the system. The last 2 meters of fiber were loosely coiled in a water flooded tube. An angled end cap with anti-reflective coating, with a reflectance of $R < 0.3\,\%$ for wavelengths between 900 nm and 1120 nm was spliced to the fiber output. This end cap provided suppression of the reflection back into the core by more than 60 dB.

5.2.2 Beam and setup characterization methods

The experimental setup was thoroughly characterized and Table 5.1 lists all the parameters measured and the measurement devices.

The separation of the Raman pump and Stokes signal was achieved by using specially designed dichroic mirrors with up to 19.8 dB difference in reflectivity at those two wavelengths. The beam was sampled with several fused silica (Corning 7979) wedges placed under a small angle. Air circulation of cooling fans and vibrations of the water cooling was reduced. The photodiode measurements were done similar to (Otto et al., 2012), with the slight improvement, that a single-mode fiber was used as the pinhole and it was placed at the center of the beam near field image. Overframing was ensured by choosing a suited focal lens. The output of that single-mode fiber was then shone onto the photodiode. This technique enables to always measure the same spatial beam sample, which allows direct correlation between different signals. To this end, the fiber position is tuned to the center of the beam in the focal plane (i.e. maximizing the transmitted signal power during stable laser operation). With the photodiodes at the $1:6+1$ combiner, mentioned in subsection 5.2.1, it is possible to identify the place of origin of the TMI to either be within the high-power amplification element or within the Raman enhancement element.

This experimentally realized RFA transfers the signal from a wavelength

Table 5.1: Overview of the experimental parameters observed and devices used thereto.

Parameter	Measurement device
Total output power	Coherent PM3K
Raman pump and Stokes fraction	Thorlabs S120C
Unabsorbed 976 nm light at the $1:6+1$ combiner	Thorlabs S350C
Raman pump light at the $1:6+1$ combiner	Thorlabs S350C
Stokes seed laser power	Thorlabs S120C
Raman pump backwards power	Thorlabs S302C
Raman pump output stability	Thorlabs PDA015
Stokes output stability	Thorlabs PDA015
Pump backwards stability stability	Thorlabs PDA015
Pump $1:6+1$ combiner stability	Thorlabs PDA015
Optical spectrum	Yokogawa OSA
Raman pump beam quality	Cinogy CinSquare CS200
Raman pump and Stokes beam profile	Optronis CamRecord 5000
Temperature along the fiber/ fiber length	Luna OBR-4613

of 1060 nm to a Stokes wavelength of 1110 nm. The quantum defect of such a wavelength shift amounts to about 5 %, which is comparable to the 8 % usually reached for Yb fiber lasers. Thus, the heat load caused by SRS in this system is comparable to the quantum defect heat load of conventional fiber laser systems. Therefore, prior to this work, it was presumed that TMI might occur in Raman fiber amplifiers (Naderi et al., 2016), which is experimentally verified in the following section 5.3. The realized RFA allows for a Stokes output power of several hundred Watts, which is considerable higher than the Stokes powers presented in the investigations on the interaction of SRS and TMI for active fibers explained in section 5.1. While there, TMI was most likely caused by a perturbation of the laser process in the active fiber, the setup presented here is suitable to examine SRS-induced TMI in a passive fiber, as shown in the following section.

5.3 Examination of SRS-induced TMI in a passive fiber

TMI in a passive fiber RFA was numerically investigated by (Naderi et al., 2016). Several predictions are made in that work: First, it is stated that SRS-induced TMI in passive fibers exist. For the used fiber parameters (15 µm core size, 0.05 NA) the Raman induced TMI threshold is expected to be approximately 550 W. Second, it is predicted that the TMI threshold does not depend on the fiber length for cladding-pumped RFA (Naderi et al., 2016). For core-pumped RFA, it is stated that a dependence of the threshold on the fiber length is possible due to a wavelength-dependent difference of the propagation constant of the fundamental (FM) and higher order modes (HOM). However, the influence of this effect was predicted to be small ($\mathcal{O}(1\,\%)$, depending on the fiber parameters). Specifically, they numerically calculated a reduction of the Stokes power at the TMI threshold of 7 % when reducing the fiber length from 50 m to 10 m.

With the experimental method explained in the previous section, these predictions could be tested. Indeed SRS-induced TMI were experimentally observed. The localization of the origin of TMI to inside the passive fiber is presented in subsection 5.3.1. Thereafter, the influence of some key parameters of the laser setup is experimentally investigated: the seed laser noise charac-

teristics in subsection 5.3.2, the Stokes seed power in subsection 5.3.3 and the fiber length in subsection 5.3.4. The results of these investigations are discussed in section 5.4 which also widens the analysis to other parameters and future perspectives.

5.3.1 Observation of SRS-induced TMI in a passive fiber

Without the Stokes seed laser, and without the Raman enhancement element, the system emits a stable beam quality and power up to an output power of 1.9 kW. The onset of TMI was observed at an output power of 1.95 kW with a drastic increase in M^2 and photodiode fluctuations. The measured output power in the case of TMI actually drops slightly since the higher order mode is partially leaking into the cladding and is removed at the CLS at the fiber end. To use common TMI plotting and evaluation techniques from free-space and monolithic CLS free setups, the power slope of the stable region of the laser is extrapolated to the region showing TMI. This power is then referred to as *corrected output power*. In the stable region the beam quality of the setup was measured to be $M^2 = 1.3$, which is comparable to other values reported (Y. Li et al., 2017; Lee et al., 2019; Möller et al., 2018).

With the Raman enhancement element the laser power performance was similar, as shown in Figure 5.2 a). This figure displays the measured total power at the fiber output in both cases (with and without Stokes seed) as a function of 976 nm power. Additionally, for the case when the Raman enhancement element was used, the individual power in the Raman pump and in the Stokes signal at the fiber output is shown. Once the Stokes seed signal is introduced in the system, the total output power slope shows a slightly reduced efficiency towards high values, since a significant fraction of light is transferred from the Raman pump to the Stokes signal, undergoing an additional quantum defect.

For this thesis it is important to be aware of the location along the fiber where the power is transferred from the Raman pump to the Stokes signal. From subsection 2.2.2 and Equation 2.14 it is expected that in a co-pumped system without pump-depletion, like the one presented here, most of the power is converted by the Raman process towards the end of the fiber, i.e. in the Raman enhancement element and not in the active fiber. This implies that the temperature profile of the active fiber remains nearly unchanged. Thus, in

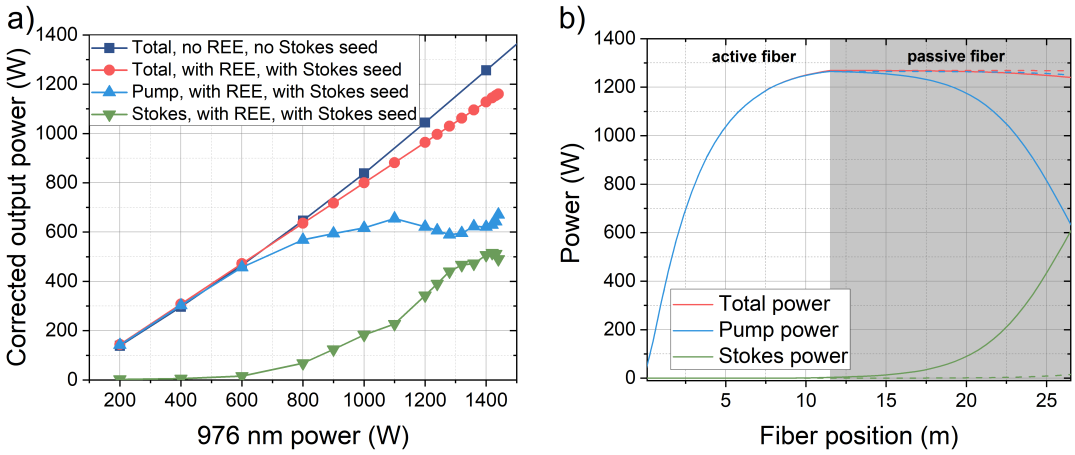

Figure 5.2: The power performance of the laser system with and without the Raman enhancement element (REE) (a) and the numerical simulation of the Stokes and Raman pump power along the fiber (b). The dashed lines in the numerical simulation represent the case without Stokes seed.

this setup SRS would only influence the TMI threshold of the active fiber via a disturbance of the phase shift, as in the experiment by (Hejaz et al., 2017), discussed in section 5.1, but not through an additional heat load. To strengthen this argument, a numerical calculation of the power evolution along the fiber was performed for which the steady-state rate-equations and power propagation including the Raman term were solved. The simulation parameters can be found in Table 5.2.

Table 5.2: Parameters used for the numerical calculation of the Stokes power along the fiber.

Parameter	Value
Input field	3 W at 1060 nm and 1 mW at 1110 nm
976 nm power	1.4 kW
Mode-field diameter	18 µm
Cladding diameter	400 µm
Active fiber length	11.5 m

The results of this calculation are depicted in Figure 5.2 b) and show that, while the Stokes power increases throughout the fiber, most of the energy is converted from Raman pump to Stokes towards the end of the Raman enhancement element. As a consequence the heat load caused by SRS is mainly

concentrated at the last few meters of this element.

This behavior was experimentally tested by measurements with the OFDR. Unfortunately the device is unable to measure the temperature in regions with significant Raman content as explained in subsection 5.2.1. Thus, the temperature of the Raman enhancement element cannot be directly measured. However, since the temperature in the total active fiber remains unchanged with and without the Stokes seed, as shown in Figure 5.3 a), this is evidence for the Raman process mainly happening after the active fiber.

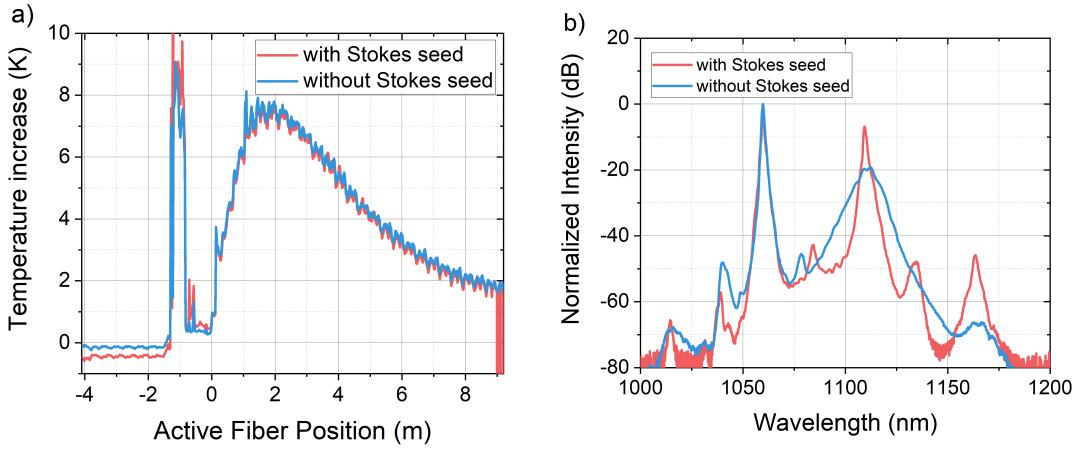

Figure 5.3: The temperature of the active fiber at an output power of 1.2 kW in the case with and without Stokes seed laser (a). Spectral performance of the laser system with and without Stokes seed at 1.1 kW (b).

The output spectrum of the system is shown in Figure 5.3 b). Here, the performance with and without Stokes seed laser is shown at an output power of 1.1 kW. Two strong lines are visible in the spectrum: The Raman pump and the Stokes signal. It has to be noted that the optical spectrum measurement is not suited to extract conclusions about the relative power content in the Raman pump and the Stokes signal since the fiber attached to the optical spectrum analyzer acts as a single-mode filter, which leads to a varying coupling efficiency in the case of TMI, for example. As described in Table 5.1, the power ratio is, therefore, directly measured with powermeters.

Besides the Raman pump and the Stokes signal, there are other features visible in the optical spectrum: the second Stokes order around 1165 nm and some FWM peaks, which were already observed in chapter 4. The strength of these FWM peaks could be influenced by changing the orientation of the fiber bending. This is due to the polarized input state, as shown by (Haarlammert et

al., 2013). While the fiber is a non-PM fiber, a weak birefringence is introduced into the fiber through bending. This birefringence has two consequences.

First, the Raman gain is maximum if the polarization is preserved along the fiber and reduced by a factor of two if the polarization is scrambled, as shown by (Stolen, 1979). If the input polarization state is not aligned with the principal polarization axis of the fiber, the polarization will change periodically along the fiber. The beat-length of this change is slightly different for the Raman pump and for the Stokes wavelength. Therefore, the amount of Raman scattering will depend on the orientation of the input splice with respect to the fiber bending axis. Changing the first splice can, therefore, change the performance of the system. Consequently, for systematic investigations of the influence of different parameters, this first splice must not be changed or PM fibers must be used for all components. In the time frame of this thesis, kW-level, Yb-doped, single-mode PM fibers were not easily available, which will hopefully change with further research in the near future.

The second consequence of the weak fiber birefringence is an FWM gain that is dependent on the input polarization. For different bending diameters and orientations the phase matching condition is fulfilled at different wavelengths, as the input polarization changes. The different position and strengths of the FWM peaks in the presented spectra in comparison to those presented in chapter 4 can be explained that way. This argument strengthens the above-described need for high-power, Yb-doped PM fibers as well as the need for fixed splicing conditions. The latter were ensured in all systematic investigations presented later in subsection 5.3.3 and subsection 5.3.4.

TMI at the fiber output

Up to a corrected output power of approximately 900 W, the above described setup showed a Raman pump beam quality of $M^2 = 1.3$. The Raman pump and the Stokes signal were spatially separated by dichroic mirrors and guided towards a high-speed CCD camera. Figure 5.4 a) shows the measured near-field beam profiles at an output power of 650 W.

For higher output powers the Raman pump beam quality deteriorated to $M^2 = 1.8$ at 976 W corrected output power, but the beam profile remained temporally stable. The Raman pump beam profile, depicted in Figure 5.4 b), clearly shows a high HOM (LP_{11}) content. To understand this behavior the different

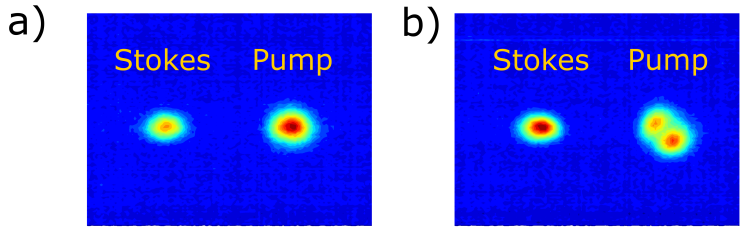

Figure 5.4: Measured beam profiles at an output power of 650 W (a) and 974 W (b).

transverse modes present in the fiber have to be considered: Raman pump FM and HOM as well as Stokes FM and HOM. Because the Stokes seed was mainly in FM, a beam cleanup to the Stokes radiation is present. Consequently, the Stokes beam profile remained Gaussian-like at this output power level. The Raman pump beam quality degradation can be understood as follows: the resulting Stokes mode profile has a higher overlap with the Raman pump FM, causing the latter to have a much higher Raman conversion efficiency than the Raman pump HOM (Christensen et al., 2016). This higher efficiency caused the ratio of Raman pump FM/HOM to decrease with increasing output power. Thus, the output beam profile changed from what seemed to be a pure FM profile to a clear mixture of FM and HOM.

While the ratio of the mode mixture changed with an increasing output power, the beam profile remained temporally stable up to a total output power of 1.1 kW. Beyond this power, the onset of TMI was observed. The Raman pump beam profile became unstable. A dynamic variation of relative mode content was observed, which manifested itself as a changing mode interference pattern of the FM and HOM on the camera and as can be seen in Figure 5.5.

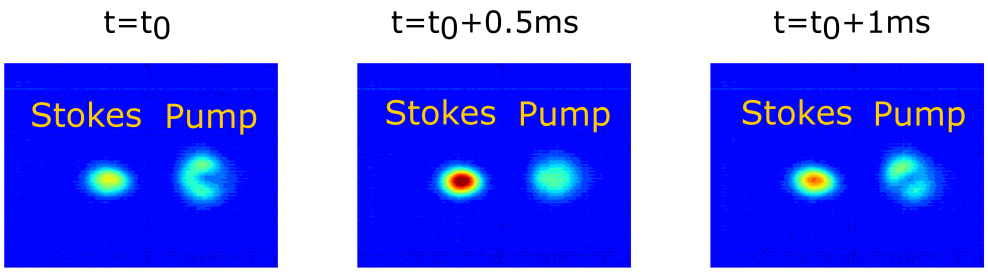

Figure 5.5: Measured beam profiles at a total output power of 1176 W at three different times.

The spectral discrimination between Raman pump and Stokes signals is necessary to fully understand the process. To illustrate this, Figure 5.6 shows the individual measured beam profiles next to a reconstructed combined beam profile at 1176 W total output power at an exemplary point in time. From the combined signal alone, the modal composition of pump and Stokes cannot be deduced.

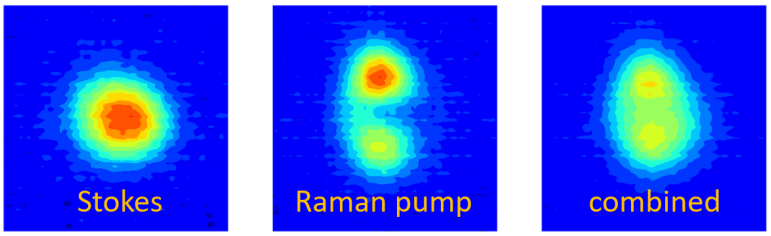

Figure 5.6: Exemplary measured beam profiles of Stokes and pump beam next to a reconstructed combined beam at a total output power of 1176 W.

A modal decomposition algorithm, which is explained in more detail in subsection 5.3.3, was programmed, similar to (Stutzki et al., 2011). A combination of FM and HOM was fitted to the beam profile images with their respective amplitudes and phases as fit parameters. A clear fluctuation of the mode composition of the Raman pump with kHz-frequency was observed that way, as depicted in Figure 5.7.

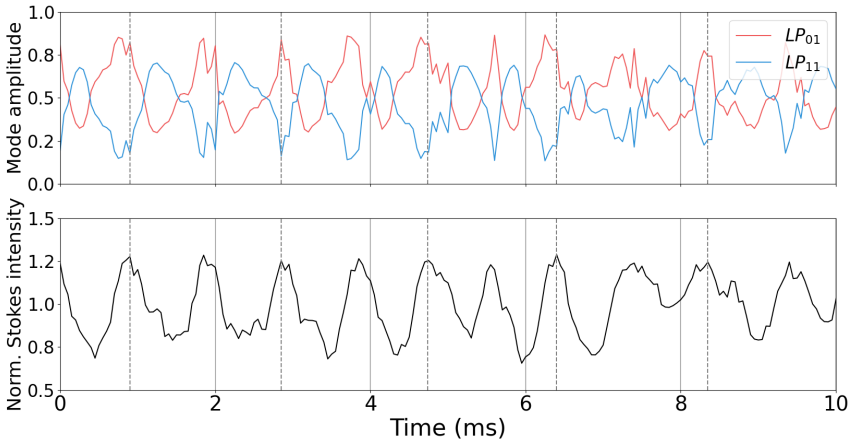

Figure 5.7: Mode amplitude of the measured Raman pump beam profile over time (top) and measured Stokes beam intensity over time (bottom) for an exemplary time period.

While the Raman pump beam showed strong modal fluctuations (TMI), the

Stokes beam exhibited a more stable beam profile with a fluctuating intensity. Figure 5.7 shows the Stokes intensity over time for the same time period as the Raman pump beam profile.

This intensity fluctuation was synchronized to the mode fluctuations of the Raman pump and can be explained by the latter. The two Raman pump modes have a different Raman conversion efficiency, as mentioned before. The higher the Raman pump FM fraction is, the higher is the Raman conversion and the higher is the Stokes intensity. However, the synchronization between the Raman pump mode fluctuation and the Stokes intensity was not perfect, which becomes clear at the maximum positions indicated by the dotted lines in Figure 5.7. The reason for that is probably electronic and other noise of the camera disturbing the numerical fit. At even higher output powers, the Stokes beam profile was seen to fluctuate in shape as well. This Stokes beam behavior will be discussed further in subsection 5.3.3.

SRS as cause of the TMI

To verify whether the observed TMI were caused by SRS, experiments with and without the Raman enhancement element and with and without the Stokes seed signal were conducted. In the different cases, photodiode signals of the Raman pump output were acquired as explained before. These photodiode signals were evaluated as described by (Otto et al., 2012; Beier et al., 2018): Each photodiode signal was split into equal-sized traces which were each normalized to their average value. For each slice the standard deviation was calculated, along the mean standard deviation of the total photodiode signal. The results of this analysis, shown in Figure 5.8 clearly indicate that the TMI threshold at approximately 1.2 kW is only present in the case with Stokes seed and the Raman enhancement element.

This threshold is far below the threshold of the high-power amplification system alone, which is 1.95 kW. This proofs that the observed TMI were, indeed, SRS-induced. However, since there is no optical isolation between the Raman enhancement element and the high-power amplification element, their origin is still unclear at this point. They could either be formed by a perturbation of the active fiber or originate in the passive fiber. This will be investigated in the following section.

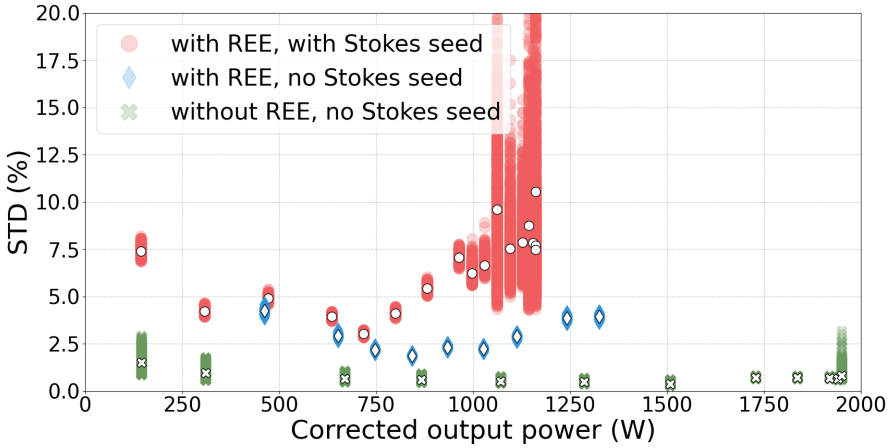

Figure 5.8: Standard deviation of the photodiode traces with and without Stokes seed as a function of the total output power in comparison to the active fiber alone (without Raman enhancement element, REE).

Localization of TMI origin

The localization of the origin of the observed SRS-induced TMI was made possible by the different measurement ports listed in Table 5.1. Mainly the power and stability at the $1:6+1$ combiner with respect to the stability at the fiber output enabled that localization. Bend loss measurements and simulations revealed that with the bending diameter of the active fiber used here, a significant amount of HOM content should couple out of the fiber core into the fiber cladding. This light will then be partially guided towards the multi-mode ports of the $1:6+1$ combiner. Due to the long fiber lengths and large number of transverse modes in the fiber cladding, all multi-mode ports of the $1:6+1$ combiner are receiving approximately the same amount of this light. Thus, if TMI is present in the active fiber, the overall power at a multi-mode $1:6+1$ combiner port will increase. Additionally, this power will also fluctuate with the characteristic kHz-frequency of the TMI. The standard deviation and power measured at this port over the total output power is depicted in Figure 5.9, in comparison to the same analysis at the fiber output.

It becomes clear that the signal at the fiber output already showed TMI at a power of 1060 W while the the $1:6+1$ combiner only showed TMI at a power of 1160 W. Only at this output power level does the power at the multi-mode $1:6+1$ combiner port drastically increase, as shown in Figure 5.9. This demonstrates that the observed TMI at 1060 W originate in the passive fiber. At

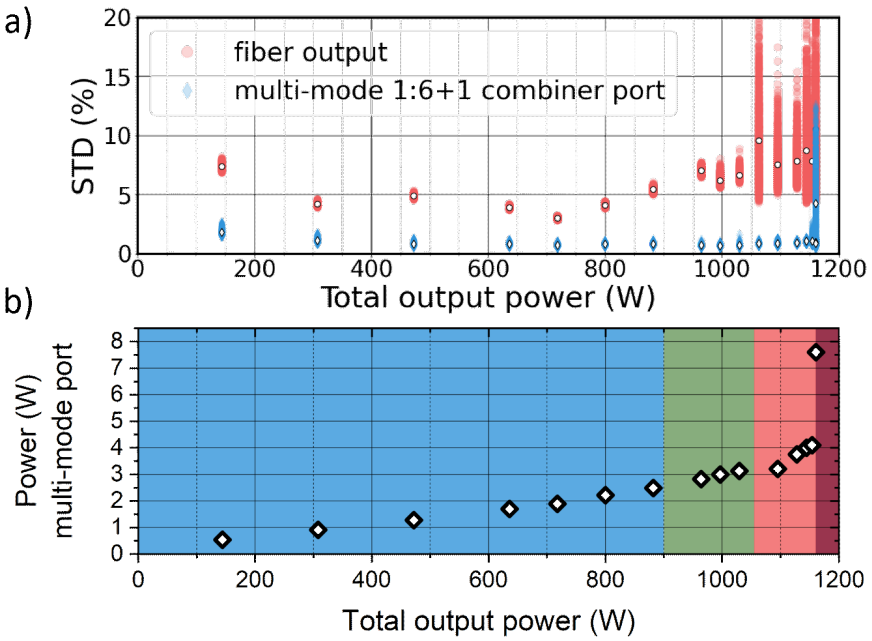

Figure 5.9: Measured standard deviations at the fiber output and the multi-mode $1:6+1$ combiner port (a) and the signal power at the the multi-mode $1:6+1$ combiner port (b) over total output power.

output powers above 1160 W TMI are present in the active fiber, as seen from the last value with increased power at the multi-mode $1:6+1$ combiner port. The TMI threshold of the active fiber with Raman enhancement element and Stokes seed is considerably lower than the threshold of the active fiber alone, shown previously in Figure 5.8. Therefore, the strong Stokes signal and/or TMI in the passive fiber disturb the stability of the active fiber, possibly through back-reflected signals acting similar to an intensity noise.

The background colors of Figure 5.9 correspond to the different overall beam stability behavior regimes with increasing output power (first a stable operation, then TMI in the passive fiber and then TMI in the active fiber). This behavior also manifests itself in the Fourier-transformations of the photodiode signals. As the observed beam fluctuations occur with frequencies in the low kHz-region, as expected for TMI (Johansen et al., 2013; Otto et al., 2012), this region is of special interest. A comparison of the Fourier-transformed photodiode signals at the fiber output and at the multi-mode $1:6+1$ combiner port is shown in Figure 5.10.

Low-kHz components appear when the systems changes from stable operation below the TMI-threshold at 636 W to the unstable operation at 1144 W.

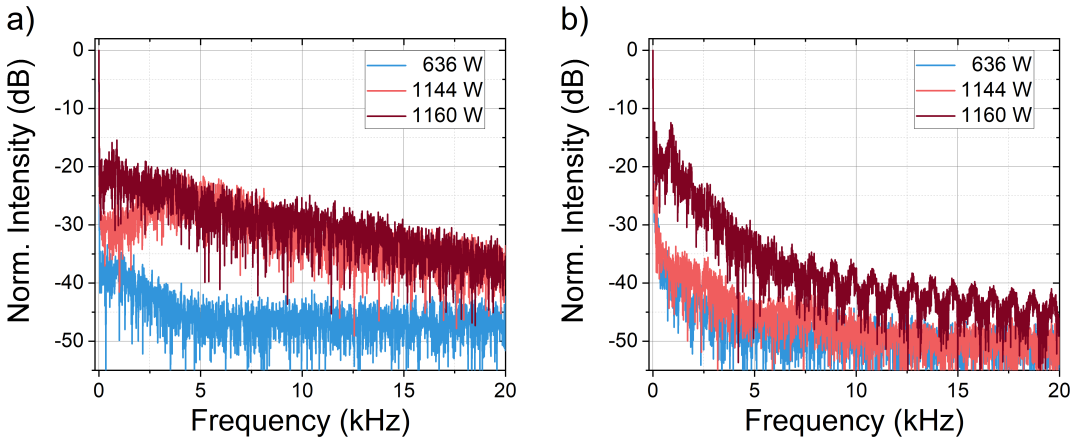

Figure 5.10: Fourier-transform of the photodiode signals at the Raman pump wavelength at the fiber output (a) and at the multi-mode $1:6+1$ combiner port (b) for different output powers. The colors correspond to the different regimes indicated in Figure 5.9.

However, they do only appear at the fiber output (Figure 5.10 a), not at the multi-mode $1:6+1$ combiner port monitoring the active fiber (Figure 5.10 b). This confirms the localization of the origin of the initial TMI to be within the passive fiber. This finding is of high importance as it implies that SRS-induced TMI potentially limits beam delivery fibers used in many different applications. Only at 1160 W does the active fiber become unstable, visible in the increase of low-kHz components at the multi-mode $1:6+1$ combiner port depicted in Figure 5.10 b). These components are then also visible at the fiber output.

In the following, key parameters influencing SRS-induced TMI in passive fibers are investigated. The above presented technique of monitoring the active fiber through the $1:6+1$ combiner was applied to all subsequently presented experimental investigations. This ensured that only SRS-induced TMI originating in the passive fiber was observed and that common TMI of the active fiber are excluded.

5.3.2 Considerations of the laser intensity noise

As described in section 2.3 the noise characteristics of the laser system have a significant impact on the TMI threshold (Stihler et al., 2020). In a Raman fiber amplifier, intensity noise can either originate from the Raman pump laser or the seed laser.

On the Raman pump laser noise

For Yb-doped fiber laser systems, an analysis of the noise transfer function showed that the 976 nm noise of the last amplification stage has the biggest influence (Gierschke et al., 2019). Such an Yb-doped fiber laser system is utilized here as pump source. Thus the high-power 976 nm laser diodes are responsible for most of the Raman pump noise in the system. Due to the short response time of the stimulated Raman scattering, there can be a strong intensity noise transfer from Raman pump to signal (Fludger et al., 2001). Therefore, throughout the experiments presented in the following, the same 976 nm laser diodes were used. While this is no optimization of the noise characteristics, it at least ensured constant Raman pump noise conditions. An improvement of this Raman pump intensity noise will be discussed later.

On the Stokes seed laser noise

The external cavity diode laser used so far as Stokes seed source has satisfactory noise characteristics. Unfortunately, this source had the disadvantage of being limited to output powers below 10 mW. This power was attenuated even more by the insertion losses of the elements composing the Stokes seed laser, especially the necessary optical isolators. FBG-stabilized laser diodes enable much higher output powers, but they usually have worse noise characteristics. To test the influence of the choice of seed laser on the SRS-induced TMI threshold, the same system was used with two different sources: An external cavity diode laser and a PM FBG-stabilized laser diode, both operating at a wavelength of 1110 nm. To ensure equal conditions the same seed power levels were fed into the system, by the use of the variable optical attenuator. A sufficient warm-up period was given to each seed laser. The results are depicted in Figure 5.11.

The SRS-induced TMI threshold behavior of the system was observed to be the same for the two seed lasers within the measurement uncertainty. The same performance of the two seed lasers allowed using the laser diode with higher output power. This enabled to vary the power of the Stokes seed laser. The influence of this parameter on the SRS-induced TMI threshold is described in the following subsection 5.3.3.

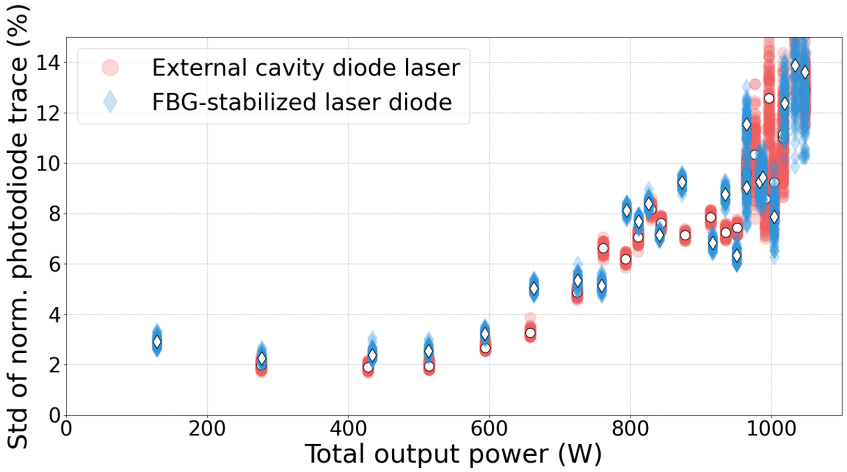

Figure 5.11: Standard deviation of the photodiode signals over output power of the system with two different seed sources: an external cavity diode laser (red) and an FBG-stabilized laser diode (blue).

5.3.3 Influence of the Stokes seed power

To examine the influence of the Stokes seed power on the SRS-induced TMI threshold, this parameter was systematically varied. Here, the Stokes seed power was changed between 4 mW and 21 mW. This was done with an optical variable attenuator, so that the seed driving current and, thereby, the seed noise characteristics were unchanged. The variation range was limited by the available output power of the seed laser on one hand and by the strong pump powers required for amplification of weak Stokes seed signals to high output power levels for a given fiber length on the other hand. A numerical simulation of the Raman amplification was performed for which the steady-state rate-equations and power propagation including the Raman term were solved. Figure 5.12 shows the development of the Stokes output power along the passive fiber (where the Raman amplification mostly takes place) for different Stokes seed powers at a 976 nm power of 1.1 kW and the fiber parameters as in Table 5.2. The Stokes power increases with passive fiber length. Consequently, the total Raman conversion efficiency, defined as the ratio of the Stokes power to the total output power, also increases with passive fiber length. This is similar for the Stokes seed power: The higher the Stokes seed power, the higher the efficiency. Figure 5.12 also depicts the corresponding local heat load along the fiber. It becomes clear that changing the Stokes seed power shifts the position of the maximum of the local heat load. However, the integrated heat load for

a specific *extracted* Stokes power is the same, as the Raman process is the only heat source in the passive fiber. This means that for the same extracted Stokes power, the total heat load in the fiber will also be the same.

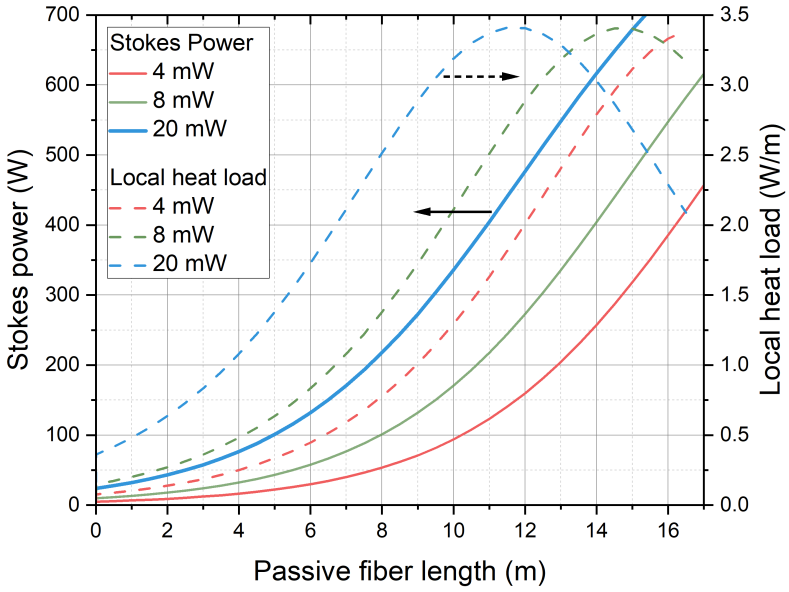

Figure 5.12: Numerical simulation of the Stokes power along the passive fiber for different Stokes seed powers together with the corresponding local heat load.

In the experiment, for each Stokes seed power, the 976 nm power was incrementally increased and the beam profile was measured with the high-speed camera. The qualitative behavior was as described above: With increasing output power the Raman pump shows first stable FM operation, then a more dominant HOM, and finally a fluctuating beam profile.

To compare the quantitative behavior a mode fitting algorithm was applied to the beam profile. The main part of this algorithm consists of fitting a combination of FM (LP_{01}) and HOM (even and odd LP_{11}) to the measured profile at each frame acquired by the high-speed camera. This fitting has four free parameters: Two phases and two amplitudes. The third modal amplitude is given by the assumption that the squared sum of them should equal unity, which neglects all other higher order modes. Unfortunately, there are more free parameters of the measurement such as the overall beam size and the central beam position. Adding these free parameters to the fitting procedure

would preclude conversion of the fit. However, the overall beam size is given by the fiber core size, the used optical lenses and the CCD-pixel size and can be calibrated initially. The central beam position is, ideally, also fixed by the used optical path. However, there are small fluctuations between the different acquisitions due to technical reasons such as different optical attenuation for different output powers, resulting in slightly different optical paths of the beams. The optimal central beam position is found by automatically performing a fit for many initial values and choosing the result with the lowest total fit residuals.

Thereby, the FM and HOM mode amplitudes are retrieved over time for each measured output power. Calculating the standard deviation of the FM mode content from these traces enables to easily access the TMI threshold. Note that for fibers and systems where the HOM content is completely filtered out before the fiber output (for example through very tight bending), the beam fluctuation is not visible on the camera and, thus, cannot be used for analysis. The mode fitting method was benchmarked against the traditional theory of measuring TMI with a photodiode (Otto et al., 2012). The two methods showed similar results and the resulting standard deviations were highly correlated with a Pearson correlation coefficient of $r > 0.8$.

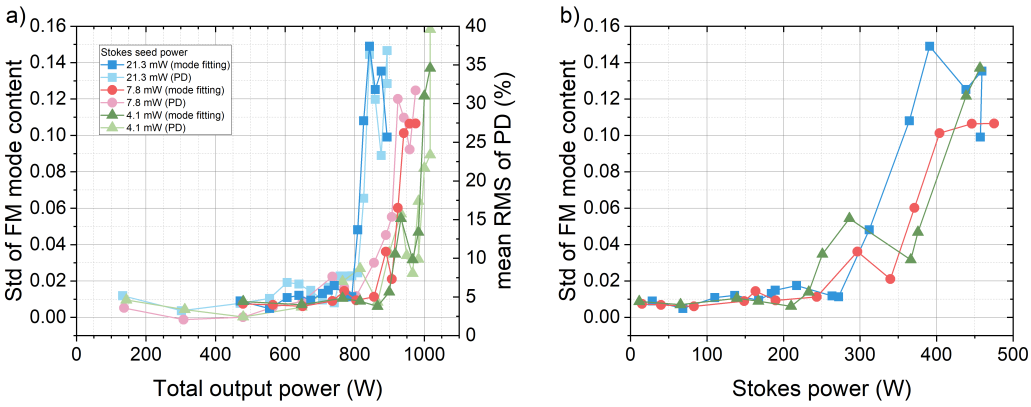

Figure 5.13: Standard deviation of the Raman pump FM mode content over the total output power (a) and the Stokes output power (b) for three different Stokes seed powers at a fixed passive fiber length of 17.5 m. For comparison, the corresponding photodiode values are shown for the total output power but omitted for the Stokes power for better visibility.

Figure 5.13 shows the result of both techniques for three different seed powers at a fiber length of 17.5 m over the total output power (a) and the Stokes power (b) for different Stokes seed powers. The total output power

shows a clear trend: The higher the Stokes seed power, the lower the total output power (the sum of Raman pump and Stokes signal) at the SRS-induced TMI threshold. However, the Stokes output power of the TMI threshold does not show a clear trend. Thus, while the efficiency of the RFA changed with different Stokes seed power, the threshold occurred at the same Stokes power within the measurement uncertainty. These observations largely validate the theoretical work of (Naderi et al., 2016).

The above presented modal analysis of the Raman pump signal was additionally applied to the Stokes signal measured during the same experiments. Again, TMI is manifested as an increase of the standard deviation of the FM content.

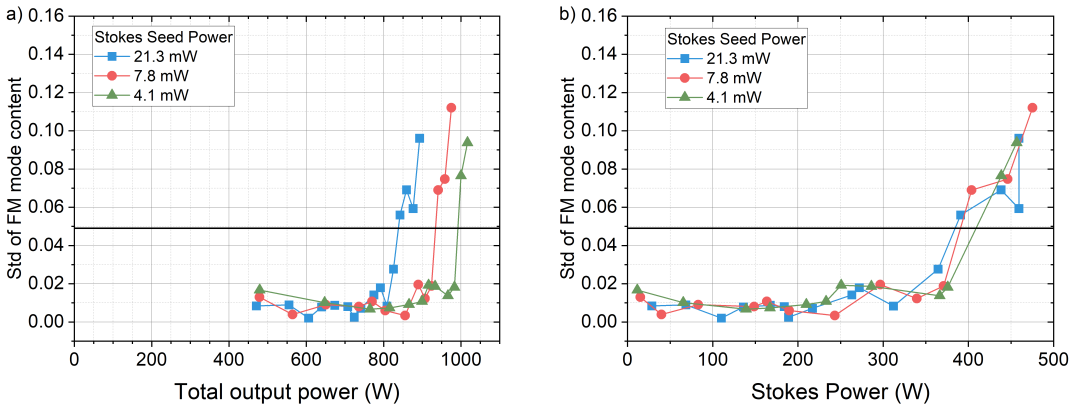

Figure 5.14: Standard deviation of the Stokes signal FM mode content over the total output power (a) and the Stokes output power (b) for three different Stokes seed powers at a fixed passive fiber length of 17.5 m.

The results are depicted in Figure 5.14. The behavior of the Stokes signal is similar to that of the Raman pump: The higher the Stokes seed power, the lower the total output power at the SRS-induced TMI threshold. The comparison to the results of the Raman pump beam analysis (Figure 5.13) shows significant differences between the Raman pump beam and the Stokes beam. For quantification, an increase of the initial standard deviation by a factor of 5 can be chosen as threshold definition[4], which leads to the values given in Table 5.3. This threshold is indicated by the horizontal black line in Figure 5.14.

The Raman pump reaches the TMI threshold at lower output powers than the Stokes signal. As the measurements of the Raman pump and Stokes beam

[4]There are several different TMI threshold definitions in use, such as using the derivative of an exponential fit (Otto et al., 2012). The fivefold increase was proposed by (Johansen et al., 2013) and used here as it was successfully applied to similar fibers in (Beier et al., 2018).

Table 5.3: Total output powers at the TMI threshold of the Raman pump and Stokes signal for three different Stokes seed powers.

Stokes seed power	21.3 mW	7.8 mW	4.1 mW
Raman pump threshold	800 W	911 W	971 W
Stokes threshold	829 W	930 W	988 W

profile were taken simultaneously, these differences are beyond the measurement uncertainty. It has to be noted that such a behavior is not contradictory to measurements that showed a lower TMI threshold for longer wavelengths (Beier et al., 2017b) as in those cases the signal wavelength was changed each time and no additional signal was present. In the experiment present here on the other hand, there were two signals present in the fiber at the same time. There are several possible mechanisms that might explain the higher TMI threshold of the Stokes signal.

The first explanation is the refractive index grating responsible for TMI of the Raman pump which might act upon the Stokes signal. However, while the spectral width of the RIG causing TMI has unfortunately not been measured to date, it is expected to be smaller than the wavelength difference between pump and Stokes. The reason for that is the long fiber length (several meters) over which the RIG is formed, resulting in many grating periods experienced by the Stokes signal. The spectral width of the RIG, probably reduces with length, as does the spectral width of long-period gratings (Ramachandran et al., 2002). Nevertheless, energy converted to the HOM after a small number of grating periods is not converted back, so the strength of the direct coupling between the Stokes modes caused by the Raman pump RIG is unclear.

The second effect is the conversion of Raman pump HOM to Stokes HOM, that is nonzero, albeit being weaker than the FM conversion efficiency. Consequently, the Stokes signal is composed of FM and HOM, possibly undergoing the same dynamic as the Raman pump signal. Because the conversion efficiency is higher for the FM, a beam cleanup takes place which stabilizes the Stokes signal, resulting in a higher TMI threshold of the Stokes signal compared to the Raman pump.

The third effect is the wavelength-dependency of the coupling efficiency between the FM and HOM for a RIG. It is known that the coupling efficiency between these modes decreases with wavelength (Dong, 2013; Hansen et al.,

2013). As the Stokes signal has a longer wavelength, it experiences a lower coupling between FM and HOM resulting in a higher TMI threshold.

To identify which of the above explanations is most important for the observed behavior remains a challenge for future research. To this end, a measurement of the spectral width of the RIG causing TMI should be conducted.

Coming back to the experimental data, it is noteworthy that the analysis of the Stokes signal beam stability, depicted in Figure 5.14 enables a clear threshold determination. The Stokes power at the TMI threshold is the same within a margin of $398\,\mathrm{W} \pm 12\,\mathrm{W}$ for all three Stokes seed powers, with the threshold definition as before. Since the total output power at the SRS-induced TMI threshold decreased with increasing Stokes seed power, the total efficiency of the RFA was changed. In summary, while the efficiency of the RFA changed with different Stokes seed power, the threshold occurred at the same Stokes power within the measurement uncertainty. As for the analysis of the Raman pump, these observations largely validate the theoretical work of (Naderi et al., 2016), commented in the introduction of section 5.3.

Another way to test the behavior of SRS-induced TMI and the theoretical prediction made by (Naderi et al., 2016) is to vary the overall conversion efficiency of the RFA, that is to change the passive fiber length, which was done in the following subsection 5.3.4.

5.3.4 Influence of the fiber length

To examine the influence of the fiber length on the SRS-induced TMI threshold, the passive fiber length was changed between 17.5 m and 14 m. This was done by opening an existing fiber splice after the $1:6+1$ combiner, cutting out a specified fiber length and re-splicing the fiber. A conventional cut-back from the fiber end was not possible due to the need for a water-cooled fiber end cap. However, the technique used here also prevents additional fiber splices. Due to the symmetry of the fiber, the redone splice was not necessarily in the same rotation direction as the previous one. This might have led to a slightly different fiber torsion changing the birefringence of the fiber. Additionally, the total birefringence of the fiber, which is induced by the fiber coiling, changes with the coiled fiber length. However, the passive fiber was coiled on a large diameter of 20 cm which induces little birefringence and, thus, these effects can be neglected here. For all investigates presented here, all other splices

were kept untouched and the length of the tightly coiled active fiber remained constant.

For every fiber length the 976 nm power was incrementally increased and the beam profile was measured with the high-speed camera. The qualitative behavior was as described above: with increasing output power, the Raman pump shows first a stable operation, then a more dominant, static HOM content and finally a fluctuating beam profile. The measurement data was analyzed as described in subsection 5.3.3.

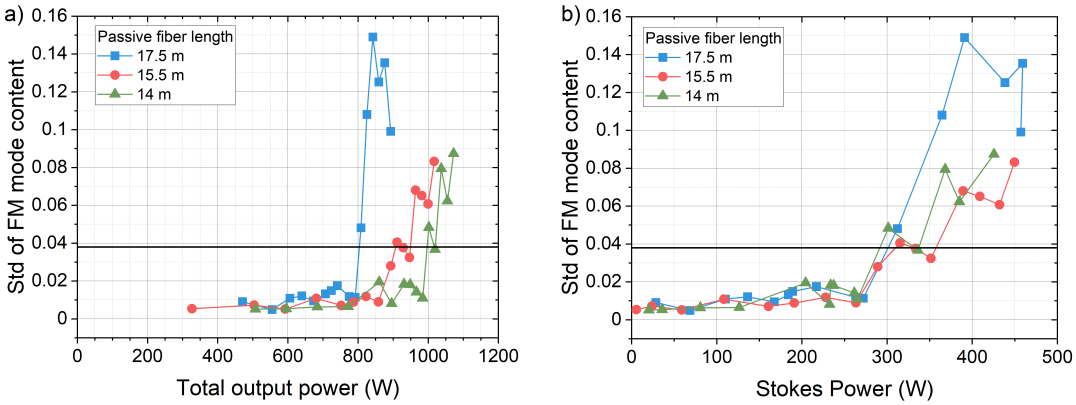

Figure 5.15: Standard deviation of the Raman pump FM mode content over the total output power (a) and the Stokes output power (b) for three different fiber lengths at a fixed seed power of 21 mW.

Figure 5.15 shows the resulting standard deviation of the Raman pump FM mode content at a seed power of 21 mW over the total output power (a) and the Stokes power (b) for different fiber lengths. The total output power shows a clear trend: the longer the fiber length, the lower the total output power at the SRS-induced TMI threshold. If an increase of the initial standard deviation by a factor of 5 is chosen as the TMI threshold definition, the total output powers at the TMI threshold with increasing fiber length are 997 W, 908 W and 804 W. On the other hand, the Stokes power shows a different behavior: Here, the threshold is the same , i.e. within a range of 301 $\pm$ 10 W Stokes power for all fiber lengths.

This fiber length variation measurements were not only done with a Stokes seed power of 21 mW, but the two other Stokes seed powers shown in the previous section were also tested. At a Stokes seed power of 8 mW the TMI threshold behavior was the same: The total output power at the TMI threshold decreases with increasing fiber length and the Stokes power at the TMI

threshold is the same.

At an even lower Stokes seed power of 4 mW, the trend was observed to be the same for the two longer fiber lengths. Unfortunately, at the shortest fiber length and at the lowest seed power thermal limitations (at the last CLS) occurred before the Stokes power was strong enough to reach the SRS-induced TMI threshold. This is because the Raman conversion efficiency decreases with fiber length as well as with Stokes seed power which requires a larger pump power and, thus, larger heat load at the CLS, to reach the same Stokes power.

In summary, while the total Raman conversion efficiency at the TMI threshold of the RFA with a Stokes seed power of 21 mW changed with increasing fiber lengths from 30 % to 37 % , the threshold occurred at the same Stokes power. These observations largely validate the theoretical work of (Naderi et al., 2016). This finding implies that the total heat load is important for the SRS-induced TMI threshold as will be discussed in the following section 5.4.

5.4 Discussion and influence of further parameters

The fiber length variation showed that the Stokes power at the TMI threshold is nearly independent of the total Raman conversion efficiency of the RFA and, likewise, the variation of the Stokes seed power showed a similar result: while the total TMI threshold power (i.e. considering both the Raman pump and the Stokes signal) showed a clear trend, the Stokes power at the TMI threshold did not. Therefore, the results of both experiments, i.e. the fiber length variation and the Stokes seed power variation, imply that the total heat load along the fiber is the key parameter for SRS-induced TMI. This suggests that the Raman gain distribution longitudinally along the fiber is not of great importance. Consequently, a bi-directional pumping optimization as done for Yb-doped amplifiers (T. Li et al., 2018) is not expected to be fruitful for RFA. While walk-off between the Raman pump and the Stokes signal may lead to a small threshold variation for core-pumped RFA and very long fiber lengths, for practical fiber configurations and cladding-pumped RFA TMI cannot be overcome by gain re-distribution along the fiber.

This leaves only few other optimization strategies to further increase the output power of RFAs. They will be discussed in the following to identify the more and less rewarding TMI mitigation strategies.

Input state

As the effect of TMI is induced by the presence of a higher order mode, both the Raman pump and Stokes signal should be in the fundamental mode. Consequently, perfect mode excitation should be achieved. Likewise, the fiber should have high losses for any HOM,which implies a reduction of the fiber V-number to as close to single-mode behavior as possible. This requires a careful fiber design with precise control over the index step for step-index fibers. In the experiment presented here the excitation was already nearly fundamental mode, as indicated by the good beam quality at low output powers. Thus, mode excitation alone will not greatly increase the SRS-induced TMI threshold.

However, the polarization of the input state is a property that can still be optimized. Unfortunately, the polarization of the input state relative to the fiber coiling axis could not be controlled in this thesis, due to the lack of high-power PM fibers, as explained in subsection 5.2.1. As these fibers are expected to be available in the near future, the influence of polarization control on the SRS-induced TMI threshold will then be examinable. A very recent theoretical investigation showed that the TMI threshold of a PM fiber can be increased by up to 50 % by using a linearly polarized input state whose polarization axes is oriented with an angle of 45 with respect to the main polarization axes of the fiber (Jauregui et al., 05.03.2021). This is caused by the dependency of the effective refractive index difference between FM and HOM on the polarization axes. This causes the MIP written in both fiber axes to have a different periodicity. As the two MIP are incoherently overlapping, the overall MIP will be locally washed out, resulting in a weaker RIG, resulting in a higher TMI threshold. This theoretical investigation agrees with recent experimental data (Lai et al., 2020) and gives a noteworthy strategy to increase the SRS-induced TMI threshold in applications that do not require a linear polarized output state.

Noise characteristics

In active fibers, an intensity noise improvement of the pump laser in the low kHz frequency region could lead to a significantly higher TMI threshold (Stihler et al., 2020). A similar behavior can be expected for Raman lasers.

During the course of this thesis, the intensity noise of the Raman pump lasers was measured relative to the fundamental quantum noise level (Popp

et al., 2020). To this end, an ECDL source operating at a Raman pump wavelength of 1064 nm was amplified in a Yb-doped, pm fiber to an output power of 1.89 W. This system is comparable to the Raman pump laser used in the above descried experiments. The system was characterized with a self-homodyne measurement setup, whose key component is a beam splitter and two identical, low-noise photodiodes, as well as electronics to add and subtract the detector signals. Since all classical noise is canceled out in the difference signal, only detector electronic noise and quantum noise remains in this signal. The added signal, on the other hand, contains classical as well as quantum noise. In that way, the classical noise could be calibrated to the quantum noise level. At a frequency of 10 kHz, the noise level of the amplifier was measured to be 59.9 dB above the quantum level, whereas the noise level of the ECDL at an output power of 5 mW was 14.9 dB above the quantum limit. This shows that there is a vast optimization potential of the noise level of the Raman pump laser used in the above described experiments investigating TMI.

To reduce the noise of the Raman pump laser it is desirable to improve the component which has the strongest contribution to the overall noise. Determining the noise transfer function of the system reveals that the final 976 nm laser diodes are the strongest noise contributor (Gierschke et al., 2019). A solution that compensates this noise with an additional low power 976 nm source and a fast electronic feed-back loop might be practical. A systematic study on that should be done in future work.

Fiber core size

The fiber core size has direct influence on the Raman amplification efficiency of the RFA (Equation 2.14). Consequently, for a larger core size, a longer fiber length is needed to achieve the same Stokes power. However, this does not change the total heat load and will, therefore, have only a minor influence on the SRS-induced TMI-threshold as described above. However, there is an influence of the core size on the beat length of the mode interference pattern, as was proposed for rare-earth doped fiber laser systems. The influence of the fiber core size on the TMI threshold in such systems is not entirely clear. On the one hand, an inverse dependency of the threshold on the square of the core diameter was theoretically derived (Zervas, 2019) and a similar behavior was found in (Tao et al., 2018). On the other hand, it was proposed that the core

size does not influence the TMI threshold if the V-number of a step-index fiber is left unchanged (Hansen et al., 2012).

In any case, keeping the V-number low is beneficial, as it decreases the HOM content. However, this requires very small refractive index steps between fiber core and cladding for step-index fibers with very large core diameters. This does not only require precise control during fiber production but also makes the fibers very sensitive to bend losses. As these bend losses are wavelength dependent, it will be challenging to keep them low for the Stokes wavelength while maintaining a small fiber NA. Alternatively, more complex fiber designs have to be used.

Quantum defect control

Since the refractive index grating responsible for TMI is caused by a dependence of the refractive index of the glass on the temperature, a solution would be to lower the heat load. This can be achieved by reducing the quantum defect by choosing wavelengths of Raman pump and Stokes that are close to each other, which is possible due to the broad gain region of Raman scattering. Unfortunately, this restricts the ability of the RFA to reach wavelengths outside the gain spectra of active doped fibers. However, it reduces the total heat load introduced into the fiber and, thereby, it is expected to increase the TMI threshold.

Thermal refractive index response

Instead of lowering the heat load, it is also possible to lower the sensitivity of the refractive index to temperature changes, i.e. to lower the thermo-optic coefficient in Equation 2.21. Following (Dragic et al., 2018), it is possible to reduce the factor of $\frac{\mathrm{d}n}{\mathrm{d}T}$ to zero and, thereby, create an *athermal fiber*. This would require co-doping the fiber with Boron or Phosphor at every region that experiences a temperature increase. Due to thermal conduction within the fiber, this region is larger than the fiber core. Producing such a large region can be impractical. An alternative would be not to aim for $\frac{\mathrm{d}n}{\mathrm{d}T} = 0$, but to choose a slightly higher factor, that is still lower than the $\frac{\mathrm{d}n}{\mathrm{d}T}$ of the surrounding silica. That way, the refractive index in the core would increase similar to the refractive index in the surrounding cladding, albeit experiencing a much higher heat load. Consequently, the refractive index difference between core and cladding

would not (strongly) increase and, thus, the fiber would show stable guiding conditions, i.e. a fiber that is single-mode in its cold state would remain single-mode under heat load. While the technique of tailoring the thermal refractive index response would require substantial fiber material research, it has a vast potential to improve the performance of high-power, single-mode fiber lasers. This also holds true for Raman fiber lasers, but it has to be noted that strong co-doping influences the Raman gain as the dopants vibrate differently (El Hamzaoui et al., 2015). Consequently, a fine tuning of the fiber parameters might be necessary to adapt to a gain curve different from the one depicted in Figure 2.3.

Active TMI mitigation

Lastly, one could consider active strategies to either mitigate the TMI within the fiber or to work with an unstable beam.

The latter would be done by deploying adaptive optics. Low power experiments show that such a technique is able to significantly increase the power in the bucket of a beam profile (Xie et al., 2019). However, due to the necessary computation time, this correction is currently too slow for TMI compensation. The reaction times would need to be shortened by 2 orders of magnitude, which seems unlikely in the near future.

Another option is given by an active TMI mitigation within the fiber, as proposed by (Stihler et al., 2018). These methods rely on the control of the phase shift between the refractive index grating and the mode interference pattern that are responsible for TMI. There are several methods to achieve this such as a pump modulation (Jauregui et al., 2018) or a dual-tone seeding (Möller et al., 2020a). While the last is not feasible in RFA, a pump modulation is. Since the phase shift between refractive index grating and mode interference pattern accumulates along the fiber length and since the fiber lengths required for RFA are much longer than the one studied in (Jauregui et al., 2018), a much smaller variation than the one presented in (Jauregui et al., 2018) might achieve a TMI suppression.

5.5 Conclusion

This chapter gave a review of the research on SRS causing TMI in active fibers. Beyond that, experimental evidence was given of the occurrence of SRS-induced TMI in passive fibers. To this end a high-power, core-pumped RFA was constructed and the emitted beam was analyzed in a spectrally selective manner with high temporal resolution, which led to the detection of TMI. Measurements with and without Stokes seed proofed that the instability was caused by SRS. Stability analysis of the system at two different points along the fiber allowed to identify the passive fiber as place of origin of the TMI. This effect observed here for the first time, is likely to become a strong performance limitation of high-power, single-mode RFAs in the near future. TMI already is a major limiting factor of high-power active fibers, as explained in (Zervas, 2019). The results presented in this chapter showed that it poses a similar threat to high-power RFA and, potentially, even to beam delivery fibers if SRS comes into play.

Therefore, a complete understanding of the process is necessary. A first step towards this goal was made by experimentally investigating the influence of the Stokes seed power and fiber length on the TMI threshold. The latter was determined by performing a modal decomposition of the output beam profile. These investigations validate previous theoretical predictions and imply that the total heat load along the fiber is the key parameter for SRS-induced TMI. This led to the discussion of several other influential parameters and strategies to mitigate SRS-induced TMI. Implementing these strategies will allow for kW-level RFA with excellent beam quality in the spectral region beyond 1.1 µm in the near future.

6 Conclusion and outlook

This thesis presented analytic, numerical and experimental investigations of SRS in high-power fiber laser systems. There are two major fields of applications where the insights gained from this thesis are helpful: High-power fiber laser systems where SRS is sought to be avoided and high-power Raman fiber amplifiers.

In solid-core fibers the Raman pump and the Stokes signal experience different group velocities and this thesis showed that the resulting walk-off has a strong influence on the SRS process even in continuous wave systems. An existing analytical walk-off model describing the single-pulse case could be expanded to describe the continuous case. Walk-off was found to explain the previously observed, but not understood relation of a lower Stokes content for a broader spectral width of the output coupler grating in high-power fiber oscillators. A broader spectrum corresponds to shorter temporal features which results in walk-off reducing the simultaneous presence of the Raman pump and the Stokes signal more effectively. Numerical simulations verify the influence of walk-off and the analytical model. The application domain of the latter was clarified. The analytical walk-off model was found to be in agreement with previously published experimental data showing a Stokes power decrease over several orders of magnitude with an increasing spectral width.

These insights are especially important for high-power cw fiber oscillators, that currently show an SRS-limited record output power of 5 kW at a wavelength of around 1 µm. As further improvement of the thermal properties of the FBGs in such oscillators can be expected, the precise knowledge of the influence of their spectral width will allow significantly reducing the Stokes content of these systems. As a consequence even higher output powers are within reach with monolithic fiber oscillators up to where transverse mode instability limits further scaling. A stable single-mode operation with mode-field

area of approximately 300 μm^2 at an output power of 6 kW and beyond should be possible in the near future.

The performance of high-power, single-mode RFAs has been studied as well. Experimental investigations showed that a multi-longitudinal mode Raman pump seed source is best suited for narrow-linewidth operation, because it prohibits spectral broadening of the Stokes signal induced by cross-phase modulation. The Stokes output power of the RFA could be increased up to 500 W.

Furthermore, experimental evidence of TMI caused by SRS was presented. Monitoring the stability of the system at several locations along the fiber enabled to locate the origin of the TMI within the passive fiber. To the best of my knowledge, this is the first time that the effect of TMI has been reported in a passive fiber. The TMI threshold was determined by carrying out a spectrally selective modal decomposition of the beam profiles measured with a high-speed camera. A systematic variation of the fiber length and Stokes seed power allowed to verify and expand previous theoretical predictions. A main result of these investigations is, that the TMI threshold occurs at the same extracted Stokes power, independently of the Stokes seed power and fiber length. This indicates that for a given passive fiber and launch condition, the Stokes power is the parameter to monitor when tailoring pump power and fiber length to remain below the TMI threshold. It became clear, that SRS-induced TMI poses a severe threat to the performance scaling of high-power RFAs.

However, there are several mitigation techniques of TMI viable, that are discussed in this thesis, such as single-mode guidance and an athermal fiber. Testing these strategies should be in the center of future research. While the fabrication of an athermal fiber promises a strong power scaling, it requires substantial research effort. Investigating the influence of fiber bending and the possibility to compensate pump intensity noise are simpler steps towards an improved performance of high-power RFAs. In the mid-term, the outlined TMI-mitigation strategies will allow kW-level (cascaded) RFA with excellent beam quality in the wavelength region between the emission bands of Yb and Er. These sources will allow for high-brightness in-band pumping of Er-doped fiber lasers, reducing the quantum defect in those systems and thereby scaling their attainable output power. High-power RFAs and Er-doped fiber lasers emitting in the "eye-safe" region beyond 1.4 µm will likely have a huge impact on many applications requiring open air transmission such as remote sensing, rangefinding and free-space optical communications.

Bibliography

AGRAWAL, Govind P., 2013. *Nonlinear Fiber Optics*. Elsevier. Available from DOI: 10.1016/B978-0-12-397023-7.00018-8.

BARRIO, R. A.; GALEENER, F. L.; MARTINEZ, E.; ELLIOTT, R. J., 1993. Regular ring dynamics in AX_2 tetrahedral glasses. *Physical Review B*. No. 48.21, pp. 15672–15689.

BEIER, Franz; HUPEL, Christian; KUHN, Stefan; HEIN, Sigrun; NOLD, Johannes; PROSKE, Fritz; SATTLER, Bettina; LIEM, Andreas; JAUREGUI, César; LIMPERT, Jens; HAARLAMMERT, Nicoletta; SCHREIBER, Thomas; EBERHARDT, Ramona; TÜNNERMANN, Andreas, 2017a. Single mode 4.3 kW output power from a diode-pumped Yb-doped fiber amplifier. *Optics Express*. Vol. 25, no. 13, pp. 14892–14899. Available from DOI: 10.1364/OE.25.014892.

BEIER, Franz; MÖLLER, Friedrich; SATTLER, Bettina; NOLD, Johannes; LIEM, Andreas; HUPEL, Christian; KUHN, Stefan; HEIN, Sigrun; HAARLAMMERT, Nicoletta; SCHREIBER, Thomas; EBERHARDT, Ramona; TÜNNERMANN, Andreas, 2018. Experimental investigations on the TMI thresholds of low-NA Yb-doped single-mode fibers. *Optics Letters*. Vol. 43, no. 6, pp. 1291–1294. Available from DOI: 10.1364/OL.43.001291.

BEIER, Franz; PLÖTNER, Marco; SATTLER, Bettina; STUTZKI, Fabian; WALBAUM, Till; LIEM, Andreas; HAARLAMMERT, Nicoletta; SCHREIBER, Thomas; EBERHARDT, Ramona; TÜNNERMANN, Andreas, 2017b. Measuring thermal load in fiber amplifiers in the presence of transversal mode instabilities. *Optics Letters*. Vol. 42, no. 21, pp. 4311–4314. Available from DOI: 10.1364/OL.42.004311.

BEYER, Eckhard; MAHRLE, Achim; LÜTKE, Matthias; STANDFUSS, Jens; BRÜCKNER, Frank, 2012. Innovations in high power fiber laser appli-

cations. In: *Fiber Lasers IX: Technology, Systems, and Applications*. SPIE, p. 823717. SPIE Proceedings. Available from DOI: 10.1117/12.910899.

BLOW, K. J.; WOOD, D., 1989. Theoretical description of transient stimulated Raman scattering in optical fibers. *IEEE Journal of Quantum Electronics*. No. 25, 12, pp. 2665–2673. Available from DOI: 10.1109/3.40655.

BOYD, Robert W., 2008. *Nonlinear optics*. 3. ed. Amsterdam: Elsevier/Academic Press. Available also from: http://site.ebrary.com/lib/alltitles/docDetail.action?docID=10258886.

BROCHU, G.; VILLENEUVE, A.; FAUCHER, M.; MORIN, M.; TRÉPANIER, F.; DIONNE, R., 2017. SRS modeling in high power CW fiber lasers for component optimization. *Proc. SPIE (LASE)*, 100850N. Available from DOI: 10.1117/12.2248336.

BROWN, D. C.; HOFFMAN, H. J., 2001. Thermal, stress, and thermo-optic effects in high average power double-clad silica fiber lasers. *IEEE Journal of Quantum Electronics*. Vol. 37, no. 2, pp. 207–217. Available from DOI: 10.1109/3.903070.

CAO, Ruiting; LIN, Xianfeng; CHEN, Yisha; CHENG, Yongshi; WANG, Yibo; XING, Yingbin; LI, Haiqing; YANG, Luyun; CHEN, Gui; LI, Jinyan, 2019. 532 nm pump induced photo-darkening inhibition and photo-bleaching in high power Yb-doped fiber amplifiers. *Optics Express*. Vol. 27, no. 19, pp. 26523–26531. Available from DOI: 10.1364/OE.27.026523.

CHEN, Yizhu; YAO, Tianfu; HUANG, Liangjin; XIAO, Hu; LENG, Jinyong; ZHOU, Pu, 2020a. 2 kW high-efficiency Raman fiber amplifier based on passive fiber with dynamic analysis on beam cleanup and fluctuation. *Optics Express*. Vol. 28, no. 3, pp. 3495–3504. Available from DOI: 10.1364/OE.383683.

CHEN, Yizhu; YAO, Tianfu; XIAO, Hu; LENG, Jinyong; ZHOU, Pu, 2020b. High-power cladding pumped Raman fiber amplifier with a record beam quality. *Optics Letters*. Vol. 45, no. 8, pp. 2367–2370. Available from DOI: 10.1364/OL.388297.

CHRISTENSEN, Erik N.; KOEFOED, Jacob G.; FRIIS, Søren M. M.; CASTANEDA, Mario A. Usuga; ROTTWITT, Karsten, 2016. Experimental characterization of Raman overlaps between mode-groups. *Scientific reports*. Vol. 6, p. 34693. Available from DOI: 10.1038/srep34693.

CHRISTODOULIDES, D. N.; JOSEPH, R. I., 1989. Theory of stimulated Raman scattering in optical fibers in the pulse walkoff regime. *IEEE Journal of Quantum Electronics*, pp. 273–279.

DAVIS, M. K.; DIGONNET, Michel J.; PANTELL, Richard H., 1998. Thermal Effects in Doped Fibers. *Journal of Lightwave Technology*. Vol. 16, no. 6, p. 1013.

DAWSON, Jay W.; MESSERLY, Michael J.; BEACH, Raymond J.; SHVERDIN, Miroslav Y.; STAPPAERTS, Eddy A.; SRIDHARAN, Arun K.; PAX, Paul H.; HEEBNER, John E.; SIDERS, Craig W.; BARTY, C. P. J., 2008. Analysis of the scalability of diffraction-limited fiber lasers and amplifiers to high average power. *Optics Express*. Vol. 16, no. 17, pp. 13240–13266. Available from DOI: 10.1364/oe.16.013240.

DONG, Liang, 2013. Stimulated thermal Rayleigh scattering in optical fibers. *Optics Express*. Vol. 21, no. 3, pp. 2642–2656. Available from DOI: 10.1364/OE.21.002642.

DONG, Liang, 2016. Thermal lensing in optical fibers. *Optics Express*. Vol. 24, no. 17, pp. 19841–19852. Available from DOI: 10.1364/OE.24.019841.

DONG, Liang; SAMSON, Bryce, 2017. *Fiber lasers: Basics, technology, and applications*. Boca Raton, FL: CRC Press.

DRAGIC, Peter D.; CAVILLON, Maxime; BALLATO, Arthur; BALLATO, John, 2018. A unified materials approach to mitigating optical nonlinearities in optical fiber. II. B. The optical fiber, material additivity and the nonlinear coefficients. *International Journal of Applied Glass Science*. Vol. 9, no. 3, pp. 307–318. Available from DOI: 10.1111/ijag.12329.

EIDAM, Tino; WIRTH, Christian; JAUREGUI, César; STUTZKI, Fabian; JANSEN, Florian; OTTO, Hans-Jürgen; SCHMIDT, Oliver; SCHREIBER, Thomas; LIMPERT, Jens; TÜNNERMANN, Andreas, 2011. Experimental observations of the threshold-like onset of mode instabilities in high power fiber amplifiers. *Optics Express*. Vol. 19, no. 14, pp. 13218–13224. Available from DOI: 10.1364/OE.19.013218.

EL HAMZAOUI, Hicham; BOUAZAOUI, Mohamed; CAPOEN, Bruno, 2015. Raman investigation of germanium- and phosphorus-doping effects on the structure of sol–gel silica-based optical fiber preforms. *Journal of Molecular Structure*. Vol. 1099, pp. 77–82. Available from DOI: 10.1016/j.molstruc.2015.06.061.

ENDERLEIN, Martin, 2020. SodiumStar – The sodium guide star laser by TOPTICA Projects GmbH. *SPIE Exhibition Product Demonstrations*, AS20EX0F. Available from DOI: 10.1117/12.2588664.

ENGHOLM, Magnus; NORIN, Lars, 2008. Reduction of photodarkening in Yb/Al-doped fiber lasers. In: BROENG, Jes; HEADLEY III, Clifford (eds.). *Fiber Lasers V: Technology, Systems, and Applications*. SPIE, 68731E. SPIE Proceedings. Available from DOI: 10.1117/12.763218.

FANG, Qiang; LI, Jinhui; SHI, Wei; QIN, Yuguo; XU, Yang; MENG, Xiangjie; NORWOOD, Robert A.; PEYGHAMBARIAN, Nasser, 2017. 5 kW Near-Diffraction-Limited and 8 kW High-Brightness Monolithic Continuous Wave Fiber Lasers Directly Pumped by Laser Diodes. *IEEE Photonics Journal*. Vol. 9, no. 5, pp. 1–7. Available from DOI: 10.1109/JPHOT.2017.2744803.

FELICE, Domenico, 2016. *A Study of a Nonlinear Schrödinger Equation for Optical Fibers*.

FENG, Yan; TAYLOR, Luke R.; CALIA, Domenico Bonaccini, 2009. 25 W Raman-fiber-amplifier-based 589 nm laser for laser guide star. *Optics Express*. Vol. 17, no. 21, pp. 19021–19026. Available from DOI: 10.1364/OE.17.019021.

FIBERDESK, 2021. Available also from: www.fiberdesk.com.

FINI, John M.; MERMELSTEIN, Marc D.; YAN, M. F.; BISE, r. T.; YABLON, Andrew D.; WISK, P. W.; ANDREJCO, M. J., 2006. Distributed suppression of stimulated Raman scattering in an Yb-doped filter-fiber amplifier. *Optics Letters*. Vol. 31, no. 17, pp. 2550–2552. Available from DOI: 10.1364/OL.31.002550.

FLUDGER, C. R. S.; HANDEREK, V.; MEARS, R. J., 2001. Pump to Signal RIN Transfer in Raman Fiber Amplifiers. *Journal of Lightwave Technology*. No. 19.8, pp. 1140–1148.

FROSZ, Michael, 2010. Validation of input-noise model for simulations of supercontinuum generation and rogue waves. *Optics Express*. Vol. 51, no. 5, pp. 14778–14787.

FU, Yuqing; FENG, Guoying; ZHANG, Dayong; CHEN, Jianguo; ZHOU, Shouhuan, 2010. Beam quality factor of mixed modes emerging from a multimode step-index fiber. *Optik*. Vol. 121, no. 5, pp. 452–456. Available from DOI: 10.1016/j.ijleo.2008.08.003.

GAIDA, Christian; GEBHARDT, Martin; HEUERMANN, Tobias; WANG, Ziyao; JAUREGUI, Cesar; LIMPERT, Jens, 2021. Transverse mode instability and thermal effects in thulium-doped fiber amplifiers under high thermal loads. *Optics Express*. Vol. 29, no. 10, pp. 14963–14973. Available from DOI: 10.1364/OE.421954.

GALEENER, F. L.; GEISSBERGER, A. E., 1983. Vibrational dynamics in 30Si -substituted vitreous SiO2. *Physical Review B*. Vol. 27, no. 10, pp. 6199–6204. Available from DOI: 10.1103/PhysRevB.27.6199.

GALEENER, F. L.; MIKKELSEN, J. C., 1981. Vibrational dynamics in 18O - substituted vitreous SiO2. *Physical Review B*. Vol. 23, no. 10, pp. 5527–5530. Available from DOI: 10.1103/PhysRevB.23.5527.

GIERSCHKE, Philipp; JAUREGUI, César; GOTTSCHALL, Thomas; LIMPERT, Jens, 2019. Relative amplitude noise transfer function of an Yb3+-doped fiber amplifier chain. *Optics Express*. Vol. 27, no. 12, pp. 17041–17050. Available from DOI: 10.1364/OE.27.017041.

GLICK, Yaakov; SHAMIR, Yariv; AVIEL, Matitya; SINTOV, Yoav; GOLDRING, Sharone; SHAFIR, Noam; PEARL, Shaul, 2018. 1.2 kW clad pumped Raman all-passive-fiber laser with brightness enhancement. *Optics Letters*. Vol. 43, no. 19, pp. 4755–4758. Available from DOI: 10.1364/OL.43.004755.

HAARLAMMERT, Nicoletta; REKAS, M.; VRIES, Oliver de; KLINER, A.; LIEM, Andreas; SCHREIBER, Thomas; EBERHARDT, Ramona; TÜNNERMANN, Andreas, 2013. Polarization dependent nonlinear limitations in continuous-wave high power fiber amplifiers. In: HENDOW, Sami T. (ed.). *Fiber Lasers X: Technology, Systems, and Applications*. SPIE, 86012W. SPIE Proceedings. Available from DOI: 10.1117/12.2004362.

HANSEN, Kristian Rymann; ALKESKJOLD, Thomas Tanggaard; BROENG, Jes; LÆGSGAARD, Jesper, 2011. Thermo-optical effects in high-power ytterbium-doped fiber amplifiers. *Optics Express*. Vol. 19, no. 24, pp. 23965–23980. Available from DOI: 10.1364/OE.19.023965.

HANSEN, Kristian Rymann; ALKESKJOLD, Thomas Tanggaard; BROENG, Jes; LÆGSGAARD, Jesper, 2012. Thermally induced mode coupling in rare-earth doped fiber amplifiers. *Optics Letters*. Vol. 37, no. 12, pp. 2382–2384. Available from DOI: 10.1364/OL.37.002382.

HANSEN, Kristian Rymann; ALKESKJOLD, Thomas Tanggaard; BROENG, Jes; LÆGSGAARD, Jesper, 2013. Theoretical analysis of mode instability in high-power fiber amplifiers. *Optics Express*. Vol. 21, no. 2, pp. 1944–1971. Available from DOI: 10.1364/OE.21.001944.

HARISH, Achar Vasant; NILSSON, Johan, 2018. Optimization of Phase Modulation Formats for Suppression of Stimulated Brillouin Scattering in Optical Fibers. *IEEE Journal of Selected Topics in Quantum Electronics*. Vol. 24, no. 3, pp. 1–10. Available from DOI: 10.1109/JSTQE.2017.2753041.

HECHT, Jeff, 2008. PHOTONIC FRONTIERS: EYE-SAFE LASERS-Retina-safe wavelengths benefit open-air applications. *Laser Focus World*. No. 44.

HECK, Maximilian; KRÄMER, Ria G.; RICHTER, Daniel; GOEBEL, Thorsten A.; MATZDORF, Christian; BOCK, Victor; LIEM, Andreas; SCHREIBER, Thomas; TÜNNERMANN, Andreas; NOLTE, Stefan, 2018. Mitigation of stimulated Raman scattering in high power fiber lasers using transmission gratings, p. 53. Available from DOI: 10.1117/12.2289511.

HEJAZ, Kamran; SHAYGANMANESH, Mahdi; REZAEI-NASIRABAD, Reza; ROOHFOROUZ, Ali; AZIZI, S.; ABEDINAJAFI, Ali; VATANI, Vahid, 2017. Modal instability induced by stimulated Raman scattering in high-power Yb-doped fiber amplifiers. *Optics Letters*. Vol. 42, no. 24, pp. 5274–5277. Available from DOI: 10.1364/OL.42.005274.

HOLLENBECK, Dawn; CANTRELL, Cyrus D., 2002. Multiple-vibrational-mode model for fiber-optic Raman gain spectrum and response function. *Journal of the Optical Society of America B*. Vol. 19, no. 12, pp. 2886–2892. Available from DOI: 10.1364/JOSAB.19.002886.

HUTCHINGS, D. C.; SHEIK-BAHAE, M.; HAGAN, D. J.; VAN STRYLAND, E. W., 1992. Kramers-Krönig relations in nonlinear optics. *Optical and Quantum Electronics*. No. 24, pp. 1–30.

JANSEN, Florian; NODOP, Dirk; JAUREGUI, César; LIMPERT, Jens; TÜNNERMANN, Andreas, 2009. Modeling the inhibition of stimulated Raman scattering in passive and active fibers by lumped spectral filters in high power fiber laser systems. *Optics Express*. Vol. 17, no. 18, pp. 16255–16265. Available from DOI: 10.1364/OE.17.016255.

JANSEN, Florian; NODOP, Dirk; JAUREGUI, César; LIMPERT, Jens; TÜNNERMANN, Andreas, 2010. Suppression of stimulated Raman scattering in high-power fiber laser systems by lumped spectral filters. In: TANKALA, Kanishka (ed.). *SPIE LASE*. SPIE, p. 75802I. SPIE Proceedings. Available from DOI: 10.1117/12.842104.

JANSEN, Florian; STUTZKI, Fabian; OTTO, Hans-Jürgen; EIDAM, Tino; LIEM, Andreas; JAUREGUI, Cesar; LIMPERT, Jens; TÜNNERMANN, Andreas, 2012. Thermally induced waveguide changes in active fibers. *Optics Express*. Vol. 20, no. 4, pp. 3997–4008. Available from DOI: 10.1364/OE.20.003997.

JAUREGUI, César; EIDAM, Tino; OTTO, Hans-Jürgen; STUTZKI, Fabian; JANSEN, Florian; LIMPERT, Jens; TÜNNERMANN, Andreas, 2012. Temperature-induced index gratings and their impact on mode instabilities in high-power fiber laser systems. *Optics Express*. Vol. 20, no. 1, pp. 440–451. Available from DOI: 10.1364/OE.20.000440.

JAUREGUI, César; OTTO, Hans-Jürgen; BREITKOPF, Sven; LIMPERT, Jens; TÜNNERMANN, Andreas, 2016. Optimizing high-power Yb-doped fiber amplifier systems in the presence of transverse mode instabilities. *Optics Express*. Vol. 24, no. 8, pp. 7879–7892. Available from DOI: 10.1364/OE.24.007879.

JAUREGUI, César; OTTO, Hans-Jürgen; STUTZKI, Fabian; LIMPERT, Jens; TÜNNERMANN, Andreas, 2015. Simplified modelling the mode instability threshold of high power fiber amplifiers in the presence of photodarkening. *Optics Express*. Vol. 23, no. 16, pp. 20203–20218. Available from DOI: 10.1364/OE.23.020203.

JAUREGUI, César; STIHLER, Christoph; KHOLAIF, Sobhy E.; TU, Yiming; LIMPERT, Jens, 05.03.2021. *Mitigation of transverse mode instability in polarization maintaining, high-power fiber amplifiers*. Available from DOI: 10.1117/12.2577635.

JAUREGUI, César; STIHLER, Christoph; LIMPERT, Jens, 2020a. Transverse mode instability. *Advances in Optics and Photonics*. Vol. 12, no. 2, pp. 429–484. Available from DOI: 10.1364/AOP.385184.

JAUREGUI, César; STIHLER, Christoph; TU, Yiming; KHOLAIF, Sobhy E.; LIMPERT, Jens, 2020b. Mitigation of transverse mode instability with travel-

ling waves in high-power fiber amplifiers. *Proc. SPIE 11260*, p. 46. Available from DOI: 10.1117/12.2543383.

JAUREGUI, César; STIHLER, Christoph; TÜNNERMANN, Andreas; LIMPERT, Jens, 2018. Pump-modulation-induced beam stabilization in high-power fiber laser systems above the mode instability threshold. *Optics Express*. Vol. 26, no. 8, pp. 10691–10704. Available from DOI: 10.1364/OE.26.010691.

JETSCHKE, Sylvia; UNGER, Sonja; LEICH, Martin; KIRCHHOF, Johannes, 2012. Photodarkening kinetics as a function of Yb concentration and the role of Al codoping. *Appl. Opt.* Vol. 51, no. 32, pp. 7758–7764. Available from DOI: 10.1364/AO.51.007758.

JOHANSEN, Mette Marie; LAURILA, Marko; MAACK, Martin D.; NOORDEGRAAF, Danny; JAKOBSEN, Christian; ALKESKJOLD, Thomas Tanggaard; LÆGSGAARD, Jesper, 2013. Frequency resolved transverse mode instability in rod fiber amplifiers. *Optics Express*. Vol. 21, no. 19, pp. 21847–21856. Available from DOI: 10.1364/OE.21.021847.

KABACIŃSKI, Piotr; KARDAŚ, Tomasz M.; STEPANENKO, Yuriy; RADZEWICZ, Czesław, 2019. Nonlinear refractive index measurement by SPM-induced phase regression. *Optics Express*. Vol. 27, no. 8, pp. 11018–11028. Available from DOI: 10.1364/OE.27.011018.

KALAMPOUNIAS, Angelos, 2011. IR and Raman spectroscopic studies of sol–gel derived alkaline-earth silicate glasses. *Bulletin of Materials Science*. Vol. 34, no. 2, pp. 299–303. Available from DOI: 10.1007/s12034-011-0064-x.

KIM, J.; DUPRIEZ, P.; CODEMARD, Christophe A.; NILSSON, Johan; SAHU, Jayanta K., 2006. Suppression of stimulated Raman scattering in a high power Yb-doped fiber amplifier using a W-type core with fundamental mode cut-off. *Optics Express*. Vol. 14, no. 12, pp. 5103–5113. Available from DOI: 10.1364/OE.14.005103.

KIRCHHOF, Johannes; UNGER, Sonja; SCHWUCHOW, Anka; JETSCHKE, Sylvia; KNAPPE, Bruno, 2005. Dopant interactions in high-power laser fibers. In: JIANG, Shibin; DIGONNET, Michel J. (eds.). *Optical Components and Materials II*. SPIE, p. 261. SPIE Proceedings. Available from DOI: 10.1117/12.590021.

KOBYAKOV, Andrey; SAUER, Michael; CHOWDHURY, Dipak, 2010. Stimulated Brillouin scattering in optical fibers. *Advances in Optics and Photonics*. Vol. 2, no. 1, pp. 1–59. Available from DOI: 10.1364/AOP.2.000001.

KOPONEN, Joona J.; SÖDERLUND, Mikko J.; HOFFMAN, Hanna J.; TAMMELA, Simo K. T., 2006. Measuring photodarkening from single-mode ytterbium doped silica fibers. *Optics Express*. Vol. 14, no. 24, pp. 11539–11544. Available from DOI: 10.1364/oe.14.011539.

KOREPANOV, Vitaly I., 2020. Phonon propagation scale and nanoscale order in vitreous silica from Raman spectroscopy. *Journal of physics. Condensed matter : an Institute of Physics journal*. Vol. 32, no. 5, p. 055901. Available from DOI: 10.1088/1361-648X/ab4f23.

KRÄMER, Ria G.; MATZDORF, Christian; LIEM, Andreas; BOCK, Victor; MIDDENTS, Wilko; GOEBEL, Thorsten A.; HECK, Maximilian; RICHTER, Daniel; SCHREIBER, Thomas; TÜNNERMANN, Andreas; NOLTE, Stefan, 2019. Femtosecond written fiber Bragg gratings in ytterbium-doped fibers for fiber lasers in the kilowatt regime. *Optics Letters*. Vol. 44, no. 4, pp. 723–726. Available from DOI: 10.1364/OL.44.000723.

KUHN, Stefan; HEIN, S.; HUPEL, C.; NOLD, Johannes; HAARLAMMERT, Nicoletta; SCHREIBER, Thomas; EBERHARDT, Ramona; TÜNNERMANN, Andreas, 2018. Modelling the refractive index behavior of Al,P-doped SiO 2 , fabricated by means of all-solution doping, in the vicinity of Al:P = 1:1. *Optical Materials Express*. Vol. 8, no. 5, pp. 1328–1340. Available from DOI: 10.1364/OME.8.001328.

LAI, Wenchang; MA, Pengfei; LIU, Wei; HUANG, Long; LI, Can; MA, Yanxing; ZHOU, Pu, 2020. 550 W single frequency fiber amplifiers emitting at 1030 nm based on a tapered Yb-doped fiber. *Optics Express*. Vol. 28, no. 14, pp. 20908–20919. Available from DOI: 10.1364/OE.395619.

LANGNER, Andreas; SUCH, Mario; SCHÖTZ, Gerhard; GRIMM, Stephan; JUST, Florian; LEICH, Martin; MÜHLIG, Christian; KOBELKE, Jens; SCHWUCHOW, Anka; MEHL, Oliver; STRAUCH, Olaf; NIEDRIG, Roman; WEDEL, Björn; REHMANN, Georg; KRAUSE, Volker, 2011. New developments in high power fiber lasers based on alternative materials. In: DAWSON, Jay W. (ed.). *Fiber Lasers VIII: Technology, Systems,*

and Applications. SPIE, 79141U. SPIE Proceedings. Available from DOI: 10.1117/12.876978.

LEE, Junsu; LEE, Kwang Hyun; JEONG, Hwanseong; PARK, Minkyu; SEUNG, Ji Hoon; LEE, Jung Hwan, 2019. 2.05 kW all-fiber high-beam-quality fiber amplifier with stimulated Brillouin scattering suppression incorporating a narrow-linewidth fiber-Bragg-grating-stabilized laser diode seed source. *Appl. Opt.* Vol. 58, no. 23, pp. 6251–6256. Available from DOI: 10.1364/AO.58.006251.

LEPROUX, P.; FÉVRIER, S.; DOYA, V.; ROY, P.; PAGNOUX, D., 2001. Modeling and Optimization of Double-Clad Fiber Amplifiers Using Chaotic Propagation of the Pump. *Optical Fiber Technology*. Vol. 7, no. 4, pp. 324–339. Available from DOI: 10.1006/ofte.2001.0361.

LI, Tenglong; KE, Weiwei; MA, Yi; SUN, Yinhong; GAO, Qingsong, 2019. Suppression of stimulated Raman scattering in a high-power fiber amplifier by inserting long transmission fibers in a seed laser. *Journal of the Optical Society of America B*. Vol. 36, no. 6, pp. 1457–1465. Available from DOI: 10.1364/JOSAB.36.001457.

LI, Tenglong; ZHA, Congwen; SUN, Yinhong; MA, Yi; KE, Weiwei; PENG, Wanjing, 2018. 3.5 kW bidirectionally pumped narrow-linewidth fiber amplifier seeded by white-noise-source phase-modulated laser. *Laser Physics*. Vol. 28, no. 10, p. 105101. Available from DOI: 10.1088/1555-6611/aace37.

LI, Yang; LI, Tenglong; PENG, Wanjing; SU, Hua; WANG, Xiaojun, 2017. Narrow Spectrum Kilowatt-Level MOPA Seeded By Yb-Doped Random Fiber Laser. *IEEE Photonics Technology Letters*. Vol. 29, no. 21, pp. 1844–1847. Available from DOI: 10.1109/LPT.2017.2753323.

LI, Zebiao; JING, Feng; LI, Chengyu; LIU, Yu; LUO, Qiang; LIN, Honghuan; HUANG, Zhihua; XU, Shanhui; YANG, Zhongmin; WANG, Jianjun, 2018. Impact of Stimulated Raman Scattering on the Transverse Mode Instability Threshold. *IEEE Photonics Journal*. Vol. 10, no. 3, pp. 1–9. Available from DOI: 10.1109/JPHOT.2018.2842467.

LIN, Q.; AGRAWAL, Govind P., 2006. Raman response function for silica fibers. *Optics Letters*. Vol. 31, no. 21, pp. 3086–3088. Available from DOI: 10.1364/OL.31.003086.

LIN, W.; ROCHETTE, M., 2018. Raman Suppression Using Chirp-Moire Fiber Bragg Grating in High-Power Fiber Lasers. *2018 Photonics North*.

LIU, Wei; MA, Pengfei; LV, Haibin; XU, Jiangmin; ZHOU, Pu; JIANG, Zongfu, 2016. General analysis of SRS-limited high-power fiber lasers and design strategy. *Optics Express*. Vol. 24, no. 23, pp. 26715–26721. Available from DOI: 10.1364/OE.24.026715.

LIU, Wei; MA, Pengfei; SHI, Chen; ZHOU, Pu; JIANG, Zongfu, 2018. Theoretical analysis of the SRS-induced mode distortion in large-mode area fiber amplifiers. *Optics Express*. Vol. 26, no. 12, pp. 15793–15803. Available from DOI: 10.1364/OE.26.015793.

LIU, Wei; MA, Pengfei; ZHOU, Pu; JIANG, Zongfu, 2017. Optimization for the fiber laser source through its temporal and spectral characteristics. *Proc. SPIE 10436, High-Power Lasers: Technology and Systems, Platforms, and Effects*, 104360O. Available from DOI: 10.1117/12.2277694.

MA, Pengfei; MIAO, Yu; LIU, Wei; MENG, Daren; ZHOU, Pu, 2020. Kilowatt-level ytterbium-Raman fiber amplifier with a narrow-linewidth and near-diffraction-limited beam quality. *Optics Letters*. Vol. 45, no. 7, pp. 1974–1977. Available from DOI: 10.1364/OL.387151.

MAFI, Arash, 2020. Temperature variation across an optical fiber laser: Why it is almost always small. *Journal of the Optical Society of America B*. Available from DOI: 10.1364/JOSAB.390935.

MISHCHIK, Konstantin, 2012. *Ultrafast laser-induced modification of optical glasses: a spectroscopy insight into the microscopic mechanisms*.

MITSCHKE, Fedor Manuel, 2005. *Glasfasern: Physik und Technologie*. 1. Aufl. Heidelberg: Elsevier Spektrum Akad. Verl. Available also from: http://deposit.dnb.de/cgi-bin/dokserv?id=2652185&prov=M&dok_var=1&dok_ext=htm.

MÖLLER, Friedrich; DISTLER, Victor; SCHREIBER, Thomas; EBERHARDT, Ramona; TÜNNERMANN, Andreas, 2020a. Manipulating the heat load distribution by laser gain competition in TMI-limited fiber amplifiers. *Proc. SPIE 11260*, Fiber Lasers XVII: Technology and Systems, 45. Available from DOI: 10.1117/12.2545951.

MÖLLER, Friedrich; DISTLER, Victor; STRECKER, Maximilian; WALBAUM, Till; SCHREIBER, Thomas, 2021. Backward transverse mode instability? *Proc. SPIE (LASE)*. No. 11665, p. 116650X.

MÖLLER, Friedrich; DISTLER, Victor; WALBAUM, Till; HAARLAMMERT, Nicoletta; NOLD, Johannes; SCHREIBER, Thomas; UNGER, Sonja; REICHEL, V.; KOBELKE, Jens; BIERLICH, J.; SCHWUCHOW, Anka; ESCHRICH, T.; LEICH, M.; WONDRACZEK, K.; TÜNNERMANN, Andreas, 2020b. Influence of pedestal diameter on mode instabilities in Yb/Ce/Al-doped fibers. *Optics Express*. Vol. 28, no. 22, pp. 33456–33474. Available from DOI: 10.1364/OE.403460.

MÖLLER, Friedrich; KRÄMER, Ria G.; C. MATZDORF; S. NOLTE; STRECKER, Maximilian; STUTZKI, Fabian; PLÖTNER, Marco; BOCK, Victor; SCHREIBER, Thomas; TÜNNERMANN, Andreas, 2018. Comparison Between Bidirectional Pumped Yb-doped All-fiber Single-mode Amplifier and Oscillator Setup up to a Power Level of 5 kW. *Laser Congress 2018 (ASSL), OSA Technical Digest*, paper AM2A.3.

MÖLLER, Friedrich; KRÄMER, Ria G.; MATZDORF, Christian; STRECKER, Maximilian; PLÖTNER, Marco; STUTZKI, Fabian; WALBAUM, Till; SCHREIBER, Thomas; EBERHARDT, Ramona; NOLTE, Stefan; TÜNNERMANN, Andreas, 2019. Multi-kW performance analysis of Yb-doped monolithic single-mode amplifier and oscillator setup. *Proc. SPIE 10897*, p. 12. Available from DOI: 10.1117/12.2509348.

NADERI, Shadi; DAJANI, Iyad; GROSEK, Jacob; MADDEN, Timothy, 2016. Theoretical and numerical treatment of modal instability in high-power core and cladding-pumped Raman fiber amplifiers. *Optics Express*. Vol. 24, no. 15, pp. 16550–16565. Available from DOI: 10.1364/OE.24.016550.

NICHOLSON, Jeffrey W.; YAN, M. F.; WISK, P.; FLEMING, J.; DIMARCELLO, F.; MONBERG, E.; TAUNAY, T.; HEADLEY, C.; DIGIOVANNI, D. J., 2010. Raman fiber laser with 81 W output power at 1480 nm. *Optics Letters*. Vol. 35, no. 18, pp. 3069–3071. Available from DOI: 10.1364/OL.35.003069.

NODOP, Dirk; JAUREGUI, César; JANSEN, F.; LIMPERT, Jens; TÜNNERMANN, Andreas, 2010. Suppression of stimulated Raman scattering employing long period gratings in double-clad fiber amplifiers. *Optics Letters*. Vol. 35, no. 17, pp. 2982–2984. Available from DOI: 10.1364/OL.35.002982.

OTTO, Hans-Jürgen; STUTZKI, Fabian; JANSEN, Florian; EIDAM, Tino; JAUREGUI, César; LIMPERT, Jens; TÜNNERMANN, Andreas, 2012. Temporal dynamics of mode instabilities in high-power fiber lasers and amplifiers. *Optics Express*. Vol. 2012, no. 14, pp. 15710–15722.

PLÖTNER, Marco; BOCK, Victor; SCHULTZE, Tim; BEIER, Franz; SCHREIBER, Thomas; EBERHARDT, Ramona; TÜNNERMANN, Andreas, 2017. High power sub-ps pulse generation by compression of a frequency comb obtained by a nonlinear broadened two colored seed. *Optics Express*. Vol. 25, no. 14, pp. 16476–16483. Available from DOI: 10.1364/OE.25.016476.

POPP, Alexandra; DISTLER, Victor; JAKSCH, Kevin; SEDLMEIR, Florian; MÜLLER, Christian R.; HAARLAMMERT, Nicoletta; SCHREIBER, Thomas; MARQUARDT, Christoph; TÜNNERMANN, Andreas; LEUCHS, Gerd, 2020. Quantum-limited measurements of intensity noise levels in Yb-doped fiber amplifiers. *Applied Physics B*. Vol. 126, no. 8, pp. 1–7. Available from DOI: 10.1007/s00340-020-07476-7.

RAMACHANDRAN, Siddharth; WANG, Zhiyong; YAN, Man, 2002. Bandwidth control of long-period grating-based mode converters in few-mode fibers. *Optics Letters*. Vol. 27, no. 9, pp. 698–700. Available from DOI: 10.1364/ol.27.000698.

ROCHA, A. C. P.; SILVA, J. R.; LIMA, S. M.; NUNES, L. A. O.; ANDRADE, L. H. C., 2016. Measurements of refractive indices and thermo-optical coefficients using a white-light Michelson interferometer. *Appl. Opt.* Vol. 55, no. 24, pp. 6639–6643. Available from DOI: 10.1364/AO.55.006639.

RUNCORN, T. H.; MURRAY, R. T.; KELLEHER, E. J. R.; POPOV, S. V.; TAYLOR, J. R., 2015. Duration-tunable picosecond source at 560 nm with watt-level average power. *Optics Letters*. Vol. 40, no. 13, pp. 3085–3088. Available from DOI: 10.1364/OL.40.003085.

SCARNERA, V.; GHIRINGHELLI, F.; MALINOWSKI, A.; CODEMARD, C. A.; DURKIN, M. K.; ZERVAS, Michalis N., 2019. Modal instabilities in high power fiber laser oscillators. *Optics Express*. Vol. 27, no. 4, pp. 4386–4403. Available from DOI: 10.1364/OE.27.004386.

SCHREIBER, Thomas; LIEM, Andreas; FREIER, E.; MATZDORF, Christian; EBERHARDT, Ramona; JAUREGUI, César; LIMPERT, Jens; TÜNNERMANN, Andreas, 2014. Analysis of stimulated Raman scattering in cw

kW fiber oscillators. *Proc. SPIE (LASE)*, 89611T. Available from DOI: 10.1117/12.2039869.

SIEGMAN, A. E., 1998. How to (Maybe) Measure Laser Beam Quality. *DPSS (Diode Pumped Solid State) Lasers: Applications and Issues*, OSA Trends in Optics and Photonics (Optical Society of America, 1998), paper MQ.

SMITH, Arlee V.; SMITH, Jesse J., 2011. Mode instability in high power fiber amplifiers. *Optics Express*. Vol. 19, no. 11, pp. 10180–10192. Available from DOI: 10.1364/OE.19.010180.

SMITH, Arlee V.; SMITH, Jesse J., 2016. Mode instability thresholds for Tm-doped fiber amplifiers pumped at 790 nm. *Optics Express*. Vol. 24, no. 2, pp. 975–992. Available from DOI: 10.1364/OE.24.000975.

SMITH, R. G., 1972. Optical Power Handling Capacity of Low Loss Optical Fibers as Determined by Stimulated Raman and Brillouin Scattering. *Appl. Opt.* No. 11, 11.

SOLLER, B.; GIFFORD, D.; WOLFE, M.; FROGGATT, M., 2005. High resolution optical frequency domain reflectometry for characterization of components and assemblies. *Optics Express*. No. 13.2, pp. 666–674.

STIHLER, Christoph, 2020. *Transverse mode instability: Insights into modal energy transfer in high-power fiber lasers*. Dissertation, Friedrich-Schiller-Universität Jena.

STIHLER, Christoph; JAUREGUI, César; KHOLAIF, Sobhy E.; LIMPERT, Jens, 2020. Intensity noise as a driver for transverse mode instability in fiber amplifiers. *PhotoniX*. Vol. 1, no. 1, pp. 1–17. Available from DOI: 10.1186/s43074-020-00008-8.

STIHLER, Christoph; JAUREGUI, César; TÜNNERMANN, Andreas; LIMPERT, Jens, 2018. Modal energy transfer by thermally induced refractive index gratings in Yb-doped fibers. *Light: Science & Applications*. Vol. 7, no. 1, pp. 1–12. Available from DOI: 10.1038/s41377-018-0061-6.

STOLEN, R., 1979. Polarization effects in fiber Raman and Brillouin lasers. *IEEE Journal of Quantum Electronics*. Vol. 15, no. 10, pp. 1157–1160. Available from DOI: 10.1109/JQE.1979.1069913.

STOLEN, R.; LIN, Chinlon, 1978. Self-phase-modulation in silica optical fibers. *Physical Review A*. Vol. 17, no. 4, pp. 1448–1453. Available from DOI: 10.1103/PhysRevA.17.1448.

STOLEN, R.; TOMLINSON, W. J.; HAUS, H. A.; GORDON, J. P., 1989. Raman response function of silica-core fibers. *Journal of the Optical Society of America B*. Vol. 6, no. 6, pp. 1159–1166. Available from DOI: 10.1364/JOSAB.6.001159.

STUTZKI, Fabian; OTTO, Hans-Jürgen; JANSEN, Florian; GAIDA, Christian; JAUREGUI, César; LIMPERT, Jens; TÜNNERMANN, Andreas, 2011. High-speed modal decomposition of mode instabilities in high-power fiber lasers. *Optics Letters*. No. 36, pp. 4572–4574.

SUPRADEEPA, V. R.; FENG, Yan; NICHOLSON, Jeffrey W., 2017. Raman fiber lasers. *Journal of Optics*. Vol. 19, no. 2, p. 023001. Available from DOI: 10.1088/2040-8986/19/2/023001.

SURIN, A. A.; BORISENKO, T. E.; LARIN, S. V., 2016. Generation of 14 W at 589 nm by frequency doubling of high-power CW linearly polarized Raman fiber laser radiation in MgO:sPPLT crystal. *Optics Letters*. Vol. 41, no. 11, pp. 2644–2647. Available from DOI: 10.1364/OL.41.002644.

ŠUŠNJAR, Peter; AGREŽ, Vid; PETKOVŠEK, Rok, 2018. Photodarkening as a heat source in ytterbium doped fiber amplifiers. *Optics Express*. Vol. 26, no. 5, pp. 6420–6426. Available from DOI: 10.1364/OE.26.006420.

TAO, Rumao; MA, Pengfei; WANG, Xiaolin; ZHOU, Pu; LIU, Zejin, 2015a. 1.3 kW monolithic linearly polarized single-mode master oscillator power amplifier and strategies for mitigating mode instabilities. *Photonics Research*. Vol. 3, no. 3, pp. 86–93. Available from DOI: 10.1364/PRJ.3.000086.

TAO, Rumao; MA, Pengfei; WANG, Xiaolin; ZHOU, Pu; LIU, Zejin, 2015b. Mitigating of modal instabilities in linearly-polarized fiber amplifiers by shifting pump wavelength. *Journal of Optics*. Vol. 17, no. 4, p. 045504. Available from DOI: 10.1088/2040-8978/17/4/045504.

TAO, Rumao; MA, Pengfei; WANG, Xiaolin; ZHOU, Pu; LIU, Zejin, 2015c. Study of Wavelength Dependence of Mode Instability Based on a Semi-Analytical Model. *IEEE Journal of Quantum Electronics*. Vol. 51, no. 8, pp. 1–6. Available from DOI: 10.1109/JQE.2015.2442760.

TAO, Rumao; WANG, Xiaolin; ZHOU, Pu, 2018. Comprehensive theoretical study of mode instability in high power fiber lasers by employing a universal model and its implications. *IEEE Journal of Selected Topics in Quantum Electronics*, p. 1. Available from DOI: 10.1109/JSTQE.2018.2811909.

TECHNAVIO.COM, 2020. *Global Fiber Laser Market: 2020-2024*.

TURITSYN, S. K.; BEDNYAKOVA, A. E.; FEDORUK, M. P.; LATKIN, A. I.; FOTIADI, A. A.; KURKOV, A. S.; SHOLOKHOV, E., 2011. Modeling of CW Yb-doped fiber lasers with highly nonlinear cavity dynamics. *Optics Express*. Vol. 19, no. 9, pp. 8394–8405. Available from DOI: 10.1364/OE.19.008394.

WANG, Meng; ZHANG, Yujing; WANG, Zefeng; SUN, Junjie; CAO, Jianqiu; LENG, Jinyong; GU, Xijia; XU, Xiaojun, 2017. Fabrication of chirped and tilted fiber Bragg gratings and suppression of stimulated Raman scattering in fiber amplifiers. *Optics Express*. Vol. 25, no. 2, pp. 1529–1534. Available from DOI: 10.1364/OE.25.001529.

WARD, B.; ROBIN, C.; DAJANI, I., 2012. Origin of thermal modal instabilities in large mode area fiber amplifiers. *Optics Express*. Vol. 20, no. 10, pp. 11407–11422. Available from DOI: 10.1364/OE.20.011407.

WEI, Daoping; KARPOV, Vladimir; GUO, Ning; CLEMENTS, Wallace R. L., 10.07.2018. *A 100-W 1178-nm continuous-wave single-frequency linearly polarized Raman fiber amplifier*. Available from DOI: 10.1117/12.2312114.

XIE, Kun; LIU, Wenguang; ZHOU, Qiong; HUANG, Liangjin; JIANG, Zongfu; XI, Fengjie; XU, Xiaojun, 2019. Adaptive phase correction of dynamic multimode beam based on modal decomposition. *Optics Express*. Vol. 27, no. 10, pp. 13793–13802. Available from DOI: 10.1364/OE.27.013793.

XU, Haiyang; JIANG, Man; SHI, Chen; ZHOU, Pu; ZHAO, Guomin; GU, Xijia, 2017. Spectral shaping for suppressing stimulated-Raman-scattering in a fiber laser. *Appl. Opt.* Vol. 56, no. 12, pp. 3538–3542. Available from DOI: 10.1364/AO.56.003538.

YANG, Baolai; SHI, Chen; ZHANG, Hanwei; YE, Qing; PI, Haoyang; TAO, Rumao; WANG, Xiaolin; MA, Pengfei; LENG, Jinyong; CHEN, Zilun; ZHOU, Pu; XU, Xiaojun; CHEN, Jinbao; LIU, Zejin, 2018a. Monolithic fiber laser oscillator with record high power. *Laser Physics Letters*. Vol. 15, no. 7, p. 075106. Available from DOI: 10.1088/1612-202X/aac19f.

YANG, Baolai; ZHANG, Hanwei; SHI, Chen; TAO, Rumao; SU, Rongtao; MA, Pengfei; WANG, Xiaolin; ZHOU, Pu; XU, Xiaojun; LU, Qisheng, 2018b. 3.05 kW monolithic fiber laser oscillator with simultaneous optimizations of stimulated Raman scattering and transverse mode instability. *Journal of*

Optics. Vol. 20, no. 2, p. 025802. Available from DOI: 10.1088/2040-8986/aa9ec0.

YE, Yun; XI, Xiaoming; SHI, Chen; ZHANG, Hanwei; YANG, Baolai; WANG, Xiaolin; ZHOU, Pu; XU, Xiaojun, 2019. Experimental Study of 5 kW High Stability Monolithic Fiber Laser Oscillator With or Without External Feedback. *IEEE Photonics Journal*, p. 1. Available from DOI: 10.1109/JPHOT.2019.2923709.

YE, Yun; YANG, Baolai; WANG, Peng; ZENG, Lingfa; XI, Xiaoming; SHI, Chen; ZHANG, Hanwei; WANG, Xiaolin; ZHOU, Pu; XU, Xiaojun, 2021. Industrial 6 kW high-stability single-stage all-fiber laser oscillator based on conventional large mode area ytterbium-doped fiber. *Laser Physics*. Vol. 31, no. 3, p. 035104. Available from DOI: 10.1088/1555-6611/abdfc2.

YODA, Hidehiko; POLYNKIN, Pavel; MANSURIPUR, Masud, 2009. Corrections to "Beam Quality Factor of Higher Order Modes in a Step-Index Fiber". *Journal of Lightwave Technology*. Vol. 27, no. 9, p. 1237. Available from DOI: 10.1109/JLT.2008.925069.

ZERINGUE, Clint; DAJANI, Iyad; NADERI, Shadi; MOORE, Gerald T.; ROBIN, Craig A., 2012. A theoretical study of transient stimulated Brillouin scattering in optical fibers seeded with phase-modulated light. *Optics Express*. Vol. 20, no. 19, pp. 21196–21213. Available from DOI: 10.1364/OE.20.021196.

ZERVAS, Michalis N., 2019. Transverse mode instability, thermal lensing and power scaling in Yb3+-doped high-power fiber amplifiers. *Optics Express*. Vol. 27, no. 13, pp. 19019–19041. Available from DOI: 10.1364/OE.27.019019.

ZERVAS, Michalis N.; CODEMARD, Christophe A., 2014. High Power Fiber Lasers: A Review. *IEEE Journal of Selected Topics in Quantum Electronics*. Vol. 20, no. 5, pp. 219–241. Available from DOI: 10.1109/JSTQE.2014.2321279.

ZHANG, Hanwei; XIAO, Hu; WANG, Xiaolin; ZHOU, Pu; XU, Xiaojun, 2020. Mode dynamics in high-power Yb-Raman fiber amplifier. *Optics Letters*. Vol. 45, no. 13, pp. 3394–3397. Available from DOI: 10.1364/OL.393879.

ZHAO, Nan; LI, Weihao; LI, Jiaming; ZHOU, Guiyao; LI, Jinyan, 2019. Elimination of the Photodarkening Effect in an Yb-Doped Fiber Laser With Deuterium. *Journal of Lightwave Technology*. Vol. 37, no. 13, pp. 3021–3026. Available from DOI: 10.1109/JLT.2019.2909575.

ZHAO, Nan; LIU, Yehui; LI, Miao; LI, Jiaming; PENG, Jinggang; YANG, Luyun; DAI, Nengli; LI, Haiqing; LI, Jinyan, 2017. Mitigation of photodarkening effect in Yb-doped fiber through Na+ ions doping. *Optics Express*. Vol. 25, no. 15, pp. 18191–18196. Available from DOI: 10.1364/OE.25.018191.

ZHOU, Pu; XIAO, Hu; LENG, Jinyong; XU, Jiangmin; CHEN, Zilun; ZHANG, Hanwei; LIU, Zejin, 2017. High-power fiber lasers based on tandem pumping. *Journal of the Optical Society of America B*. Vol. 34, no. 3, A29–A36. Available from DOI: 10.1364/JOSAB.34.000A29.

Acronyms

CLS Cladding light stripper.
ECDL External cavity diode laser.
FBG Fiber Bragg grating.
FM Fundamental mode.
FWM Four-wave mixing.
HOM Higher order mode.
MOPA Master oscillator power amplifier.
NA Numerical aperture.
NLSE Nonlinear Schrödinger equation.
OFDR Optical frequency domain reflectometer.
PM Polarization maintaining.
RFA Raman fiber amplifier.
SBS Stimulated Brillouin scattering.
SPM Self-phase modulation.
SRS Stimulated Raman scattering.
TMI Transverse mode instability.
XPM Cross-phase modulation.

Summary

Fiber lasers with kW-level average output power are a key tool in many modern production processes. However, further output power scaling is limited by stimulated Raman scattering (SRS) and transverse mode instability (TMI). TMI cause the emitted beam profile to fluctuate between different transverse modes of the fiber and SRS is an effect that transfers significant signal power to longer wavelengths. Besides the limits of further output power scaling, another important obstacle of high-power fiber lasers is the limited working wavelength of these systems. SRS can be used to overcome this obstacle, in the form of a Raman fiber amplifier (RFA). There, a strong SRS effect enables operation at otherwise inaccessible wavelengths and SRS needs to be enhanced, whereas for wavelengths within the amplifying band of the active ions it needs to be suppressed. Within this thesis, both of these cases are under study.
Prior to this thesis, an influence of the spectral width of the output coupler in high-power fiber oscillators on the Stokes content created by SRS has been observed but could not be explained. This is changed by this thesis that develops an enhanced, analytic walk-off model. These examinations show that walk-off between Raman pump and Stokes signal has a large effect on SRS in cw laser systems. The model and the influence of walk-off is verified by numerical simulations. These investigates pave the way for monolithic fiber oscillators with output powers beyond 6 kW and excellent beam quality.
Additionally, a narrow-linewidth RFA system is realized and its spectral properties are analyzed. Significant spectral broadening of the Stokes signal is observed. Cross-phase modulation of Raman pump and Stokes signal is identified as cause of this behavior. The Stokes output power of the RFA could be increased up to 500 W. Experimental evidence for TMI caused by SRS is given and, for the first time, it is shown that SRS-induced TMI can even occur within a passive fiber. Spectral separation of the Raman pump and Stokes signals allows determination of the TMI threshold by analyzing the individual beam profiles on a millisecond timescale. This enables experimental investigations of the TMI threshold in dependence of fiber length and Stokes seed power. The results are then used to test and advance theoretical predictions on their influence regarding the threshold. These findings can be used to select the most rewarding TMI mitigation strategy for further power scaling of RFA and, thereby, enable high-brightness sources at wavelengths otherwise unreachable.

Zusammenfassung

Faserlaser mit mittleren Ausgangsleistungen im kW-Bereich sind ein wichtiges Werkzeug in vielen modernen Produktionsprozessen. Die weitere Skalierung der Ausgangsleistung wird jedoch durch stimulierte Raman-Streuung (SRS) und transversale Modeninstabilitäten (TMI) begrenzt. TMI verursachen eine Fluktuation des emittierten Strahlprofils zwischen verschiedenen transversalen Moden der Faser und SRS ist ein Effekt, der signifikante Signalleistung zu längeren Wellenlängen (Stokes-Signalen) überträgt. Neben den Begrenzungen der weiteren Ausgangsleistungsskalierung ist ein weiteres wichtiges Hindernis von Hochleistungsfaserlasern der begrenzte Spektralbereich dieser Systeme. Um dieses Hindernis zu überwinden, kann SRS in Form eines Raman-Faserverstärkers (RFA) eingesetzt werden. Dort ermöglicht ein starker SRS-Effekt den Betrieb bei sonst unzugänglichen Wellenlängen und seine Verstärkung ist erwünscht, während er für Wellenlängen innerhalb des Verstärkerbandes der aktiven Ionen unerwünscht ist. In der vorliegenden Arbeit werden beiden Fälle untersucht.

Vor Beginn dieser Arbeit wurde ein Einfluss der spektralen Breite des Auskoppelreflektors in Hochleistungsfaseroszillatoren auf den Stokesgehalt beobachtet, konnte aber nicht erklärt werden. Dies wird durch die vorliegende Arbeit geändert, die ein erweitertes, analytisches Walk-off-Modell entwickelt. Die Untersuchungen zeigen, dass der Walk-off (das räumliche Auseinanderlaufen) zwischen Raman-Pumpe und Stokes-Signal einen großen Einfluss auf die SRS in cw-Lasersystemen hat. Das Modell und der Einfluss des Walk-offs wird durch numerische Simulationen verifiziert. Diese Untersuchungen ebnen den Weg für monolithische Faseroszillatoren mit Ausgangsleistungen jenseits von 6 kW und ausgezeichneter Strahlqualität.

Darüber hinaus wird in der vorliegendne Arbeit ein schmalbandiges RFA-System realisiert und dessen spektrale Eigenschaften analysiert. Es wird eine signifikante spektrale Verbreiterung des Stokes-Signals beobachtet. Eine Kreuzphasenmodulation von Raman-Pumpe und Stokes-Signal wird als Ursache für dieses Verhalten identifiziert. Die Stokes-Ausgangsleistung des RFA-Systems konnte auf bis zu 500 W gesteigert werden. Es wird der experimentelle Nachweis für eine durch SRS verursachte TMI erbracht und erstmals gezeigt, dass eine SRS-induzierte TMI sogar innerhalb einer passiven Faser auftreten kann. Die spektrale Trennung der Raman-Pump- und

Stokes-Signale erlaubt die Bestimmung der TMI-Schwelle durch Analyse der einzelnen Strahlprofile auf einer Millisekunden-Zeitskala. Dies ermöglicht experimentelle Untersuchungen der TMI-Schwelle in Abhängigkeit von der Faserlänge und der Stokes-Seed-Leistung. Die dabei gewonnenen Ergebnisse werden verwendet, um theoretische Vorhersagen über deren Einfluss auf die Schwelle zu testen und weiterzuentwickeln. Diese Erkenntnisse können genutzt werden, um die lohnendste TMI-Vermeidungsstrategie für die weitere Leistungsskalierung von RFA auszuwählen und zukünftig Quellen mit hoher Helligkeit bei sonst unerreichbaren Wellenlängen zu ermöglichen.

Publications

Peer-reviewed journals

1. V. Bock, M. Plötner, O. de Vries, J. Nold, N. Haarlammert, T. Schreiber, R. Eberhardt, A. Tünnermann. "Modal content measurements (S2) of negative curvature hollow-core photonic crystal fibers". Optics express 25 (4), 3006-3012 (2017)

2. M. Plötner, V. Bock, T. Schultze, F. Beier, T. Schreiber, R. Eberhardt, A. Tünnermann. "High power sub-ps pulse generation by compression of a frequency comb obtained by a nonlinear broadened two colored seed". Optics express 25 (14), 16476-16483 (2017)

3. R. Krämer, C. Matzdorf, A. Liem, V. Bock, W. Middents, T. Goebel, M. Heck, D. Richter, T. Schreiber, A. Tünnermann, S. Nolte. "Femtosecond written fiber Bragg gratings in ytterbium-doped fibers for fiber lasers in the kilowatt regime". Optics letters 44 (4), 723-726 (2019)

4. V. Distler, F. Möller, M. Strecker, G. Palma-Vega, T. Walbaum, T. Schreiber. "Transverse mode instability in a passive fiber induced by stimulated Raman scattering". Optics Express 28 (15), 22819-22828 (2020)

5. A. Popp, V. Distler, K. Jaksch, F. Sedlmeir, C. Müller, N. Haarlammert, T. Schreiber, C. Marquardt, A. Tünnermann, G. Leuchs. "Quantum-limited measurements of intensity noise levels in Yb-doped fiber amplifiers". Applied Physics B 126 (8), 1-7 (2020)

6. F. Möller, V. Distler, T. Walbaum, N. Haarlammert, J. Nold, T. Schreiber, S. Unger, V. Reichel, J. Kobelke, J. Bierlich, A. Schwuchow, T. Eschrich, M. Leich, K. Wondraczek, A Tünnermann. "Influence of pedestal diameter on mode instabilities in Yb/Ce/Al-doped fibers". Optics Express 28 (22), 33456-33474 (2020)

7. V. Distler, F. Möller, B. Yildiz, M. Plötner C. Jauregui, T. Walbaum, T. Schreiber. "Experimental analysis of Raman-induced transverse mode instability in a core-pumped Raman fiber amplifier". Optics Express 29 (11), 16175-16181 (2021)

Conference talks

1. V. Bock, T. Schultze, A. Liem, T. Schreiber, R. Eberhardt, A. Tünnermann. "The influence of different seed sources on Stimulated Raman Scattering in fiber amplifiers". CLEO (2017)

2. V. Bock, A. Liem, T. Schreiber, R. Eberhardt, A. Tünnermann. "Explanation of stimulated Raman scattering in high power fiber systems". SPIE Fiber Lasers XV (2018)

3. M. Heck, V. Bock, R. Krämer, D. Richter, T. Goebel, C. Matzdorf, A. Liem, T. Schreiber, A. Tünnermann, S. Nolte. "Mitigation of stimulated Raman scattering in high power fiber lasers using transmission gratings". SPIE Fiber Lasers XV (2018)

4. F. Möller, R. Krämer, C. Matzdorf, S. Nolte, M. Strecker, Fabian Stutzki, M. Plötner, V. Bock, T. Schreiber, A. Tünnermann. "Comparison between bidirectional pumped Yb-doped all-fiber single-mode amplifier and oscillator setup up to a power level of 5 kW". ASSL (2018)

5. V. Bock, M. Plötner, T. Walbaum, T. Schreiber, R. Eberhardt, A. Tünnermann. "Mode-locked Erbium-doped Fiber Laser with High Average Power and Ultra-short Pulse Duration". ASSL (2018)

6. F. Möller, V. Distler, T. Schreiber, R. Eberhardt, A. Tünnermann. "Manipulating the heat load distribution by laser gain competition in TMI-limited fiber amplifiers". SPIE Fiber Lasers XVII (2020)

7. V. Distler, F. Möller, M. Strecker, G. Palma-Vega, T. Walbaum, T. Schreiber, A. Tünnermann. "High power narrow-linewidth Raman amplifier and its limitation". SPIE Fiber Lasers XVII (2020)

8. N. Haarlammert, S. Kuhn, C. Hupel, J. Nold, S. Schulze, F. Möller, V. Distler, M. Strecker, G. Palma-Vega, S. Hein, D. Häßner, T. Walbaum, T. Schreiber, R. Eberhardt, A. Tünnermann. "Analysis of fabrication techniques and material systems for kW fibers limited by TMI". SPIE Fiber Lasers XVII (2020)

9. F. Möller, V. Distler, M. Strecker, T. Walbaum, T. Schreiber. "Backward transverse mode instability?". SPIE Fiber Lasers XVII (2021)

10. T. Walbaum, F. Möller, V. Distler, M. Strecker, T. Schreiber. "Guidelines and pitfalls in characterization of transverse mode instabilities". SPIE Fiber Lasers XVII (2021)

Acknowledgment

This doctoral thesis would not have been possible without the exceptionally good environment at the Friedrich Schiller University Jena, Institute of Applied Physics IAP and the Fraunhofer IOF, Institute for Applied Optics and Precision Engineering. In particular, I was able to experience an open error culture, friendly interaction and modern work culture in pandemic times. A whole range of people have contributed to the success of this work. I would like to thank all of them: Thank you very much! Thank you for your dedication, thank you for your shared and lonely hours in the lab, thank you for your borrowed equipment, thank you for the proofreading, thank you for all the presentation rehearsals, thank you for discussions, advice, literature, and much more.

Some people have said phrases during the course of my work that reflect well why I am grateful to them, among other things. Below I have condensed these sentences somewhat literary:

I will make sure it works. - Dr. habil. César Jauregui

I always have half an hour for you. - Prof. Dr. Jens Limpert

Just be a little bit proud of it. - Dr. Johannes Nold

I'll explain the basics again [unasked]. - Dr. Till Walbaum

Don't worry - my doctoral hat had a fiber guillotine. - Dr. Thomas Schreiber

I know, young people need some money. - Dr. Ramona Eberhardt

Of course I'll help you. - Every member of the laser technology department, especially Friedrich Möller, Max Strecker and Benjamin Yildiz.

Tell me about your work. - Elisabeth Distler, almost every day.

Finally, I would like to thank my children, whose existence created the pressure necessary to complete this work.

Curriculum vitae (Lebenslauf)

Ehrenwörtliche Erklärung

Ich erkläre hiermit ehrenwörtlich, dass ich die vorliegende Arbeit selbständig, ohne unzulässige Hilfe Dritter und ohne Benutzung anderer als der angegebenen Hilfsmittel und Literatur angefertigt habe. Die aus anderen Quellen direkt oder indirekt übernommenen Daten und Konzepte sind unter Angabe der Quelle gekennzeichnet.
Bei der Auswahl und Auswertung folgenden Materials haben mir die nachstehend aufgeführten Personen in der jeweils beschriebenen Weise entgeltlich/unentgeltlich geholfen:

1. Die Co-Autoren der entsprechenden Publikationen bei den durchgeführen Expiermenten und Simulationen.

Weitere Personen waren an der inhaltlich-materiellen Erstellung der vorliegenden Arbeit nicht beteiligt. Insbesondere habe ich hierfür nicht die entgeltliche Hilfe von Vermittlungs- bzw. Beratungsdiensten (Promotionsberater oder andere Personen) in Anspruch genommen. Niemand hat von mir unmittelbar oder mittelbar geldwerte Leistungen für Arbeiten erhalten, die im Zusammenhang mit dem Inhalt der vorgelegten Dissertation stehen.
Die Arbeit wurde bisher weder im In- noch im Ausland in gleicher oder ähnlicher Form einer anderen Prüfungsbehörde vorgelegt.
Die geltende Promotionsordnung der Physikalisch-Astronomischen Fakultät ist mir bekannt.
Ich versichere ehrenwörtlich, dass ich nach bestem Wissen die reine Wahrheit gesagt und nichts verschwiegen habe.

Ort, Datum Victor Distler